FZD-538

Advanced emitters and detectors for terahertz time-domain spectroscopy

Falk Peter

Juni 2010

Wissenschaftlich-Technische Berichte
FZD-538 2010 · ISSN 1437-322X

WISSENSCHAFTLICH-TECHNISCHE BERICHTE

Forschungszentrum Dresden Rossendorf

Wissenschaftlich-Technische Berichte
FZD-538
Juni 2010

Falk Peter

Advanced emitters and detectors for terahertz time-domain spectroscopy

Forschungszentrum
Dresden Rossendorf

Advanced emitters and detectors for terahertz time-domain spectroscopy

Dissertation

zur Erlangung des akademischen Grades
doctor rerum naturalium (Dr. rer. nat.)

vorgelegt von Falk Peter

eingereicht an der Fakultät
Mathematik und Naturwissenschaften
der Technischen Universität Dresden

Gutachter:	Prof. Dr. M. Helm (TU Dresden) Prof. Dr. T. Dekorsy (U Konstanz)

eingereicht im März 2010

Publications in refereed journals

Parts of the work presented in this thesis have been published in the following journals:

- F. Peter, S. Winnerl, H. Schneider, M. Helm, K. Köhler, “Large-area terahertz emitters based on GaInAsN”, Proceedings of SPIE 7366 (2009).
- S. Winnerl, B. Zimmermann, F. Peter, H. Schneider, and M. Helm, ”Terahertz Bessel-Gauss beams of radial and azimuthal polarization from microstructured photoconductive antennas”, Opt. Exp. 17, pp. 1571-1576 (2009).
- F. Peter, S. Winnerl, H. Schneider, M. Helm, and K. Köhler, ”Terahertz emission from a large-area GaInAsN emitter”, Appl. Phys. Lett. 93, 101102 (2008).
- S. Winnerl, F. Peter, A. Dreyhaupt, B. Zimmermann, M. Wagner, H. Schneider, M. Helm, and K. Köhler, “Generation and detection of THz radiation with scalable antennas based on GaAs substrates with different carrier lifetimes”, IEEE Journal of Selected Topics in Quantum Electronics 14, pp. 449-457 (2008).
- F. Peter, S. Nitsche, S. Winnerl, A. Dreyhaupt, H. Schneider, and M. Helm, “Coherent terahertz detection with a large-area photoconductive antenna”, Appl. Phys. Lett. 91, 081109 (2007).
- A. Dreyhaupt, F. Peter, S. Winnerl, S. Nitsche, M. Wagner, H. Schneider, M. Helm, and K. Köhler, “Leistungsstarke Emitter und einfach zu handhabende Detektoren für die Terahertz-Time-Domain-Spektroskopie”, Technisches Messen, Oldenburg Verlag 75, pp. 3-13 (2007).

Patent pending

- S. Winnerl, H. Schneider, A. Dreyhaupt, M. Helm, F. Peter, “Skalierbare Terahertz-Antennen”, EP 09160392.8 (2009).

Kurzfassung

Mit Hilfe der Terahertz-Zeitbereichs-Spektroskopie (engl. THz-TDS) lassen sich grundlegende Einblicke in die Dynamik von Stoffen und Materialien gewinnen. THz-TDS basiert auf der Analyse der Antwortfunktion der unterschiedlichen Proben mit spektral breitbandigen, ultrakurzen THz-Pulsen. Zur Erzeugung und Detektion von THz-Pulsen werden fotoleitende Schalter, sowie nichtlineare Kristalle genutzt. Der hohe Preis und die Komplexität der dabei benutzten Kurzpuls Titan Saphir Lasersysteme verhindert jedoch eine breite kommerzielle Nutzung. Erbium dotierte Faserlaser könnten hier eine günstigere Alternative sein. Diese Faserlaser arbeiten typischerweise mit einer Wellenlänge um $1.55\,\mu$m. In dieser Arbeit werden verschiedene nichtlineare Kristalle und fotoleitende Emitter untersucht, welche THz-Emission im Anregungsbereich von 800 nm bis 1550 nm erlauben. Das Hauptthema ist hierbei die Untersuchung geeigneter Substratmaterialien für fotoleitende Antennen mit interdigitalen Elektrodenstrukturen. Diese Antennen bieten einige Vorteile, wie hohe Beschleunigungsfelder bei moderaten Betriebsspannungen aufgrund geringer Elektrodenabstände. Durch die Skalierbarkeit dieser Strukturen sind aktive Bereiche von einigen mm^2 möglich, das erlaubt flächige Anregung mit größeren optischen Leistungen. Im Vergleich zu konventionellen fotoleitenden Quellen ergeben sich daraus Vorteile wie größere THz Felder, bessere Bandbreite und einfachere Handhabung bei der Justage. In Abhängigkeit vom Substrat können diese Emitter mit unterschiedlichen Anregungswellenlängen betrieben werden. Bei Substraten mit sehr schnellen Ladungsträgereinfang, und damit kurzer Ladungsträgerlebensdauer, können diese Antennen auch als Detektoren verwendet werden. Des Weiteren wird gezeigt wie man Emitter, basierend auf interdigitalen Strukturen, herstellen kann, die radial und azimutal polarisierte THz Wellen abstrahlen.Ein zweites Thema ist die Signalanalyse und Interpretation wenn ein THz Puls durch eine entsprechende Probe transmittiert. Diese Experimente zeigen das Potential von THz-TDS für Anwendungen, wie Spektroskopie und Tomographie. Im dritten Teil untersuchen wir organische und anorganische nichtlineare Kristalle als THz-Emitter. Das Hauptthema ist dabei polaritonische Phasenanpassung in GaAs. In Kombination dieser GaAs Kristalle mit einer Wellenleiterstruktur wurden Hinweise auf eine mit der Anregungswellenlänge durchstimmbare THz Emission gefunden. Dieser Effekt ist jedoch kleiner als erwartet, verschiedene Gründe dafür werden diskutiert.

Abstract

The idea of terahertz-time-domain spectroscopy (THz-TDS) is to exploit a single cycle, spectrally broad THz radiation pulse to gain insight into the response of matter. Photoconductive devices and nonlinear crystals are utilized in both the generation as well as the coherent detection of THz radiation. The relatively high cost and the complexity of commonly used titanium-sapphire lasers hinder a more widespread use of pulsed THz systems for commercial applications. Er-doped femtosecond fiber lasers operating at $1.55\,\mu$m could offer a viable alternative. In this thesis nonlinear crystals and photoconductive emitters are discussed for excitation in the near infrared (NIR) window of between 800 nm to 1550 nm.

The main focus of this thesis is a detailed study of substrate materials for an interdigitated photoconductive antenna. Photoconductive antennas with microstructured electrodes provide high electric acceleration fields at moderate voltages because of small electrode separations. The scalability of these devices allows for large active areas in the mm^2 range, which are sufficient for excitation at large optical powers. In comparison with conventional emitter structures, these antennas have more favourable characteristics regarding THz power, spectral properties, and ease of handling. Depending on the utilized substrate material, photoconductive antennas can then be operated using different excitation wavelengths. By employing substrates with short carrier trapping times these antennas can be operated as THz-detectors. Moreover the design of electrode structures for generating radially and azimuthally polarized THz waves are presented.

A second topic deals with the signal analysis and signal interpretation of THz pulses transmitted through several material systems. These experiments show the potential for tomographic and spectroscopic applications.

The third part deals with THz emission by frequency mixing in nonlinear organic and inorganic crystals. Hereby the focus is on polaritonic phase matching in GaAs. Furthermore, indications of THz tunability by the excitation wavelength were found by utilizing waveguide structures. However, the observed tuning range is much lower then theoretically predicted. Specific reasons for this are discussed.

Contents

1 Introduction

The combination of ultrashort laser- and semiconductor- technologies starting in the late seventies of the last century created the new field of terahertz optoelectronics. It is based on the principle that a semiconductor can become photoconductive for a short time interval, if a short laser pulse is applied. In pioneering work D. Auston developed an optoelectronic switch, that allows switching of electronic signals on a picosecond timescale [1]. Nowadays this kind of optoelectronic switch is known as Auston switch. Soon it was clear that the induced transient current in an Auston switch itself is the source for an electromagnetical pulse. Like the operating laser, the pulse duration of the generated pulse lies within the picosecond range. Again, it was D. Auston who demonstrated the free space propagation of such a pulse [2]. Because of their short pulse duration, the frequency spectra of these pulses range from Gigahertz- (10^9 Hz) to Terahertz (10^{12} Hz). Shortly after being discovered these optoelectronically generated pulses were named THz-Pulses. THz radiation covers the part of the electromagnetic spectrum between microwaves on the low frequency side and infrared waves on the high frequency side (0.1-10 THz). The first who applied fs optical pulses for spectroscopic applications with THz radiation were D. Grischkowsky and his colleagues [3, 4]. Since then, the experimental method has been known as “Terahertz Time-Domain Spectroscopy (THz-TDS)”. With the development of self-mode-locked operation in Ti:sapphire oscillators, there has been rapid advancement in the generation of sub-100 fs optical pulses [5]. The first Ti:sapphire lasers became commercially available in the early 1990s. Simultaneously, the molecular-beam-epitaxy (MBE) grown low temperature GaAs (LT-GaAs) thin films began to be utilized [6]. From that point onwards, dipole antennas fabricated on LT-GaAs substrates have frequently been utilized as emitters or detectors driven by photoconductive shorting of the dipole gap by pumping with a sub-100 fs Ti:sapphire laser.

Already in 1983, Auston [7] predicted that a propagating polarization in a Cherenkov cone radiates subpicosecond electro-optic (EO) shock waves. These are caused by optical rectification, when an ultrashort optical pulse is focused into a nonlinear material. In 1984 Auston and colleagues employed the EO effect for the detection of Cherenkov shock waves using the same EO crystal [8]. Wu and Zhang applied this technique in 1995 for free space THz pulse sensing [9]. THz detection with EO crystals has become popular due to its broad bandwidth capability and ease of realization.

In numerous scientific publications within the last two decades, THz-TDS has been used in order to obtain information about optical properties in the far infrared region [10, 11]. Many transitions in molecules, originating from lattice vibrations and rotations, are in the THz region of the electromagnetic spectrum. These transitions characterizing chemical and biological compounds. For instance in GaAs the LO phonon resonance is at around 8.7 THz [12]. Also for security application THz spectroscopy might be interesting since explosives reveal their spectral fingerprints [13]. Exploiting velocity matched optical rectification in $LiNbO_3$ based on pulse front tilting of the fs laser pulses showed efficient generation of THz radiation [14]. In the last decade higher frequencies and even higher bandwidths were obtained by phase-matched difference-frequency generation using two different wavelengths. For example by pumping an optical parametric amplifier with a high-power Ti:sapphire laser and mixing the generated idler and signal beams. In this way THz fields exceeding 100 MV/cm with a broad tunability from 10 to 70 THz were realized utilizing DFG in GaSe, $AgGaS_2$ [15]. However, combining several stages of nonlinear frequency conversion is very complicated and difficult to achieve.

THz sources include very complex systems like the Free Electron Laser (FEL). In general lasers consist of a gain medium, generating stimulated emission under strong optical or electrical excitation and a cavity which works as a resonator. In FELs this gain medium is replaced by a relativistic electron beam generated by an accelerator and the “stimulated emission” is realized by the deviation of the free electrons in a spatially periodic magnetic field in the undulator. The wavelength of the FEL is determined by the energy of the relativistic electrons and the period of the magnets in the undulator [16–18].

Another approach using compact semiconductors is the THz quantum cascade laser (QCL) operating in the region between 5 and 1 THz with peak powers up to 248 mW [19–21]. The drawback of the THz QCL is that they will only operate at cryogenic temperatures in this frequency range. It is not clear today, whether room-temperature operation for commercial applications can ever be achieved. Moreover, the THz QCLs are difficult to tune and do not deliver *ps* pulses. Other THz sources are gas lasers where the lasing transitions, typically a rotationally transition of the molecule, is in the THz region [22].

Due to the progress in the telecommunication industry, compact and reliable fibre based femtosecond lasers with a wavelength of around 1.5 μm have become available in the last years. In the future, these lasers might contribute to the development of relatively compact, stable and cost-effective THz systems if a suitable nonlinear or photoconductive material can be found. Besides organic materials GaAs is a promising candidate as a nonlinear medium. It has been demonstrated as a source and detection crystal with 1.56 μm pulses from a fibre laser [23]. However, its EO coefficient is about a factor of two lower than that of ZnTe which is widely applied with Ti:Sapphire systems at 800 nm wavelength. $\mathrm{Ga}_x\mathrm{In}_{1-x}\mathrm{As}$ grown by molecular beam epitaxy on a binary substrate is an attractive material system for THz systems powered by fibre lasers, because the bandgap can be tuned from 0.36 to 1.42 eV by varying the Ga mole fraction [24]. However, the resistivity of these materials is relatively low when employed as photoconductive devices resulting in a quick breakdown when the bias field is increased. Furthermore, saturation of the emitted THz radiation by rapid carrier screening limits the performance, as well as causing a low signal-to-noise ratio when used as photoconductive THz detector.

The objective of this study was to investigate the suitability of variously pulsed THz sources and detection devices when utilized with several laser systems and especially with lasers operating within ordinary telecom wavelengths.

This thesis is organized as follows:

Chapter 2 gives an overview over the fundamental principles of the generation, detection and propagation of THz pulses. Additionally, a short introduction explains which data analysis methods were used for the spectroscopic applications.

Chapter 3 describes our approach for a scalable photoconductive THz emitter as well as a THz detector. After a discussion about the idea of the chip layout and its manufacturing we study the performance and operating parameters using the device as emitter. A fiber laser based THz setup would greatly reduce costs and would be a step forward on the way to a “turn key” THz TDS system. Therefore a substrate material is presented which allows photoconductive excitation above a wavelength of $1\,\mu m$. For photoconductive detectors short carrier lifetimes and a fast temporally response are key features. Subsequently we present ion implanted and low temperature grown substrates for fast detectors. Moreover a novel design for generating radially and azimuthally polarized THz waves is presented.

A key aspect of THz-TDS is the determination of the complete dielectric function of a dielectric or semiconducting material. In chapter 4 we present examples of possible applications for an industrial use.

Chapter 5 concentrates on frequency mixing in a nonlinear medium. Organic DAST crystals as well as inorganic GaAs are discussed as appropriate materials for THz emitters. Hereby the focus is on the performance of the crystals when using several laser systems with different pulse energies and wavelengths. Finally, special attention is given to phase matching during the processes of generation and propagating THz waves in a GaAs-slab.

Appendix A.1 contains some of the more technical details of the employed laser systems, while Appendix A.2 sketches the idea of the Lorentz oscillator model, which is used for the calculation of the THz refractive index in GaAs.

2 Fundamentals of THz time-domain spectroscopy

This chapter deals with the basic concepts of Terahertz time-domain spectroscopy (THz-TDS). The main properties of THz radiation will be discussed as well as the important mechanisms for generating and detecting THz radiation. Furthermore, THz-TDS will be utilized in order to determine the optical properties of solids.

2.1 Generation of THz pulses

There are many different methods for generating THz pulses. Common to all these methods is the use of a femtosecond laser pulse which triggers an ultrashort change in polarization. One approach to obtain a rapid polarization change is using second-order effects in crystals (optical rectification). For this purpose a wide range of materials has been investigated since the 1990s [25–27]. It has been found that gallium selenide (GaSe), lithium niobate ($LiNbO_3$) or zinc telluride (ZnTe) with $\langle 110 \rangle$ orientation are most effective when utilized with Ti:Sapphire lasers. Organic crystals (DAST), which will be discussed in chapter 5, as well as $LiNbO_3$ are also applied [28–30]. In order to generate a substantial amount of THz radiation in these materials an amplified femtosecond laser with pulse energies of more than several $100\,\mu J$ ought to be used [31]. Ideally, pulse lengths should stay below 100 fs [32–34]. Intense THz radiation can also be achieved in laser-induced gas plasmas by introducing an AC external bias to the optical focus [35], but these plasma emitters are not the scope of this thesis. A different method of generating THz pulses was pioneered by Auston and Grischkowsky in the late 1980s [2, 36]. In this approach a femtosecond laser is applied to a semiconductor with suitable band gap and excites carriers, which are then accelerated by the surface field or by an external field which is applied by some metal electrodes on top of the semiconductor (Auston switch). The fast rise in the produced current leads to a change in polarization and radiates a sub-picosecond, single cycle and coherent electric pulse.

2.1.1 Carrier acceleration in the surface field

A simple emitter for THz radiation is the surface of a semiconductor. There are two superimposed mechanisms for generating THz radiation when the fs laser pulse illuminates the surface. One is the Photo-Dember effect and the other is a induced photocurrent in the surface field of the semiconductor.

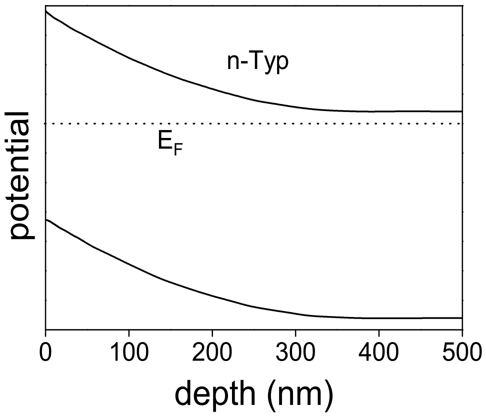

Figure 2.1: Midgap pinning of the Fermi level at the surface of a n-type semiconductor (e.g. GaAs).

Because of the broken symmetry at the surface there are additional unoccupied surface states locally increasing the density of states. The high density of surface states shifts the Fermi level of the bulk semiconductor into the surface states (Fermilevel-pinning). Since the Fermi level has to be constant between the bulk and the surface states, the valence and the conduction band are being bent. Depending on the doping the bending of the valence and the conduction band is either upwards (n doping -figure 2.1) or downwards (p doping). This bending leads to a drift current. In the case of a n-doped semiconductor the electrons move into the bulk and the holes toward the surface. This gradient in the carrier concentration subsequently initializes a diffusion in the opposite direction. However, in total a space charge separation is produced and so an electrical “built-in” field with a typical value of 10 to 100 kV/cm. The range of this field is dependent on the doping of the semiconductor but typically lies in the span of a few hundred nanometers. In this “built-in” field, photo excited carriers are accelerated perpendicular to the surface of the semiconductor and the radiated electric field is subsequently emitted parallel to the semiconductor surface. This and the relatively big step in the refractive index between vacuum and the semiconductor makes the outcoupling of the THz wave from the emitter more complicated. With an additional magnetic field the direction of the dipole can be optimized for a better decoupling [37, 38]. Also excitation under Brewster's angle increases the absorption of the gating laser pulse. The sudden change in the refractive index can be reduced by using a prism or substrate lens with the same refractive index as the emitter.

If there are large differences between the effective masses of the electrons and the holes in the semiconductor, then the dominating mechanism for THz generation is known as the photo Dember effect. Photo Dember means that the diffusion of the generally heavier holes is much slower than the diffusion of the electrons, as soon as the surface is excited by a short laser pulse. This again leads to a dipole radiating parallel to the semiconductor surface. Therefore the possibilities for optimization are the same as discussed above.

2.1.2 Carrier dynamics in photoconductive switches

When assessing the radiation emitted by the photocurrent in a switch-like emitter, the photocurrent density j can be described by a convolution between the response of the switch and the pulse shape of the incoming laser pulse

$$j(t) = q \cdot n(t) \cdot v(t) = q \int_{-\infty}^{t} dt' f(t-t') \cdot I(t') \cdot v(t'), \tag{2.1}$$

where n,q and v represent the density, charge and velocity of the carriers respectively. $I(t')$ is the normalized intensity envelope function of the laser pulse and $f(t-t')$ is a causal function describing a simple exponential decay of the carriers with lifetime τ_c, therefore $f(t-t')$ is proportional to $e^{-\frac{t-t'}{\tau_c}}$ [39]. The velocity of the free carriers in an electric field can described by the Drude theorie and is given by the differential equation [40]

$$\frac{dv(t)}{dt} = -\frac{v(t)}{\tau_s} + \frac{q}{m^*}E(t), \tag{2.2}$$

while the important material parameter for the transport is the carrier scattering time τ_s and the effective mass m*. The radiated THz field is determined by the

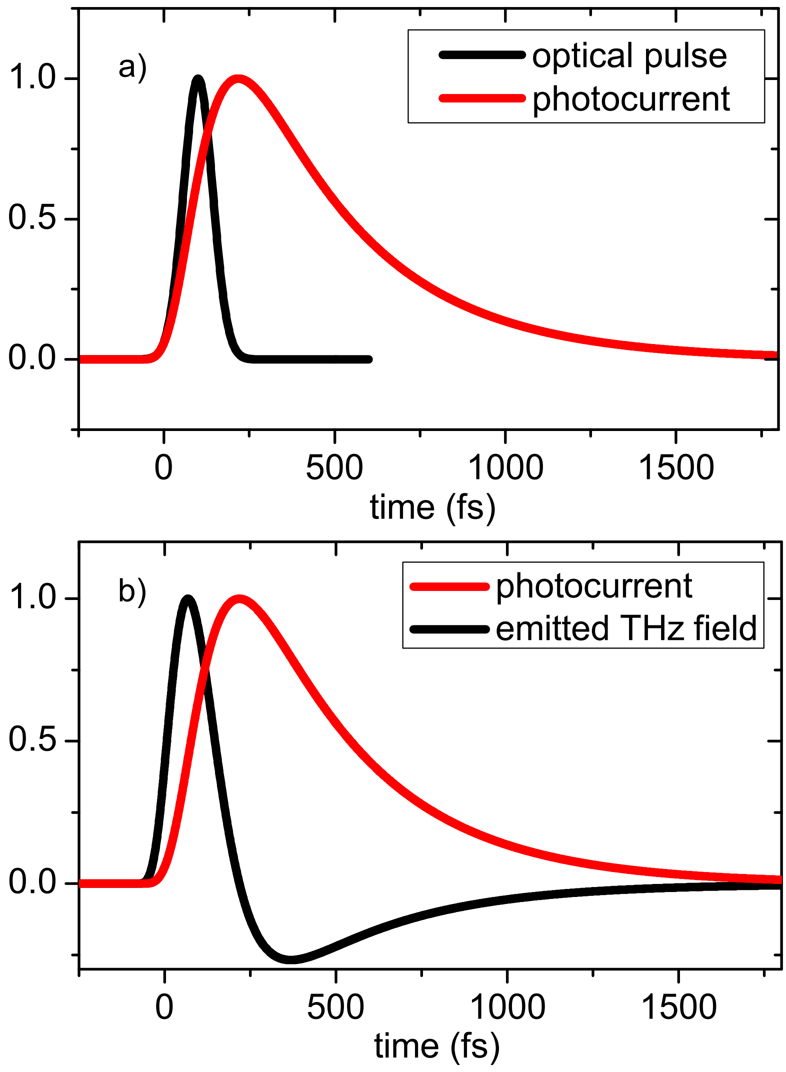

Figure 2.2: Photocurrent induced in the emitter (a) and the radiated THz pulse (b) from eqn. (2.3) with 100 fs laser pulse (FWHM), τ_s=50 fs and τ_c=500 fs.

temporal derivative of the photocurrent in the emitter antenna.

$$E_{THz} \propto \frac{dj(t)}{dt} \tag{2.3}$$

For the purpose of this illustration any screening field induced by space charges from the excited holes and photoelectrons has been ignored. This is true for carrier densities below $10^{18}\,\mathrm{cm}^{-3}$ [41, 42]. Furthermore it is assumed that a constant bias field over the photoconductive gap and a Gaussian shape of the femtosecond laser pulse is present and no intervalley transfer occurs ($m^* = const$). Figure 2.2 illustrates the induced photocurrent and the emitted field for a laser pulse with FWHM=100 fs duration, a carrier scattering time $\tau_s = 50\,\mathrm{fs}$ and a carrier recombination time $\tau_c = 500\,\mathrm{fs}$. The sharp increase of the photocurrent trace is much faster then its decay time (figure 2.2a). Because of the time derivative the radiated field is dominated by the sharp increase and the long tail of the photocurrent decay is irrelevant for the emitted field (figure 2.2b). For this reason semi-insulating (SI) GaAs is an adequate substrate choice for the emitter even though low temperature grown (LT) GaAs has a much faster carrier trapping.

2.1.3 Layout of photoconductive emitters

There are several designs for photoconductive emitters. Common to all these designs is that an external bias is applied to metal electrodes at the surface of the semiconductor. If a fs laser is gating the electrode gap, then a current is induced acting as the source for THz radiation, as it was discussed in the section before. The main difference in the several designs is the area size where the THz emission takes place. So far emission of THz radiation was originated between the electrodes in the semiconductor. However, if the area of the THz emission is much smaller than the emitted wavelength, an additional antenna is needed for an adequate outcoupling to free space. If so, the metal electrodes are used as an antenna. It is typical for a dipole antenna that, by adopting the geometries of the electrodes, it can be resonant to a certain frequency. For a dipole the rule of thumb for the relation between resonance frequency ν and dipole length L is given by $L = c/(2\nu\sqrt{\epsilon})$. Figure 2.3 shows typical designs of photoconductive emitters. The left side illustrates emitters using a dipole, bowtie and spiral shaped antennas for out-coupling. Typical bowtie antennas can emit broadband THz pulses, but they are not tuneable or scalable [43, 44], while spiral antennas are in principle scalable and also broadband emitters, but every frequency component of the emitted radiation has a different polarization [45, 47, 48]. These antenna coupled emitters have typical electrodes spacings of the order of a few micrometers resulting in a high bias field in the semiconductor. The distance between the electrodes can be further reduced by using additional interdigitated structures. A disadvantage is that the active re-

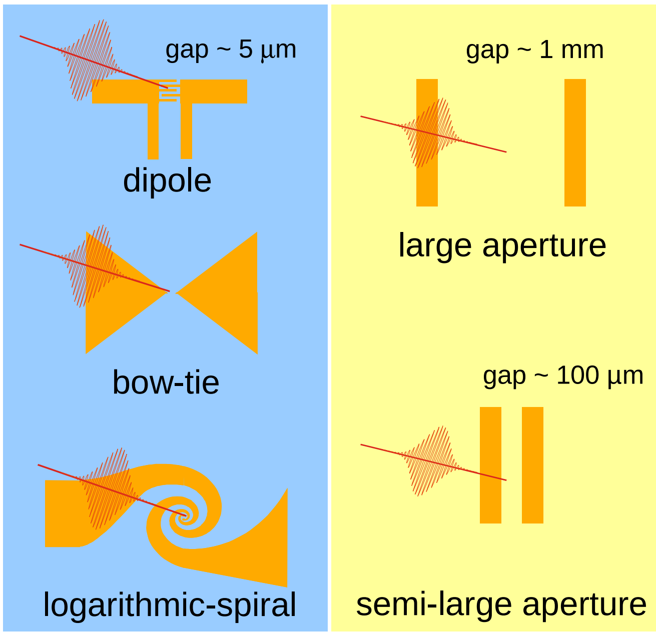

Figure 2.3: Small-area THz emitters with different antennas (left) and large-area THz emitters (right)

gion where the laser can excite carriers has to be small compared to the geometry of the antenna. Additionally, the THz emission saturates already for low optical powers, due to carrier screening of the external bias field [46]. Therefore, and to avoid damaging by hard focusing the usable optical power is limited.
The right side in figure 2.3 illustrates typical large area emitters. The advantage here is that larger laser spots can be employed and thereby a higher conversion of the laser power into THz radiation is possible. A disadvantage is the need of a much higher voltage for obtaining an adequate bias field as compared to the small area antennas. The semi-large emitter represents a trade off between a large active area and a high bias field up to a certain amount, but still requires voltages which are 20 times higher than in a dipole antenna. Another disadvantage of the larger electrode distance is the formation of a major space-charge field due to the photogenerated carriers between the metal electrodes. This screens the external bias field lowering the acceleration of the electrons and therefore limiting the THz emission [49]. Strictly speaking the large area emitters are no antennas, but typically they are also called photoconductive antennas and we will use this expression for

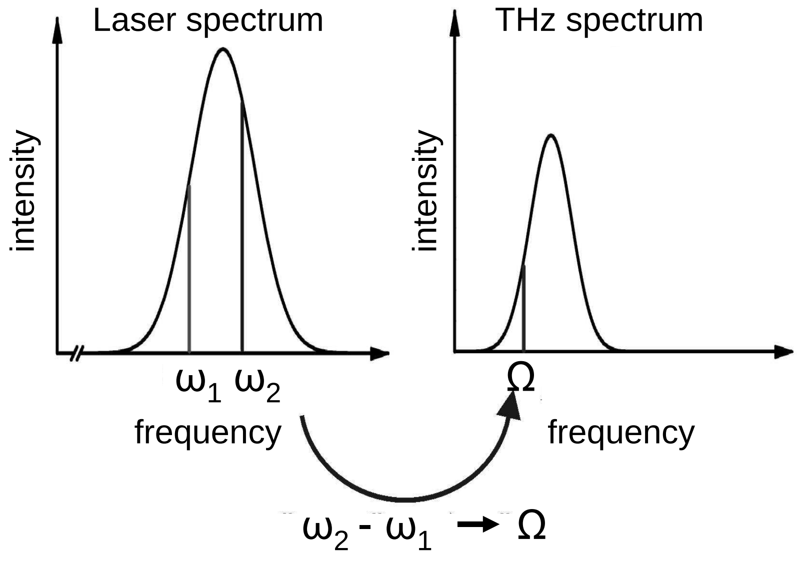

Figure 2.4: Principle of optical rectification. THz pulses are generated by mixing of spectral components within the ultrabroad laser spectrum.

the large-area devices as well.

2.1.4 Frequency mixing

Nonlinear crystals offer a further method for generating THz pulses from ultrashort laser pulses. The nonlinear response of such a crystal allows an energy transfer between electromagnetic fields with different frequencies. The best known example is frequency doubling or second harmonic generation (SHG). The SHG can be described by an addition of two photons with the same frequency to one photon with the double frequency ($2\omega = \omega + \omega$). Because of the short time duration, a femtosecond laser pulse contains a frequency distribution surrounding the central frequency. The shorter the laser pulse, the broader this frequency distribution is in the spectrum. The different frequency components contained in the short pulse can also be applied for difference frequency generation (DFG) ($\omega_3 = \omega_1 \pm \omega_2$). For typical pulse durations of fs laser systems these differences are in the THz range. Due to the much higher frequencies of optical electromagnetic waves compared with THz waves this mixing is called optical rectification (figure 2.4). The nonlinear response of such a crystal can be described by expanding the polarization P in a power series with respect to the electric field E.

$$P = P^{(0)} + P^{(1)} + P^{(2)} + \dots . \tag{2.4}$$

Without an external field there is no induced polarisation. Therefore $P^{(0)} = 0$, the linear response of matter is given by $P^{(1)} = \chi^{(1)}(\omega)E(\omega)$. Subsequently with 2.4 the nonlinear wave equation in the frequency domain is then

$$\nabla \times (\nabla \times E) - \frac{\omega^2}{c^2}\epsilon(\omega)E = \frac{\omega^2}{c^2\epsilon_0}P^{(2)}, \tag{2.5}$$

where $\epsilon(\omega) = \mathbf{1} + \chi(\omega)$ denotes the frequency dependent dielectric tensor. The second-order nonlinear polarisation $P^{(2)}$ can be regarded as a source for E. In the frequency domain the second-order polarisation of the i-th component in a medium is given by

$$P_i^{(2)}(\omega) = \epsilon_0 \sum_{jk} \chi_{ijk}(\omega; \omega_1; \omega_2)E_j(\omega_1)E_k(\omega_2) \tag{2.6}$$

where χ_{ijk} is the second-order susceptibility [50]. This second-order nonlinear polarisation describes the three-wave mixing in the nonlinear media and consists of a part representing the sum-frequency generation (SFG) with $\omega = \omega_1 + \omega_2 > 0$ for the generated frequencies and a part representing the difference-frequency generation (DFG) with $\Omega := \omega_2 - \omega_1 > 0$ for the generated frequencies. If $\omega_1; \omega_2$ are frequencies in the range around $800\,nm$ then Ω is in the THz range. Referring to equation (2.6) the i-th component of the DFG polarisation (P^{DFG}) is then determined by [51]

$$P_i^{(DFG)}(\Omega) = \epsilon_0 \int\limits_{LS} d\omega_2 \chi_{ijk}(\Omega; \omega_2; \omega_2 - \Omega)E_j(\omega_2)E_k^*(\omega_2 - \Omega). \tag{2.7}$$

Here the integration is over the whole spectrum of the laser (LS). In contrast to linear optics the wave equation 2.5 has now a source term with frequencies different from the initial frequency, particularly for DFG of an spectral broad laser pulse this frequencies are in the THz range. For computing the generated THz field we first look at the laser pulse and its propagation through the crystal in absence of any nonlinear effects. In the paraxial approximation ($\partial_x E = \partial_y E = 0$) and with the transmission coefficient at the interface air-sample t_{a-s} and the incoming laser field E_0, the laser field in the crystal is given by

$$E_{laser} = E_0(\omega_i)t_{a-s}(\omega_i)e^{ik_iz}. \tag{2.8}$$

Where k_i is the wave number

$$k_i(\omega_i) = \frac{n(\omega_i)\omega_i}{c}. \tag{2.9}$$

This laser field generates, by the nonlinear $\chi^{(2)}$-DFG-process, a radiating dipole at the position z_0 with a frequency $\Omega = |\omega_1 - \omega_2|$ and a strength which is proportional to $P^2(\Omega, z_0) \cdot \Omega^2/c^2$. The observable field E_{dip} from such a dipole at the position z outside the sample can then be represented by a spherical wave

$$E_{dip}(\Omega, z, z_0) \propto \frac{\Omega^2}{c^2}P^{(DFG)}(\Omega, z_0)\frac{e^{iK(\Omega)|z-z_0|}}{2iK(\Omega)} \cdot t_{s-a}, \tag{2.10}$$

with the wave number

$$K(\Omega) = \frac{N(\Omega)\Omega}{c}, \tag{2.11}$$

where N(Ω) is the THz refractive index. Here multiple reflections inside the sample are neglected. Furthermore we neglect the depletion of the NIR laser beam through the THz generation. The total field E_{THz} is then given by the sum of all dipole waves in the volume V of the crystal

$$E_{THz}(\Omega, z) = \int\limits_{V'} dV E_{dip}(\Omega, z, z_0). \tag{2.12}$$

Because of the paraxial approximation the integration over dx and dy in (2.12) gives a constant and simplifies to

$$E_{THz}(\Omega, z) \propto \int\limits_{o}^{\mathrm{z}} dz_0 E_{dip}(\Omega, z, z_0). \tag{2.13}$$

This integral can become zero, if all dipoles interfere destructively at the position z of the observer. For a crystal with a thickness d and the nonlinear polarisation

(2.7) the THz field reads

$$\begin{aligned} E_{THz}(\Omega, d) \propto \; & t_{s-a}(\Omega) e^{iKd} \frac{\Omega^2}{iKc^2} \int_0^d dz_0 \int_{LS} d\omega_1 \chi^{(2)}_{eff} E_0(\omega_1) E_0^*(\omega_1 - \Omega) \\ & \cdot e^{i\Delta k z_0} t_{a-s}(\omega_1) \cdot t_{a-s}(\omega_1 - \Omega), \end{aligned} \tag{2.14}$$

using the so-called phase matching relation $\Delta k = k_1 - k_2 - K$, and $\chi^{(2)}_{eff}$ which stands for the nonzero component of the second-order susceptibility tensor. $\chi^{(2)}_{eff}$ is determined by the polarisation of the exciting laser field and symmetry of the utilized nonlinear crystal. Integration over z_0 gives the field at the surface of the crystal

$$\begin{aligned} E_{THz}(\Omega, d) \propto \; & t_{s-a}(\Omega) \frac{\Omega^2}{Kc^2} e^{iKd} \int_{LS} d\omega_1 \chi^{(2)}_{eff} E_0(\omega_1) E_0^*(\omega_1 - \Omega) \frac{e^{i\Delta kd} - 1}{\Delta k} t_{a-s}(\omega_1) \\ & \cdot t_{a-s}(\omega_1 - \Omega). \end{aligned} \tag{2.15}$$

The coefficient

$$\frac{e^{i\Delta kd} - 1}{\Delta k}, \tag{2.16}$$

originates from the spatial summation of all THz dipoles, it describes the interference of the dipoles and how constructive the THz generation is. If Δk goes to zero, the emitted field has its maximum, and phase matching is perfect.

2.1.5 Phase matching or the conservation of momentum

A meaningful consideration which we address here is the use of phase matching to allow for greater interaction between the optical and THz pulses in the nonlinear medium in order to improve the efficiency of the generation process.

As shown in the previous section the creation of THz pulses in a difference frequency mixing process involves three different electric fields ($E_{NIR}(\omega_1), E_{NIR}(\omega_2), E_{THz}(\Omega)$) that have to fulfill the wave equation (2.5) simultaneously, since all waves interact in the nonlinear crystal. The conservation of momentum for this process reads:

$$\hbar k(\omega_2) - \hbar k(\Omega) = \hbar k(\omega_2 - \Omega). \tag{2.17}$$

Using $\omega_2 >> \Omega$ yields an approximation for

$$k(\omega_2 - \Omega) \approx k(\omega_2) - \Omega \frac{dk(\omega_2)}{d\omega} \tag{2.18}$$

and with (2.17)

$$k(\Omega) = \Omega \frac{dk(\omega_2)}{d\omega}, \tag{2.19}$$

and with the relation k=nω/c resulting in

$$n(\Omega) = \frac{d}{d\omega} \left[n(\omega)\omega \right]_{\omega=\omega_2} = n(\omega_2) + \omega_2 \frac{dn(\omega_2)}{d\omega}, \tag{2.20}$$

which is exactly the definition of the group velocity of the NIR $n_g = n + \omega \frac{dn}{d\omega}$. This condition implies that the phase velocity of the generated THz pulse has to match the group velocity of the NIR pulses along the length of the crystal. Otherwise THz pulses generated at different positions in the crystal would interfere destructively. From this point of view it is clear that the phase matching condition is most critical for long crystals, while it becomes less important in thin ones.

The phase matching condition can be met in different ways. For instance in anisotropic birefringent crystals like GaSe, KDP or $LiNbO_3$ it can be achieved by mixing an extraordinary beam with frequency ω_1 with an ordinary beam with frequency ω_2 by tilting the optical axis with respect to the polarization of the extraordinary beam. Adjusting this phase matching angle allows to tune the phase matched THz frequencies and therefore the emitted spectrum [52].

Another possibility to obtain phase matching is a periodic variation of the $\chi^{(2)}$ nonlinear coefficient in quasi-phase-matched (QPM) crystals. Optical rectification in a QPM crystal was first demonstrated in periodically-poled lithium niobate [30] and later in GaAs [53]. The idea of QPM rectification is that each inverted domain of a QPM crystal contributes a half cycle of the THz pulse and thus the THz wave packet has as many oscillation cycles as the number of QPM periods over the length of the crystal. Adjusting the orientation-reversal period allows one to tune the bandwidth and wavelength of the emitted THz radiation. The challenge is the patterning of the nonlinear susceptibilities in the crystals. For instance in diffusion bonded GaAs alternately rotated plates with $\langle 110 \rangle$ orientation are stacked together

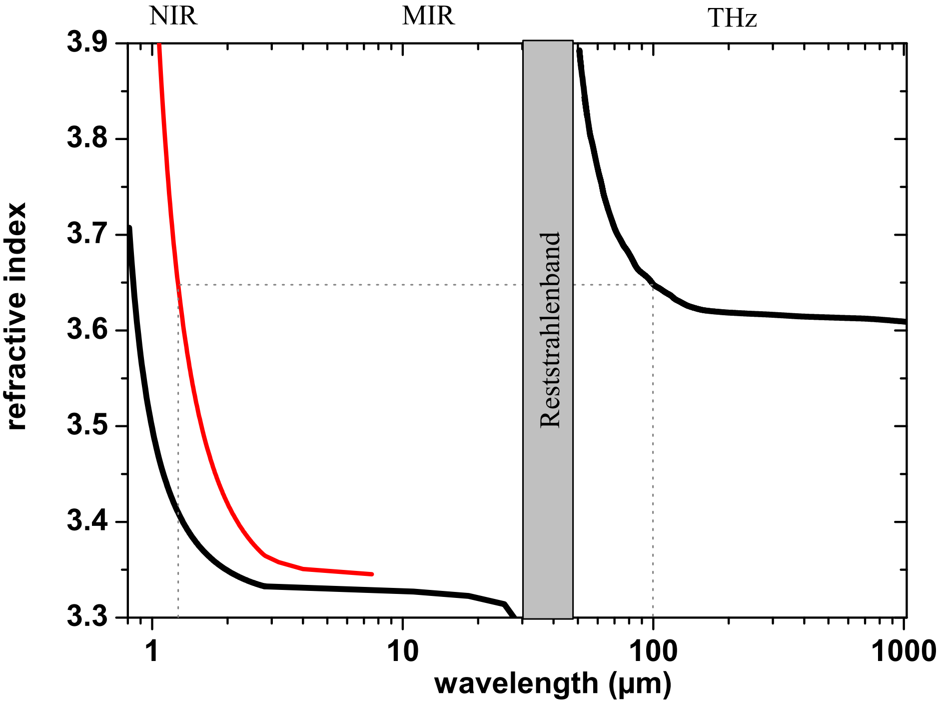

Figure 2.5: Index of refraction of bulk GaAs (black line) [55]. The red line represents the right term of equation 2.20 i.e. the group refractive index of the NIR pulse.

and by wafer fusion a monolithic body with periodic change in the nonlinear coefficient is created. Further technologies in fabrication QPM GaAs can be found in Ref. [54].

A third possibility to obtain phase matching in optically isotropic materials, where no birefringence is possible, is to use the anomalous dispersion introduced by optical phonon absorption at the reststrahlenband in GaAs. Berger and co-workers have shown in Ref. [56] that there exists a phase matching point, where one of the wavelengths lies in the THz range and the second, shorter wavelength is in the NIR around 1.4 μm. The reststrahlenband lies between those frequencies giving rise to a non-monotonic refractive index $n(\omega)$ (figure 2.5). The reststrahlen region in semiconductors lies between the transverse and longitudinal optical phonon (33.1 meV and 36.1 meV in GaAs at room temperature, respectively [57]), where the dielectric constant becomes negative and electromagnetic propagation is forbidden. Figure 2.5 shows this theoretical model for the polaritonic phase matching in bulk GaAs.

The dotted lines show the phase matching point for the generation of 3 THz radiation with a NIR wavelength of about 1.3 μm.

2.1.6 The angular dependence of the second-order susceptibility

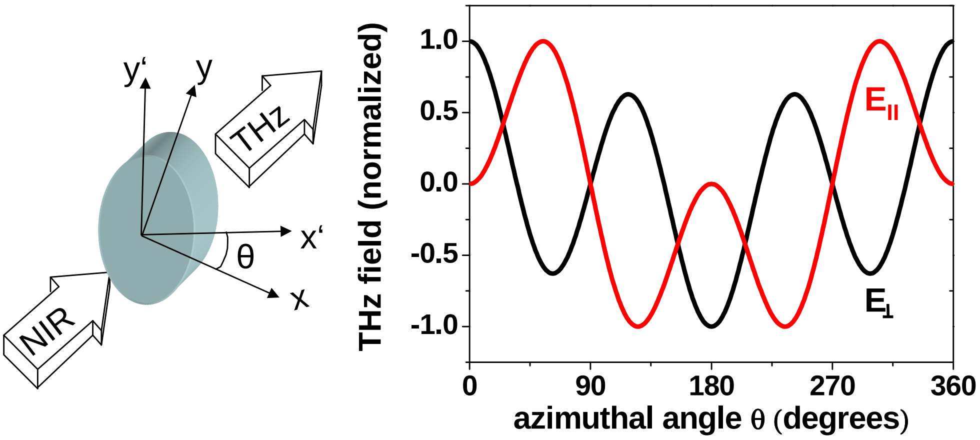

Figure 2.6: THz field from $\langle 110 \rangle$ GaAs vs azimuthal angle θ for the x- polarization (red) and the y- polarization (black) of the THz field. [148]

As shown in section 2.1.4, in the far field the radiated electromagnetic field is proportional to the second time derivative of the dielectric polarization $P(r,t)$. Most of III-V and II-VI semiconductors are zincblende crystals in particular also GaAs. These crystals have a cubic structure with point group $43m$ symmetry and have only one independent nonvanishing second-order nonlinear optical coefficient, namely $\chi_{123} = \chi_{231} = \chi_{312} \neq 0$ or, with the assumption that χ_{ijk} is symmetrical on the last two indices, χ_{ijk} becomes χ_{il}, whereby $\chi_{14} = \chi_{25} = \chi_{36} \neq 0$ (Kleinman's conjecture [51]). In equation (2.14) (section 2.1.4) we introduced the effective second-order susceptibility $\chi^{(2)}_{eff}$ describing the non-vanishing components of the tensor matrix. To keep the description simple, we have ignored the fact that $\chi^{(2)}_{eff}$ has an angular dependency between the crystallographic axis and the polarization direction of the incident laser field. This angular dependence of $\chi^{(2)}_{eff}$ for a $\langle 110 \rangle$ oriented GaAs crystal can be described with the only independent element of the susceptibility tensor d_{14} [1] in the form

$$\chi^{(2)}_{eff}(\theta) \propto \quad d_{14}(cos3\theta - cos\theta) \quad \text{NIR} \; || \; \text{to THz (x-direction)} \tag{2.21}$$

$$\chi^{(2)}_{eff}(\theta) \propto \quad d_{14}(3cos3\theta + cos\theta) \quad \text{NIR} \perp \text{to THz (y-direction)} \tag{2.22}$$

Thereby θ is the azimuthal angle between the space coordinate and the crystallographic coordinate [58]. The polarization of the NIR field is assumed to be in the x-direction. Figure 2.6 illustrates the electrical field components (x -red, y -black) of the radiated THz wave in dependence on the azimuthal angle, θ, between the fixed space axes (x,y) and the crystallographic axes (x',y').

---

[1] in general $d_{ijk}=\frac{1}{2}\chi_{ijk}$

2.2 Detection of THz pulses

Today, the two most commonly adopted methods in measuring THz pulses are the photoconductive and the electro-optic detection. The latter one is widely used, mainly due to its high bandwidth and the possibility to quantitatively measure the THz field. However, photoconductive detection antennas are more suitable for compact THz spectrometers. The principle of photoconductive detection is very similar to the generation as outlined in section 2.1.3 and will be discussed in more detail here.

2.2.1 Substrates with short carrier lifetimes

Again the fs laser generates carriers in a semiconductor like GaAs. If the photon energy $\hbar\omega_0$ of an optical pulse is higher than the bandgap energy E_g, then so called "hot" carriers with energy $\hbar\omega_0 - E_g$ are generated. Because of their smaller mass the electrons possess most of this energy.
The hot carriers lose their kinetic energy by various scattering mechanisms, mostly by optical phonon scattering on a picosecond timescale [12]. Furthermore the carriers can recombine sending out a photon or be trapped by an impurity. This trapping is usually described by the $Shockley-Read\ Hall$ recombination. The trapping time constant τ_t is determined by the trap concentration N_t, thermal velocity υ_{th} and the capture cross section of the impurity σ.

$$\tau_t = \frac{1}{N_t \sigma \upsilon_{th}} \tag{2.23}$$

If the THz pulse arrives at the detector during the lifetime of the carriers they will be accelerated towards the electrodes. This produces a measurable mean current. The detected current $I(t)$ in the detector antenna is proportional to a convolution of the transient conductance $g(t)$ and the time dependent THz field $E(t)$ as described by the equation

$$I(t) \propto \int_{-\infty}^{\infty} E(t_1) g(t - t_1) dt_1. \tag{2.24}$$

If the carrier lifetime is much shorter than the typical timescale of the terahertz waveform $g(t-t_1)$ can be approximated by a δ-function and the measured current is directly proportional to $E(t)$. In the opposite case of long carrier lifetimes $g(t-t_1)$ can be approximated by a step function and $E(t)$ is proportional to the first derivative of the measured current. Within a more detailed approximation wherein the number of generated carriers is determined by the laser pulse power $P(t)$ and provided that carrier trapping can be treated as a single-exponential process with a time constant τ and a constant mobility μ, the transient conductance can be written as

$$g(t) \propto \mu \cdot \int_{-\infty}^{t} P(t_1) exp\left[(t-t_1)/\tau\right] dt_1. \tag{2.25}$$

To illustrate the effect of different carrier lifetimes, the detected current was calculated using (2.24) and (2.25). For $P(t)$, a Gaussian function with an FWHM of 100 fs was applied. For $E(t)$, a bipolar testfunction, i.e., a positive signal followed by a negative signal of similar shape and amplitude was chosen. The same value of the mobility was employed in all calculations. The Fourier transform of the test function for $E(t)$ has a maximum at 1.2 THz and extends up to 5 THz, which is very similar to the emitted spectrum of photoconductive THz emitters [59], [60]. In Fig. 2.7, the results of the calculation are shown. For short carrier lifetimes, the current is proportional to $E(t)$, while for carrier lifetimes above 1 ps, the photocurrent signal consists of a broad large positive peak followed by a negative peak of small amplitude and long duration. The peak-to-peak signal reaches a maximum for carrier lifetime of about 1 ps, with a sharp decrease towards smaller lifetimes and a weak decrease towards longer lifetimes. In this simple picture carrier lifetimes similar to the typical duration of the THz pulse are most favorable. In nonstoichiometric GaAs (ion implanted or low-temperature-grown), the mobility will typically increase as the carrier lifetime increases in the range discussed here. This would lead to an increase of the detected signal even for carrier lifetimes above 1 ps. However, lifetimes similar to the typical duration of the THz pulse are still attractive considering the detector noise. Coherent photoconductive detection can be viewed as an ultrafast boxcar technique; hence, minimum noise is collected if the carriers do not live significantly longer than the duration of the THz pulse. There are

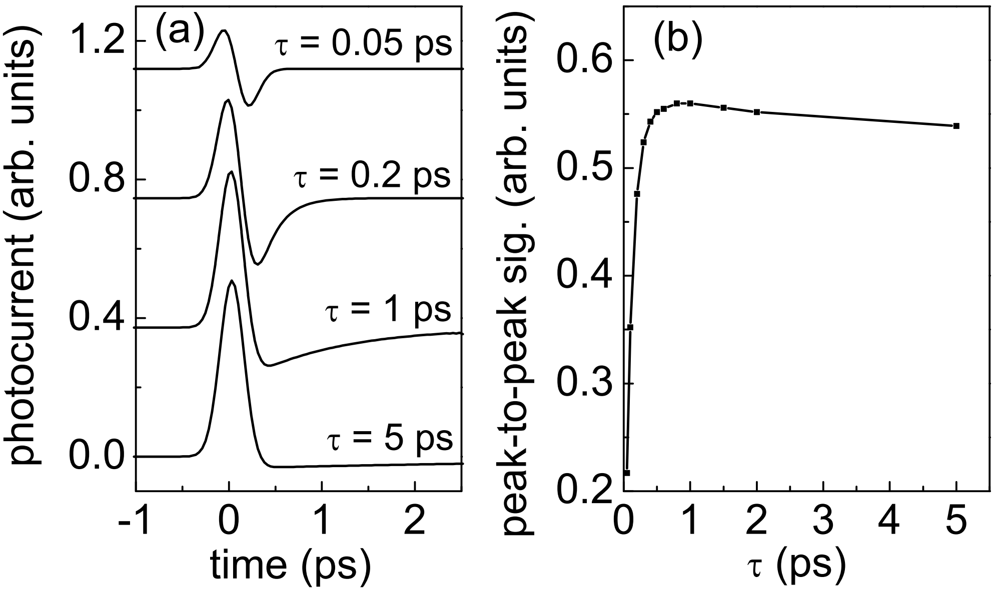

Figure 2.7: (a) Calculated photocurrent traces for different carrier lifetimes. (b) Peak to peak dependency according to carrier lifetimes [61].

two main approaches in fabricating substrates with short carrier lifetimes. One is implantation of the semiconductor substrate (here GaAs), the other possibility is low-temperature-grown gallium-arsenide (LT-GaAs).

LT-GaAs

For conventional molecular beam epitaxy (MBE) grown GaAs the substrate is heated to ≈ 600 °C. Together with the flux ratio and the growth rate this defines the main properties of the grown material. Low-temperature-grown gallium-arsenide (LT-GaAs) can be fabricated using MBE at temperatures below 300 °C [62]. Depending on the growth condition LT-GaAs has an excess of arsenic of one to two percent. This leads to a high density of point defects consisting of antisite impurities and gallium vacancies. The ionized or neutral donors $[As_{Ga}]^+$, $[As_{Ga}]^0$, respectively, form an impurity band below the conduction band. The concentration of $[As_{Ga}]^+$ can be in the range of 10^{18} - 10^{19} cm^{-3}, the concentration of $[As_{Ga}]^0$ 10^{19} - 10^{20} cm^{-3} [63]. This midgap impurity band is responsible for the short carrier lifetime via trapping described by $Shockley-Read\ Hall$ recombination (eq. 2.23). In figure 2.8 the density of states and the impurity concentrations for LT-GaAs

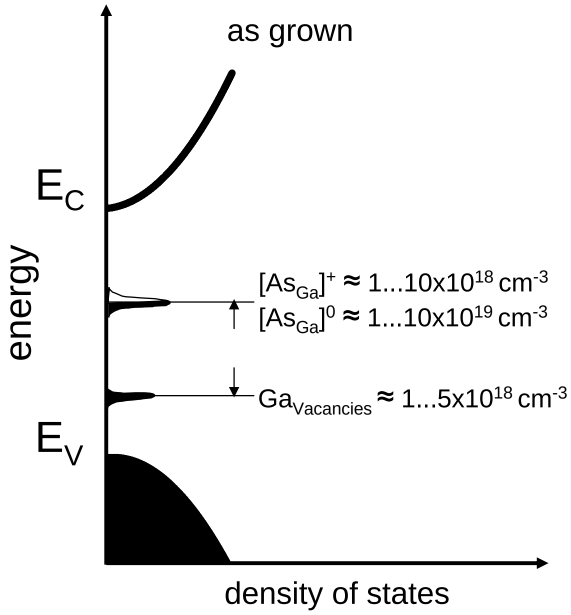

Figure 2.8: Energy band diagram in as-grown LT-GaAs (from [64]).

(as grown) are shown (from [64]). Unfortunately the formation of this impurity band also lowers the resistivity of the material after the growth process, limiting the usage for optoelectronic devices where high bias fields are needed.
However, S. Gupta et al showed in Ref. [62] that thermally annealed LT-GaAs forms As-Clusters which are surrounded by depleted regions of As-adatoms. They showed that in this annealed LT-GaAs the trapping occurs at these clusters which have a density in the range of 10^{17} to 10^{18} cm^{-3}. Furthermore this clustering due to the annealing improves the carrier mobility and increases the resistance due to a reduced hopping transport [64], if the right parameters are chosen.

Ion implanted GaAs

Another technique to obtain carrier lifetimes in the picosecond and even subpicosecond regime is the implantation of As^+, H^+, O^+ or N^+ into GaAs. The implanted ions create an impurity band which is responsible for the fast recombination, just like in LT-GaAs. Multiple implantations and the proper choice of implantation energies allows selective implantation profiles in the substrate. The concentration

of the implanted ions can be easily controlled by measuring the ion current.
Ion implantation is viewed as an easier alternative to MBE grown material. While it still seems difficult to compare LT-MBE temperatures for different machines, ion implantation conditions can easily be adapted for different machines.

2.2.2 Electro-optical sampling

The electro-optic detection is based on the Pockels effect, where a crystal in an external electric field induces a birefringence. With a laser wavelength of around 800 nm, ZnTe crystals are usually applied, but other materials are also available. A part of the near-infrared laser is used as probe and the THz pulse itself is the electric field, that induces the birefringence and in this way the polarization of the fs laser pulse. Using a polarizing beam splitter and two balanced photodiodes allows one to detect this change in polarization. It is necessary that the THz pulse and the fs pulse are temporally and spatially coincide at the detector.
Electro-optic sampling has developed into a powerful method to characterize THz pulses, as it measures directly the electric field and additionally allows the quantification of the THz field strength. For a $\langle 110 \rangle$ oriented ZnTe crystal the field can be obtained by [65, 66]:

$$E_{THz} = \frac{\Delta I}{I} \frac{\lambda}{2\pi n^3 r_{41} L}, \tag{2.26}$$

where E_{THz} is the THz electric field, $\frac{\Delta I}{I}$ is the relative modulation of the measured photodiode signal, $r_{41} = 3.9\,\frac{pm}{V}$ is the electro-optic coefficient and L is the length of the crystal. λ is the wavelength of the sampling laser and n is the corresponding near infrared refractive index. Equation (2.26) signifies that a thicker electro-optic crystal leads to a larger effect on the photodiodes. However, equation (2.26) does not consider the phase mismatch between the near infrared group velocity in the crystal and the THz phase velocity due to varying indices of refraction at the respective wavelengths. The thicker the crystal becomes, the larger this phase mismatch and the narrower the detectable THz bandwidth. Therefore, a sensor crystal with a adequate thickness is a key for the optimization of the THz pulse detection [67].

2.3 Essential data analysis in THz Spectroscopy

In a THz Time Domain Spectroscopy (TDS) measurement one obtains an electric field trace with a temporal resolution in the range of 10 fs to several 100 fs depending on the used laser system and the THz generation process. For extracting the frequency information those traces are transformed into the frequency domain by a Fourier transformation

$$E(\omega) = \frac{1}{2\pi} \int\limits_{-\infty}^{+\infty} e^{-i\omega t} E(t) dt. \tag{2.27}$$

Recording two traces in a spectroscopic experiment, one, where the pulse propagates through the sample, and one reference pulse propagating only through the surrounding media, E_s and E_{ref}, allows one to gain information about the dielectric function of the sample.

In a basic scheme the sample is a parallel plate with thickness d and a frequency dependent refractive index $n_s(\omega)$. By passing through, the pulse gains a phase factor $P_s(\omega)$. For a signal transmitted through the sample the electric field then reads

$$E_s(\omega) = E_0(\omega) t_{a-s}(\omega) P_s(\omega) t_{s-a}(\omega). \tag{2.28}$$

We consider reflection and transmission only at the first and second interface (air-sample and sample-air, respectively). Furthermore we assume normal incidence and a planar surface without scattering, thereby we can use the Fresnel equations for the transmission coefficients t_{a-s} and t_{s-a} in the form

$$t_{a-s} = \frac{2n_a}{n_a + n_s(\omega)} \tag{2.29}$$

$$t_{s-a} = \frac{2n_s(\omega)}{n_a + n_s(\omega)}. \tag{2.30}$$

The accumulated phase can be described by

$$P_s(\omega, d) = e^{-i\frac{n_s \omega d}{c}}. \tag{2.31}$$

The reference signal is not reflected at interfaces and we only have to consider the phase accumulated by passing the distance d through air

$$E_{ref}(\omega) = E_0(\omega)P_{ref} = E_0 e^{-i\frac{n_a \omega d}{c}} \tag{2.32}$$

Now we introduce the so called transfer function $H(\omega)$, which is the quotient of E_s and E_{ref} and a complex number, we can write in polar form

$$H(\omega) = \frac{E_s(\omega)}{E_{ref}(\omega)} = A(\omega)e^{i\Delta\Phi}. \tag{2.33}$$

Inserting equation 2.28 to 2.32 in 2.33 we obtain

$$H(\omega) = \frac{E_s(\omega)}{E_{ref}(\omega)} = \frac{4n_s(\omega)n_a}{(n_s(\omega)+n_a)^2} exp\left(-i\underbrace{\frac{\omega d}{c}(n_s(\omega)-n_a)}_{\Delta\Phi}\right). \tag{2.34}$$

The quantities available from the experiment are $E_s(\omega)$, $E_{ref}(\omega)$ and their corresponding phases Φ_s and Φ_{ref}, respectively. Setting the refractive index n_a of air to 1 and using the above definition for $\Delta\Phi$ one can write for the refractive index of the sample

$$n_s(\omega) = 1 + \frac{c}{\omega d}\Delta\Phi, \tag{2.35}$$

where $\Delta\Phi$ is given by $\Delta\Phi = |\Phi_{ref} - \Phi_s|$.

In a more precise consideration we have to keep in mind that n_s is also a complex value given by $n_s = n_r + in_i$. So far any absorption for obtaining the refractive index has been neglected and $n_s(\omega) = n_r(\omega)$ was a real number. For the absorption the imaginary part of n_s is determined by $n_i = \frac{c}{2\omega}\alpha$, with the absorption coefficient α [68]. By inserting this into equation (2.34) we obtain for the transfer function

$$H(\omega) = A(\omega)e^{i\Delta\Phi} = \frac{4n_r(\omega)n_a}{(n_r(\omega)+n_a)^2} exp\left(-i\frac{\omega d}{c}(n_r(\omega)-n_a)\right) e^{-\frac{1}{2}\alpha d}. \tag{2.36}$$

Solving (2.36) gives, with the ratio of the field amplitudes A, the absorption coefficient

$$\alpha(\omega) = -\frac{2}{d} ln\left(\frac{(n_r(\omega)+n_a)^2}{4n_r(\omega)n_a}A\right). \tag{2.37}$$

2.4 THz beam propagation

Since THz radiation bridges the gap between the microwave and optical regimes it combines aspects from both fields. While the microwave regime is characterized by the fact that most devices are comparable or much smaller in size to the wavelength of the radiation, the optical and infrared ranges are generally characterized by devices with dimensions much larger than the wavelength. As a consequence, the propagation of energy in the microwave region is generally in the form of single or low-order-mode guided waves in hollow core metallic waveguides. In contrast visible light typically is guided in multimode dielectric waveguides or via free-space propagation. There are of course exceptions, such as single-mode propagation in optical fibers. However, propagation in the visible can be described in terms of geometrical optics. Free space propagation of THz waves exceeds the limitations of geometrical optics and is characterized by quasi-optical propagation. This special feature of THz radiation has to be considered for optimized free beam optics. Another aspect is waveguiding in the THz region. THz waveguiding is possible both with metallic and dielectric waveguides, however, both concepts have difficulties. Over the next pages we will discuss those topics in the scope required for this thesis. A more detailed study can be found for instance in reference [69] or [70].

2.4.1 Quasi-Optical Systems

For THz optical systems an important aspect is the control of lateral extent and mode quality of a THz beam. Typically in such systems, the THz beam is focused onto some components with a spot size comparable to its wavelength. Hereby diffraction is of great importance to describe the beam propagation. Quasi optics deals with such cases where a beam of long wavelength propagates in free space under the influence of strong diffraction. For a monochromatic and linearly polarized electromagnetic wave in free space the electrical field is given by:

$$\mathbf{E(r,t)} = e_x E(x,y,z) e^{-i\omega t} \tag{2.38}$$

The wave equation (2.5) takes the form of the Helmholtz equation

$$\nabla^2 E(x,y,z) + k^2 E(x,y,z) = 0, \tag{2.39}$$

with the wave number $k = \omega/c = 2\pi/\lambda$. For the beam propagation along the z-axis, the electric field can be written as

$$E(x, y, z) = \Psi(x, y, z)e^{ikz}, \tag{2.40}$$

where the field amplitude $\Psi(x, y, z)$ varies slowly along the z-axis. With the paraxial approximation

$$\left|\frac{\partial^2\Psi}{\partial z^2}\right| << 2k\left|\frac{\partial\Psi}{\partial z}\right|, \tag{2.41}$$

and substitution of equation 2.40 into equation 2.39 leads to the Helmholtz equation in paraxial approximation

$$\frac{\partial^2\Psi}{\partial x^2} + \frac{\partial^2\Psi}{\partial y^2} + 2ik\frac{\partial\Psi}{\partial z} = 0, \tag{2.42}$$

in which the beam is confined to the vicinity of the propagation axis. The solutions to this wave equation are Hermite polynomials in rectangular coordinates and Laguerre polynomials in cylindrical coordinates with a Gaussian function as an envelope. As the spot size is minimized at $z = 0$ and $r = \sqrt{x^2 + y^2}$, the solutions can be written in the form $\Psi(x, y, z) = \Psi(r, z)$. The field amplitude at a distance z from the beam waist is given by [71]

$$\Psi(r, z) = \frac{w_0}{w(z)}e^{-r^2/w(z)^2}e^{ikr^2/2R(z)+i\phi(z)}, \tag{2.43}$$

where the beam parameters, $w(z)$, $R(z)$, and $\phi(z)$, are defined as

$$w(z) = w_0\left[1 + (\frac{z}{z_0})^2\right]^{\frac{1}{2}}, \tag{2.44}$$

$$R(z) = z\left[1 + (\frac{z_0}{z})^2\right], \tag{2.45}$$

$$\phi(z) = tan^{-1}\left(\frac{z}{z_0}\right), \tag{2.46}$$

with the Rayleigh length

$$z_0 = \frac{1}{2} k w_0^2 = \frac{\pi w_0^2}{\lambda}, \tag{2.47}$$

and w_0 is called the beam waist radius. Hereby the spot size at the focal plane is conventionally defined by the beam diameter $2w_0$. In free space propagation of THz radiation, the lower order modes are dominant in general. Therefore only the lowest-order solutions are considered. The lateral beam profile in the plane of the beam waist takes the Gaussian function

$$\Psi(r,0) = e^{-r^2/w_0^2}, \tag{2.48}$$

Equation 2.48 also implies that the beam has a flat phase front at the beam waist. The beam expands away from the focal plane, while its profile remains Gaussian. In figure 2.9 the Gaussian beam expansion near the beam waist is shown.

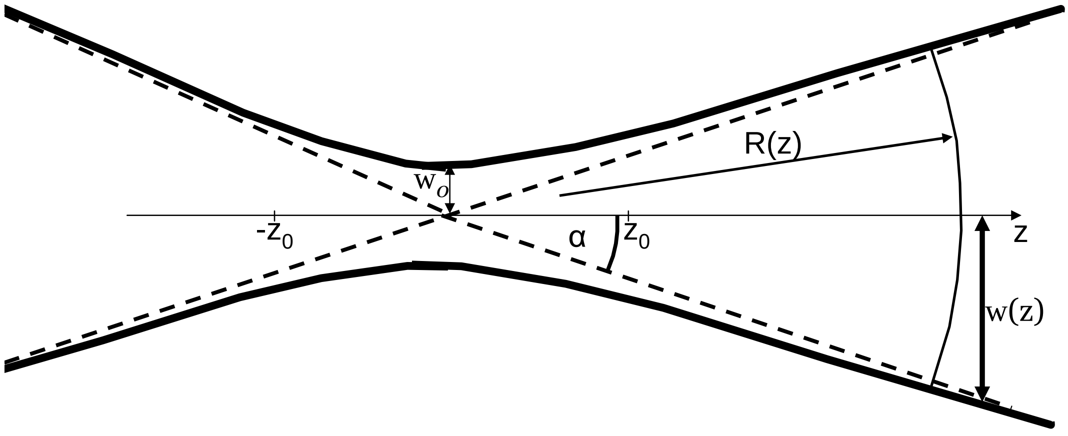

Figure 2.9: Beam waist of a Gaussian beam.

Within the confocal range, $-z_0 < z < z_0$ the beam divergence is insignificant $w(\pm z_0) = \sqrt{2} w_0$. Here the field amplitude reduces to 1/e of its on-axis maximum at $z = \pm z_0$.

The equiphase surface forms the spherical phase front, having the radius of curvature $R(z)$. The phase delay $\phi(z)$ is called the Gouy phase of the beam. The

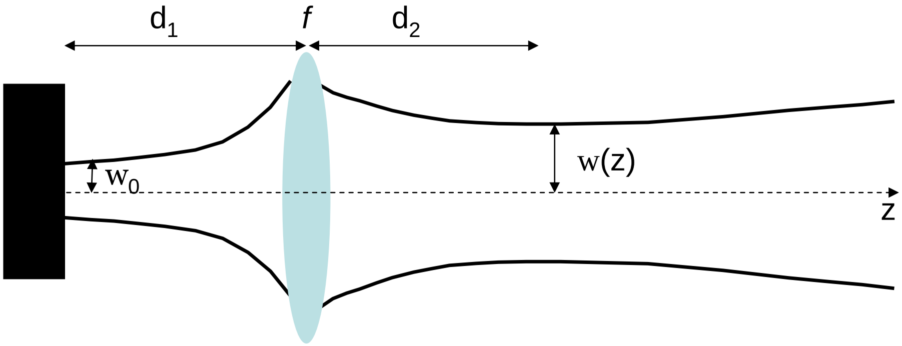

Figure 2.10: Focusing of a Gaussian beam with a thin lens of focal length f.

divergence of the beam is determined by the angle

$$\alpha = \lim_{z \to \infty} tan^{-1} \left[\frac{w(z)}{z} \right] = tan^{-1} \left(\frac{w_0}{z_0} \right) . \tag{2.49}$$

If the beam diameter is much larger than the wavelength ($w_0 >> \lambda$), the divergence angle approaches

$$\alpha \cong \frac{\lambda}{\pi w_0} . \tag{2.50}$$

A simple and practical application is the focusing of a Gaussian beam by a focusing element. In figure 2.10 the focusing by a thin lens is illustrated.

The beam waist can be determined in terms of ray matrices. As a result of such a consideration (see references [71, 72]), we obtain following relations for the beam waists

$$w(z) = w_0 \cdot \frac{f}{[(z-f)^2 + z_0^2]^{1/2}}, \tag{2.51}$$

$$d_2 = f \cdot \left[\frac{d_1(d_1 - f) + z_0^2}{(d_1 - f)^2 + z_0^2} \right], \tag{2.52}$$

where $z_0 = \pi w_0^2 / \lambda$ is the Rayleigh length of the beam waist w_0. Figure 2.11 shows the propagation of THz waves for several frequencies, plotted is the beam waist as a function of the position z along the propagation direction. The THz emitter is placed at the position $z = 0$ with an initial waist of $w_0 = 2.75\,mm$ The lens is positioned at $z = 120\,mm$. It is clearly illustrated that the beam waist is frequency dependent, with higher frequencies having a smaller diameter than lower frequencies. For an accurate imaging this frequency dependent behavior has to be considered. A perfect imaging can be realized by using a telescope with a pair of lenses (or mirrors), separated by the sum of their focal length. The magnification and the focal plane location are then the same as those of geometrical optics. However, for lower frequencies the paraxial approximation does not hold and such a description of the beam propagation is invalid. In the limit where $w_0/\lambda << 1$, one can use Bethe's diffraction theory [73, 74] to describe the propagation of the THz beam[2]. In this regime, the typical diffraction length, analogous to the Rayleigh length in Gaussian optics, is given by $z_B = 2\pi^2 \cdot w_0^3/\lambda^2$. This shows that low frequencies diffract much quicker than predicted by the paraxial approximation.

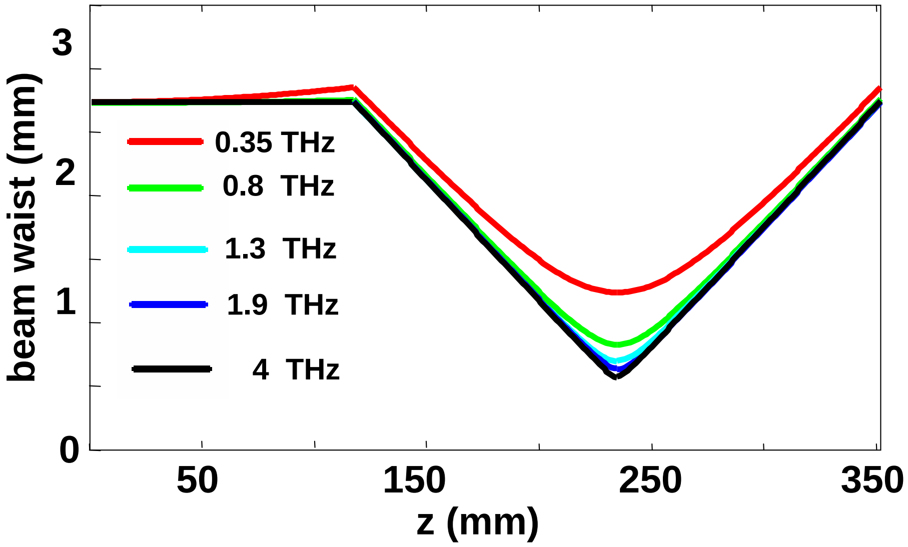

Figure 2.11: Calculated beam waist of a Gaussian beam focused by a thin lens with $f = 120\,mm$ and $\omega_0 = 2.75\,mm$ along the propagation axis z.

---

[2] The analogy is not perfectly exact, because in Bethe's theory diffraction of a plane wave is studied using a conducting plate with a hole whose size is small compared to the wavelength of the radiation. In our case the boundary conditions are slightly different, since there is no conducting medium around. Therefore in Bethe's case the fields might fall off much sharper then they really do.

However, for frequencies above 0.5 THz Gaussian optics gives a good description of the THz beam propagation [60, 72].

2.4.2 THz wave-guiding

Numerous wave-guiding techniques have been investigated for the propagation of broadband THz pulses, using hollow metallic structures [75], dielectric fibers [76], dielectric slabs [77], parallel-plate structures [78, 79], photonic crystal fibers [80], coaxial lines [81], metal wires [82–84], and metallic slits [85]. These have demonstrated great potential for applications such as high-speed interconnects, spectroscopy, sensing, imaging, microscopy, and signal processing. However, a THz wave-guiding technique that provides a complete solution, satisfying all of the requirements of low loss, low dispersion, single-mode propagation, with good energy confinement, and efficient input coupling, is still missing. For example, the use of the dominant transverse-magnetic (TM_0) mode of a dielectric slab waveguide or the Sommerfeld mode of a cylindrical metal wire can provide extremely low intrinsic losses, but the former suffers from high group velocity dispersion (GVD) [77], while the latter is prone to radiation losses even for large bending radii and suffers from poor coupling from a linearly polarized input beam [83, 84]. Additionally, the use of the transverse-electromagnetic (TEM) mode of a parallel-plate waveguide can provide low losses, negligible dispersion and very good coupling, but cannot provide complete confinement, due to the one-dimensional nature of the guide. Recent studies [79] discussed the possibility of achieving extremely low losses (in the dB/km range) and good energy confinement via the use of the TE_1 mode in parallel-plate waveguides, although under single frequency or continuous-wave operation. In these studies the typical drawback of a low-frequency cutoff for the TE_1 mode has been minimized by using transverse-concave metal plates. In general, these THz waveguides can be divided into three rough types according to where the THz wave is guided. The first are metallic tubes or rectangular waveguides where the THz wave is guided inside the hollow space. Second, plasmonic waveguides where the THz wave is guided at a metal-dielectric interface (e.g. metal wires). And the third are dielectric and photonic crystal waveguides, where the light is confined to the core by total internal reflection or by a photonic crystal creating a photonic "band structure". Nevertheless, is similar the form of the wave equation describing the THz propagation in the waveguides, while the main differences are given by the boundary conditions. Representatively we will discuss the propagation of a transverse electric (TE) THz mode in a GaAs slab with a width of $d = 400\,\mu m$ and a length of $2\,mm$. The top and bottom side is metalized by a thin Au/Cr layer. The wave equation (2.5) for an incident wave $E = (0, 0, E_{0z})$, of the electrical field inside the waveguide is then

$$\nabla \times (\nabla \times E) - n^2 k_0^2 E = 0. \tag{2.53}$$

Thus, the field pattern of the THz wave is determined by the refractive index n. We assumed a refractive index of $n_{GaAs} = 3.612$ in the GaAs slab and a refractive index of $n_{air} = 1$ outside the slab. As boundary condition it is assumed that the upper and lower side of the slab are perfectly conducting due to the additional metallization layer, therefore the E_z component has to be zero at these surfaces. Figure 2.12 shows the calculated electric field (blue indicates a field minimum and red a maximum) for 0.5 THz, 1 THz, and 1.5 THz from top to bottom. In figure 2.12 it is clearly demonstrated that the characteristics of the waveguide changes from single mode (0.5 THz) to a multimode (1.5 THz) characteristics, within 1 THz variation. At higher frequencies other modes than the TE_{10} appear, causing a "dirty" signal. The input wave then splits into several modes that are hard to control without having large power losses at the output of the waveguide. This is a challenge that has to be considered by the design of a THz waveguide for broadband THz pulses with a typical bandwidth of several THz.

This kind of waveguide can be treated analytically as well, and is therefore ideal for testing our numerical model. The analytical solution for wave propagating in x-direction (coordinate system in figure 2.12) has a discrete set of solutions of the form of

$$E_m(x, y, z, t) = E_0 \cdot sin(m\pi y/d) \cdot e^{-i(kx+\omega t)}. \tag{2.54}$$

The z-component of the electrical field E at a fixed position x is then determined by $E_z(y) = E_0 sin(\frac{m\pi y}{d})$, which is exactly the cross section[3] of our numerical solution along the y-direction. For 0.5 THz this solution is the TE_1 mode (m=1). The ana-

---

[3] cross section parallel to y coordinate

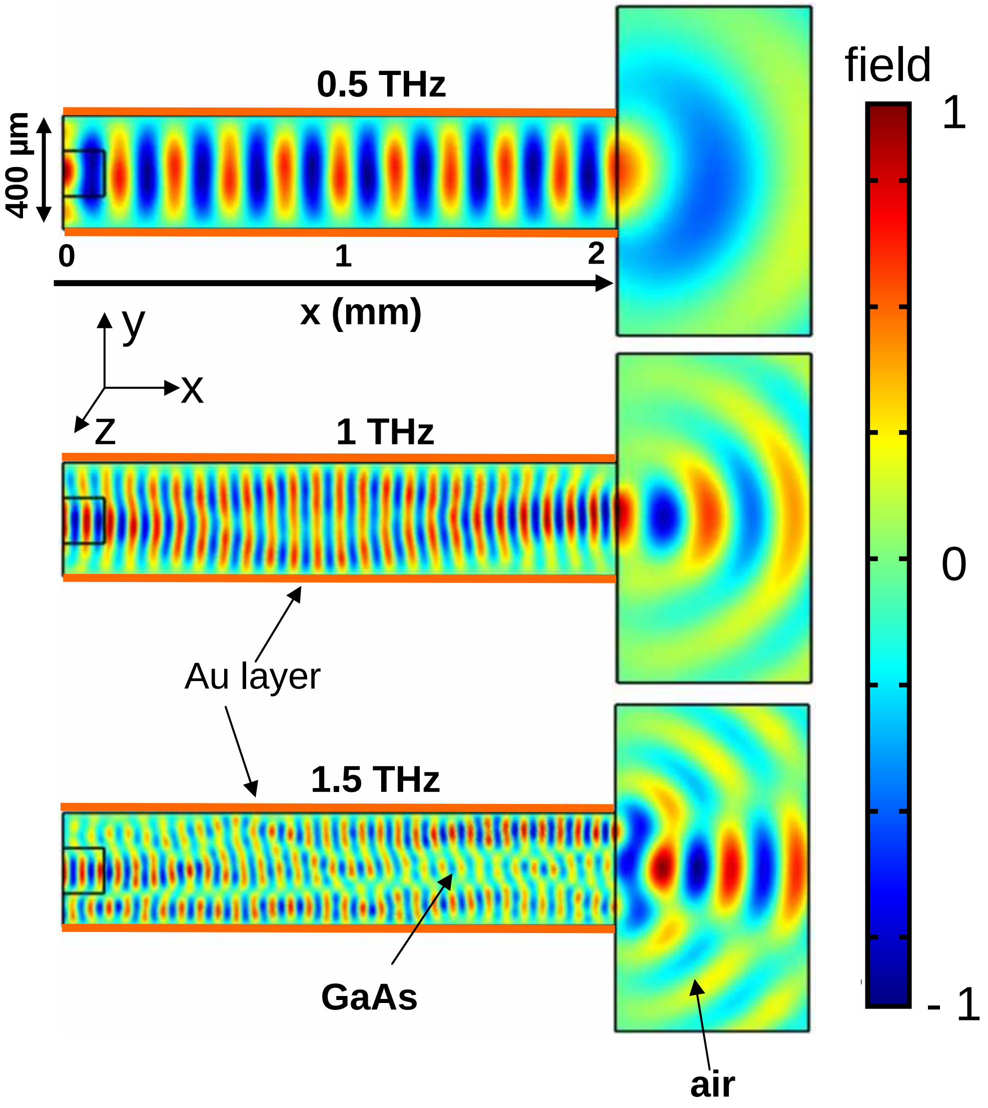

Figure 2.12: Field distribution of THz waves for different frequencies in a GaAs slab (left) and its transition to free space (right). The calculations were done numerically by using the commercial software Comsol [86]. Red are the maxima, blue the minima and green represents the zero-crossings of the electrical field. As source for the THz radiation a dipole is placed in the black square at the left end of the slab.

lytical model does not include reflections of the THz wave at the interface between GaAs-air. In the numerical model this is considered and results in opposed traveling waves superimposing with each other. This effect becomes more important for higher THz frequencies, therefore the modes are not so clearly identifiable in the numerical calculation (e.g. for 1.5 THz). Nevertheless, the good agreement between both solutions at the lower THz frequencies verifies our numerical model. We will need this for a simulation later in chapter 5.

3 Scalable photoconductive THz emitters and detectors

The disadvantage of conventional small aperture photoconductive devices, as presented in section 2.1.3, is the small active area in the $10\,\mu\text{m}^2$ range, demanding tight focusing of the NIR beam. This leads to high excitation densities for higher pulse powers. Because of that, the saturation level of an emitter is reached quickly. Furthermore, the gating beams for these antennas need to be aligned precisely at the photoconductive gap. Additionally, the laser power has to be reduced to avoid damaging the device through excessive heat generation. This leads to a reduction in usable laser power and therefore to a reduced efficiency [60].

Because of the large electrode distances, a large aperture emitter needs higher voltages than small aperture devices to obtain the same bias fields. Usually the electrode distance in such emitters are larger then the spot size of the stimulating laser. Therefore another drawback is that the excited carriers can not reach the electrodes on a time scale which is shorter then the duration of the generated THz pulse. This leads to the formation of a contrarily oriented dipole between the electrodes screening the external bias field. As a result the THz emission saturates rapidly by increasing the excitation densities [87]. It has been shown that semilarge-aperture emitters, i.e., emitters where the electrode gap is comparable to the central wavelength of the emitted radiation, are very efficient [88]. In this chapter another type of THz device is presented without the disadvantages of those conventional designs.

Parts of this chapter have been published in Appl. Phys. Lett. 91, 081109 (2007); Appl. Phys. Lett. 93, 101102 (2008); IEEE J.Sel. Top. Quantum Electron. 14, 449 (2008), and Opt. Express 17, 1571 (2009).

3.1 Chip Layout

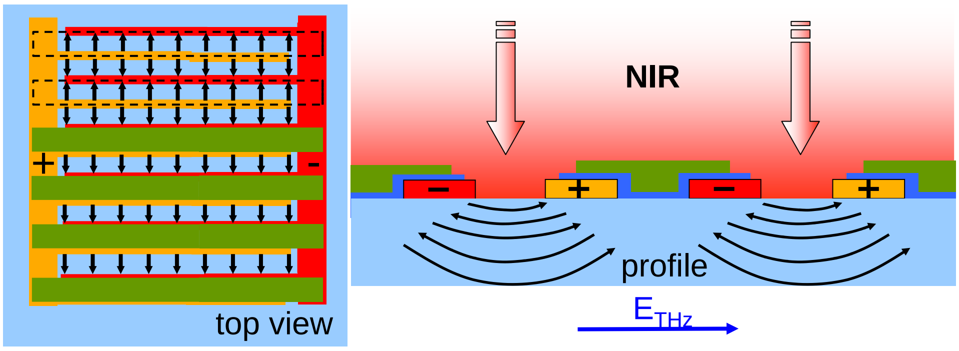

Figure 3.1: Layout of the scalable Terahertz emitter in profile and top view. The first metallization is an interdigitated finger electrode (red and orange) fabricated on a substrate like SI GaAs (light-blue). The spacing between the individual fingers is 5 μm. A second metallization (green) insulated from the first shadows every second spacing of the interdigitated structure. The arrows on the left indicate the bias field direction when an external voltage is applied. The active area can scale from 1 mm^2 to 1 cm^2. The arrows on the right side illustrate the radiated THz field from the active regions.

The approach of the Rossendorf scalable photoconductive device was based on an idea by Thomas Dekorsy. It combines the advantages of an high bias field with small electrode distances and a large active area by scaling the active region. The basis is an interdigitated electrode as shown in figure 3.1 and an additional metallization shadowing every second spacing. The second metallization is insulated from the first. If an external voltage is being applied to the electrodes, a uniform bias field is initialized as indicated by the arrows in figure 3.1. In general, the substrate is a semiconductor with a high carrier mobility and a bandstructure which allows efficient excitation with the applied laser system. By illuminating this structure with a fs Titanium Sapphire laser (Ti:Sa) at 800 nm semi-insulating (SI) GaAs is an adequate material. In that case carriers are generated and accelerated in a uniform direction. Because of that, the elementary THz waves which are generated in the non-shadowed regions interfere constructively in the far field. As a consequence of the THz emission by that intrinsic carrier acceleration, the bandwidth of the emitted radiation is not limited by a resonant characteristics. The polarization of the emitted radiation is determined by the structure of the electrodes. For the interdigitated electrodes in figure 3.1 the polarization is linear and the field vector

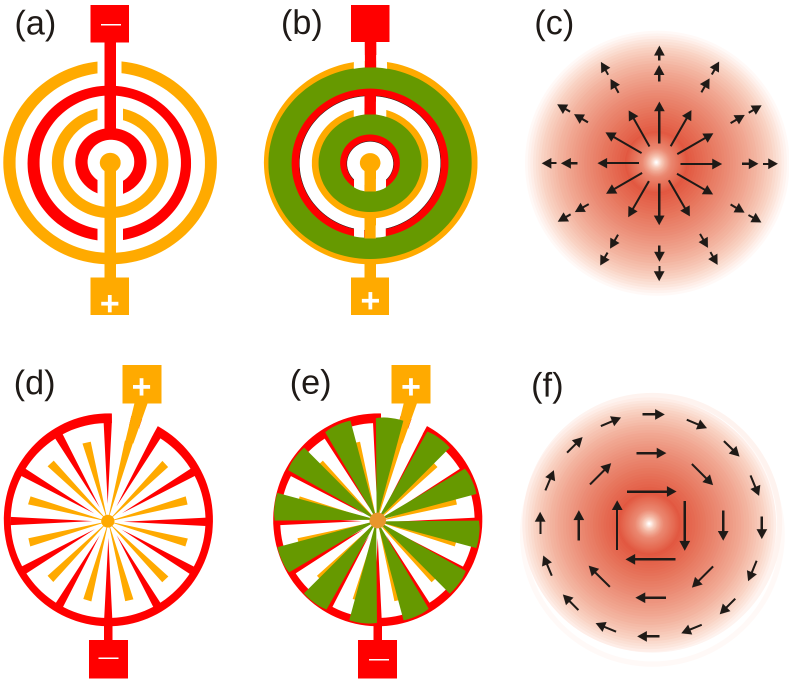

Figure 3.2: Draft of emitter for radial (a-c) and azimuthal (d-f) polarized THz radiation. In (a,d) the electrode geometry of the first metallization and in (b,e) with second metallization (green) is illustrated. (c,f) shows the resulting mode patterns. The arrows indicate the electric field and the shade the intensity distribution.

of the THz wave is orientated perpendicular to the electrodes.

In principle this approach can be utilized to generate THz beams of various field patterns. Because metal electrodes act as equipotential lines, the field pattern is then always normal to their electrode geometry. Emitters for radially polarized modes consist of concentric ring electrodes. The distance and width of the electrodes are 5 μm each. Emitters for azimuthally polarized modes consist of a circular arrangement of metalized sectors. The principal layout of the electrode geometry for radially and azimuthally polarized THz radiation is shown in figure 3.2 (a) and (d), respectively. In figure 3.2 (b) and (e) the second metalization is illustrated (green), which prevents the destructive interference of THz wavelets from neighboring electrode gaps. This principle is adopted from the microstructured devices for linearly polarized radiation with parallel metalization lines. The resulting mode patterns are shown in figure 3.2 (c) and (f). The diameter of the emitters are

2 mm. The emitters for radially polarized radiation contain 100 gaps between the electrodes, the ones for azimuthally polarized radiation comprise 92 gaps. Due to the fine patterning, the slight breaking of radial symmetry by the metalization lines, which connect all parts of the electrodes of similar polarity, is negligible.

3.1.1 Manufacturing

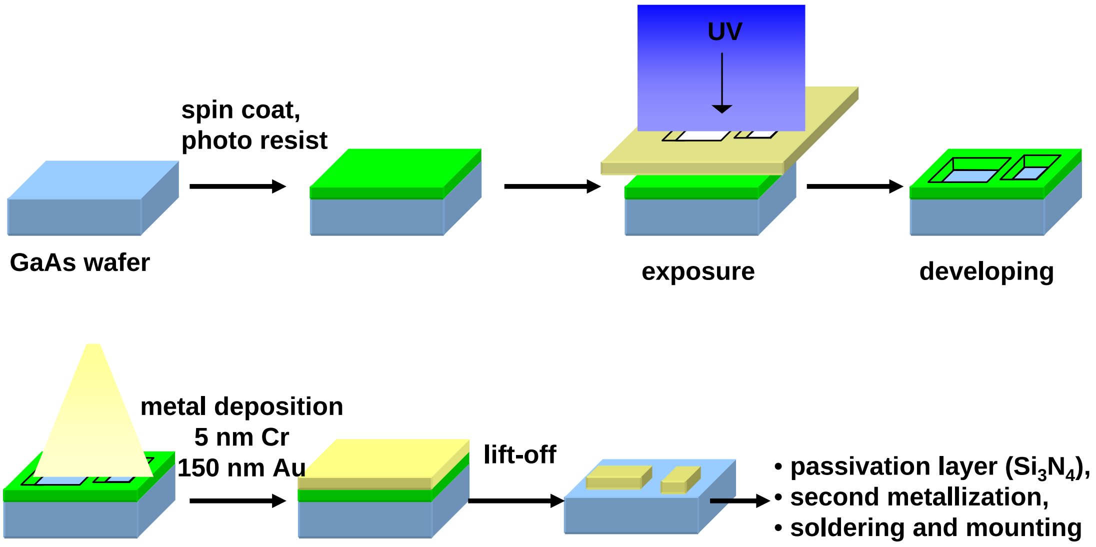

Figure 3.3: Scheme of the photolithographic process for manufacturing the THz devices.

For the purpose of our research the chips were processed, in a class 100 clean room at the “Process Technology Department” of our institute. In addition, the chips for the low volume production were manufactured by the Gesellschaft für Silizium-Mikrosysteme mbH (GeSiM). The wafers were polished on both sides and either 350 μm or 625 μm thick. The specified electron mobility was $> 6000\,\mathrm{cm}^2/\mathrm{Vs}$ and the resistivity of the semi-insulating wafers was $> 10^7\,\Omega\mathrm{cm}$. In figure 3.3 the first metallization process is illustrated. The substrates were cleaned by trichloroethylene, acetone and methanol in an ultrasonic bath. The cleaned wafers were spin coated with photoresist and exposed to UV light through a chromium mask with a negative of the electrode structures. After developing the photoresist 5 nm chromium and 150 nm to 200 nm gold were deposited. The lift off was carried out in a ultrasonic bath with acetone. After cleaning with acetone and drying with nitrogen gas the insulating layer was deposited. For this passivation silicon nitride (Si_3N_4) was used which was deposited by Plasma Enhanced Chemical Vapor Deposition (PECVD) [89]. These layers ranged in thickness from 300 nm up to 1 μm. For opening the contact pads Reactive Ion Etching (RIE) was employed in combination with an additional photolithography step. Finally the second metallization, which shadows every second spacing, was realized by a similar process as the first metallization. Here the layer thickness was 5 nm Cr and 50 nm Au. The electrical contacts for applying the bias field or measuring the photocurrent were realized by soldering.

3.2 Scalable antenna as an emitter

The suitability of the scalable antenna to act as an emitter excited with various laser systems is analysed in the following sections.

3.2.1 Performance and operating parameters

An optimum excitation condition exists when the spot size of the excitation beam is similar to the main emitted wavelength. This wavelength is typically around 300 μm [60]. Figure 3.4 (a) illustrates the experimental setup. The THz radiation from the emitter was refocused on the EOS crystal (230 μm ZnTe) by two off-axis parabolic mirrors. The terahertz signal and the sampling beam are combined by a tin doped indium oxide (ITO) coated mirror. Temporal resolution is achieved by mechanical delay of the sampling beam. In figure 3.4 (b) the dependences of the THz field amplitude on the bias field is plotted. It shows that over the investigated range from 8 to 80 kV/cm and an excitation fluence of 8 $\frac{\mu J}{cm^2}$ the field amplitude scales linearly with the bias field. Other research groups observed saturation of THz emission for bias fields over 100 kV/cm [91–93]. In these articles the saturation is attributed to a faster side valley transfer of electrons for higher bias fields. After interband excitation electrons in GaAs can transfer into the L- or even the X-valley of the bandstructure as soon as the bias field is above 5 kV/cm. Because of the higher effective mass these carriers are not accelerated efficiently any more. Furthermore, these carriers have an velocity overshoot prior to intervalley scattering and are decelerated in the side valley. For bias fields above 200 kV/cm the

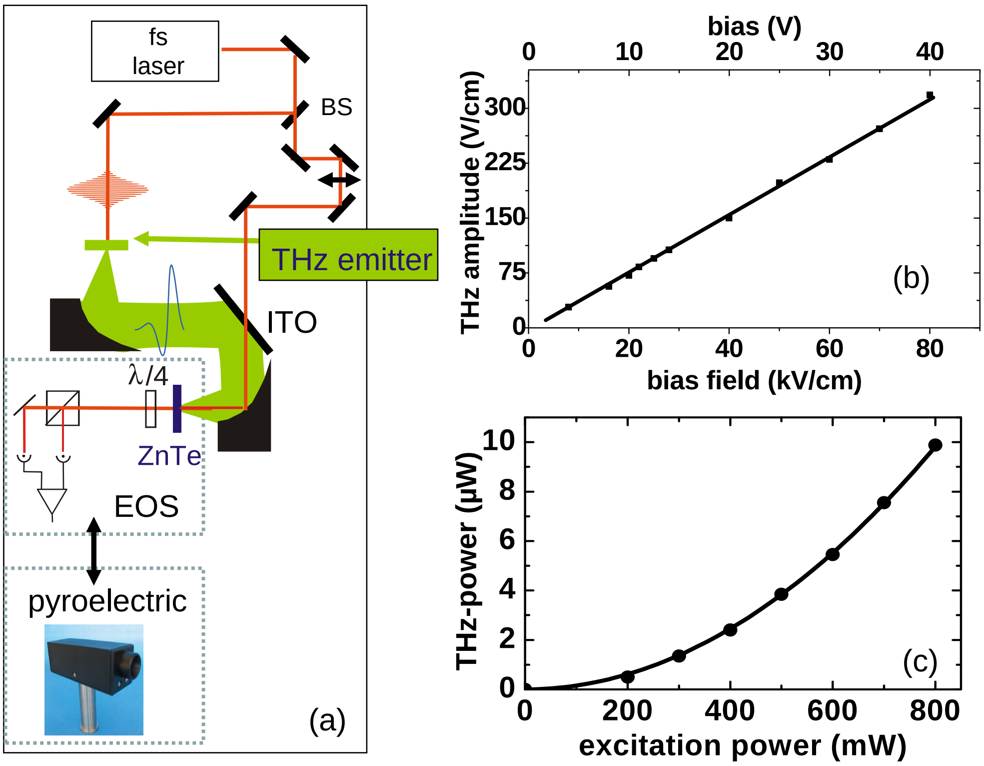

Figure 3.4: Graphic (a) illustrates the experimental setup, excitation was with the Tsunami Laser system from Spectra Physics (see appendix A.1). Graphic (b) shows the THz field amplitude, measured by EOS in a 230 μm thick ZnTe crystal, in dependence on the accelerating bias field with an excitation spot size of 300 μm (FWHM) and an excitation power of 470 mW (Black squares - data points, solid line - linear fit). In (c) the dependence of the emitted THz power on the excitation power at a bias of 10 V is shown. The power was measured with a pyroelectric detector (Black squares - data points, solid line - square fit).

electrons in GaAs can accumulate the energy on a much shorter time scale, and the side valley transfer can occur already during the excitation by the 70 fs laser pulse. Hence, their contribution to the radiated field of the THz trace is minimal and saturation is observed [94]. However, it was found that this effect increases the bandwidth of the emitted radiation [95].
Figure 3.4 (c) illustrates the dependences of the THz power on the optical excitation power. The bias at the emitter was 10 V. As anticipated, the detected THz-power rises quadratically with the optical excitation power, since the THz field amplitude depends linearly on the number of accelerated carriers. Hereby 800 mW corresponds

to a fluence of about 15 $\frac{\mu J}{cm^2}$. Experiments with the amplified laser system (A.1.2) showed that this is true for fluences of up to 25 $\frac{\mu J}{cm^2}$ [72]. For higher excitation fluences saturation occurs due to screening of the bias field by the generated THz field [87,96–98]. Saturation by carrier screening is not significant since the electrode distance (5 μm) is always small relative to the excitation spot size (300 μm) [95].

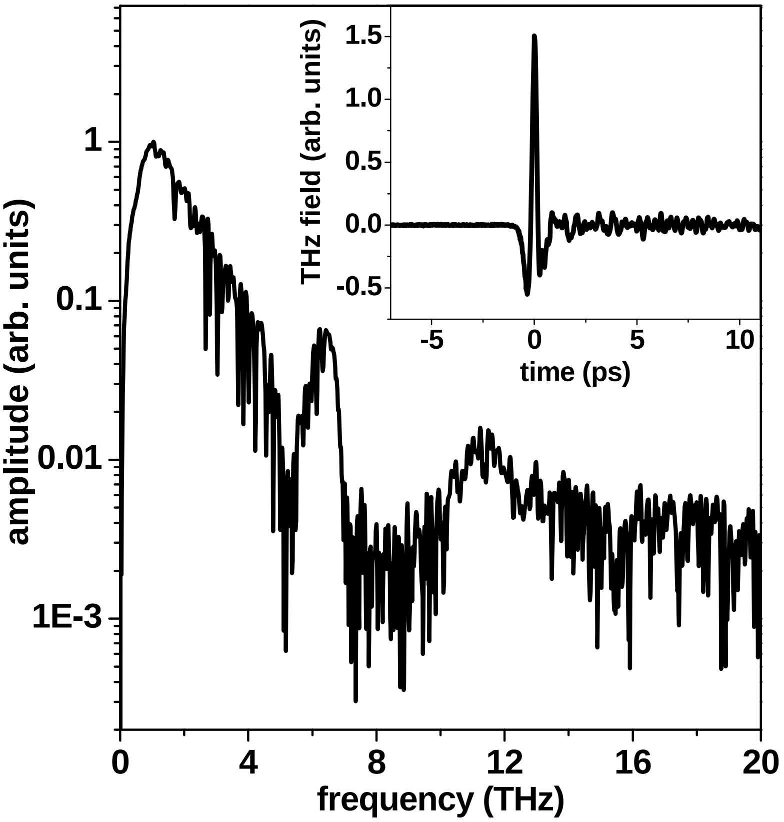

Figure 3.5: Amplitude spectrum and temporal waveform of the EOS signal from a scalable antenna based on a SI GaAs substrate. Excitation was with the 15 fs-titanium-sapphire-oscillator system (A.1.1).

To measure at higher THz frequencies, we applied EOS and ultrashort (15 fs) laser pulses to characterize the emission spectrum of a scalable antenna based on SI GaAs. Here the antenna was biased with 20 V and excited with 100 mW of optical power. The crystal for detection consisted of a 10 μm thick $\langle 110 \rangle$ oriented ZnTe active layer glued onto 1 mm ZnTe oriented in the $\langle 100 \rangle$ direction. The $\langle 100 \rangle$

oriented crystal delays reflected pulses in time. The Fourier transform and the detected THz waveform are shown in figure 3.5. The maximum of emission occurs at 1 THz with a 10 dB range from 0.16 to 4 THz. The spectrum extends up to about 12 THz. The broad dips in the spectrum from 4.5 to 6 THz and 6.8 to 11 THz are due to the reststrahlenbands of ZnTe and GaAs, respectively. The fine structure on the spectrum is caused by residual water vapour absorption in the setup, which is purged with dry nitrogen.

3.3 Scalabale emitter for excitation wavelengths above 1 μm

The availability of low-cost, stable and compact fiber lasers has stimulated research in PC antennas, which are based on substrates that allow interband excitation with wavelengths up to 1.55 μm. The challenge is to find small-gap materials with high resistivity and a short lifetime of the photo-excited carriers [99]. Low-temperature grown GaInAs and ion-irradiated GaInAs, both grown lattice-matched on InP, have been used as substrate materials for dipole emitter antennas [100, 101]. However, the resistivity of these materials is still too low for large-area emitters with interdigitated electrodes.

3.3.1 GaInAsN substrate

In this thesis a substrate material is investigated which is based on 1000 nm quaternary $Ga_{0.89}In_{0.11}As_{0.96}N_{0.04}$ on $\langle 001 \rangle$ GaAs grown in a Varian Gen II Modular molecular-beam epitaxy (MBE) system using Al, Ga, In and As solid sources and a rf nitrogen plasma source. The optimum growth temperature, which depends on the In-content of the structure, was in the range of 530 ° to 580 °C [103]. While the indium increases the lattice constant in the alloy the nitrogen lowers it, permitting a nearly lattice matched compound with an active layer of 1 μm on SI GaAs (left side in figure 3.6). As indicated on the right side of figure 3.6, both the indium and the nitrogen narrow the bandgap. Further optimization is achieved by an additional $Al_{0.3}Ga_{0.7}As/GaAs$ heterostructure layer (60 nm AlGaAs and 5 nm GaAs) as a barrier on top, giving rise to a higher resistance of the structure when contacted

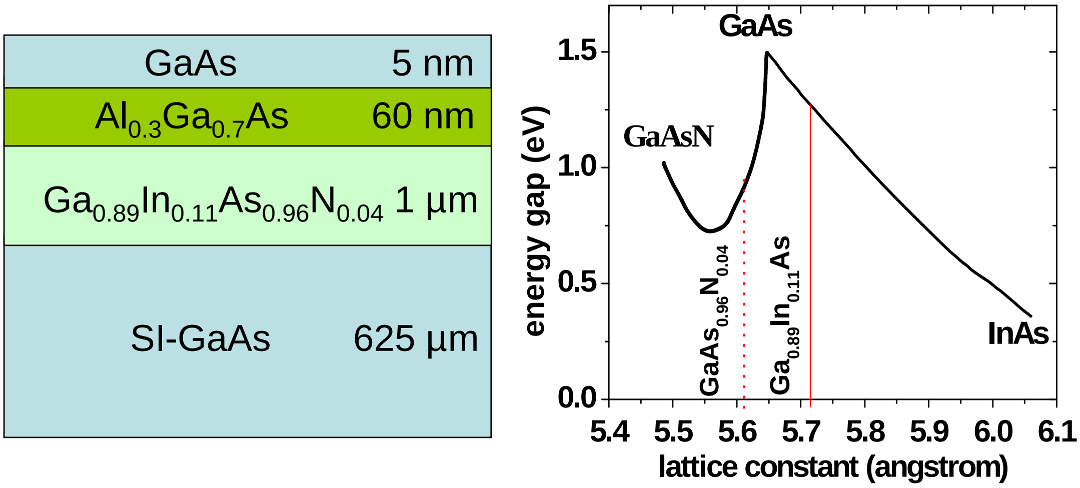

Figure 3.6: Left: Profile of the MBE grown substrate. Right: Bandgap of III-V compound semiconductors and their ternary alloys (lines) at zero temperature [104].

from the top.

Optical and electrical characterizations

Figure 3.7 shows the transmission spectrum of an emitter based on the structure of figure 3.6. The large oscillations are Fabry-Perot oscillations due to the Si_3N_4 layer of the device; the smaller ones occur from water absorptions [105]. The substrate shows a strong absorption below 1.5 μm. This step in the transmission spectrum is linked to the bandgap and therefore to the excitation of free carriers in the substrate [106]. The absorption coefficient of the GaInAsN layer at a wavelength of 1.3 μm is $1.5 \times 10^4\,\mathrm{cm}^{-1}$, which is comparable to the absorption coefficient of SI GaAs at 800 nm [107]. The substrate shows a resistivity of 500 kΩ cm, which is almost three orders of magnitude higher than previously reported for high resistivity GaInAs material grown on InP substrate [108]. After processing the interdigitated electrodes, the whole device resistance is 280 kΩ, enabling a high bias field of up to 60 kV/cm.

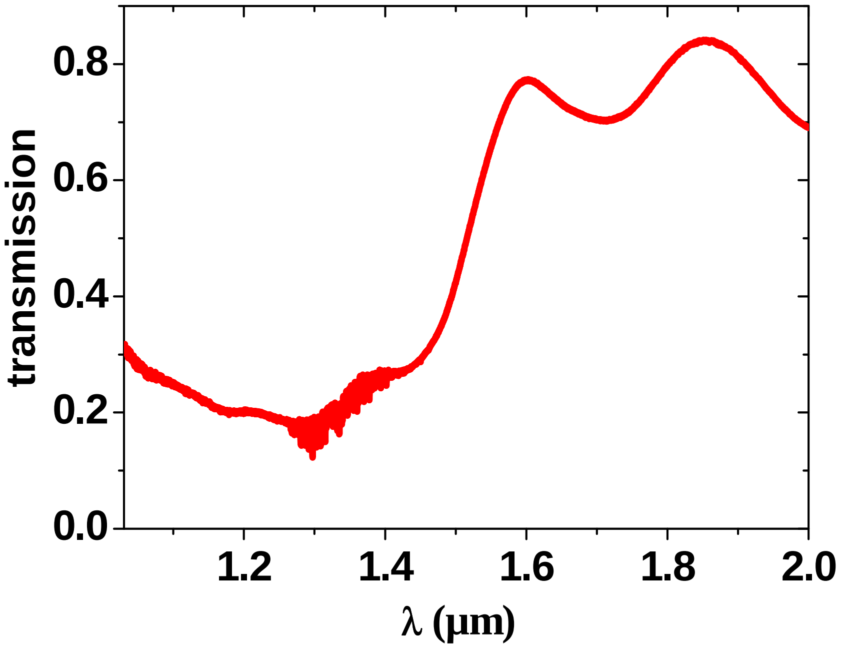

Figure 3.7: Transmission spectrum of the emitter based on a GaInAsN Substrate with AlGaAs heterostructure. The measurement was done with a Fourier Transform Infrared Spectrometer (FTIR) from Bruker GmbH (Equinox 55).

3.3.2 Experimental

For the following investigations we utilized pulses from an optical parametric oscillator (OPO) which is driven by a mode-locked femtosecond Ti:sapphire laser (Tsunami Spectra Physics -see appendix A.1.4). The signal beam of the OPO is tuneable between 1.1 and 1.5 μm. The pulse duration is on the order of 250 fs. While the signal from the OPO excites the emitter, a small part of the 820 nm beam from the Tsunami is split off before entering the OPO and is used for electro-optic sampling in a 1 mm thick $\langle 110 \rangle$ oriented ZnTe crystal. A rectangular voltage of 15 V with a duty cycle of 50 % and a frequency of 5 kHz serves as bias for the emitter. The terahertz signal and the sampling beam are again combined by a tin doped indium oxide coated mirror and focused on the ZnTe crystal by a pair of gold-coated off-axis parabolic mirrors. The transmitted sampling beam was separated in its vertical and horizontal components by a polarization sensitive beamsplitter cube. Balanced detection is performed using two photodiodes and a quarter-wave-

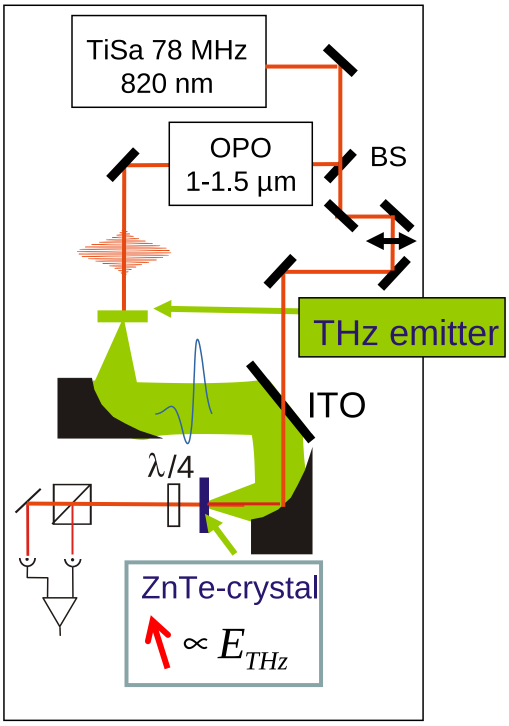

Figure 3.8: Setup for THz generation with the OPO and detection by electro-optic sampling. The red arrow in the box symbolises the polarization change of the sampling beam which is proportional to the THz field.

plate (figure 3.8). To prevent water absorption, the whole setup is purged with dry nitrogen.

3.3.3 Results and Discussion

Figure 3.9 displays the temporal waveform of the THz field, the Fourier transform amplitude is shown in the inset. The spectral maximum is around 1 THz and the usable bandwidth exceeds 2 THz. The terahertz trace is measured with a lock-in technique and has a signal-to-noise ratio of 400 at 100 ms lock-in time constant. The bandwidth of the emitted terahertz radiation is limited by the pulse duration of the OPO. For a 250 fs pulse the bandwidth is limited to about 2 THz. On the right side of figure 3.9 the dependency of the terahertz signal on the excitation wavelength is shown for constant excitation power. Between 1.1 and 1.34 μm the terahertz emission remains constant. For excitation wavelengths above 1.4 μm the

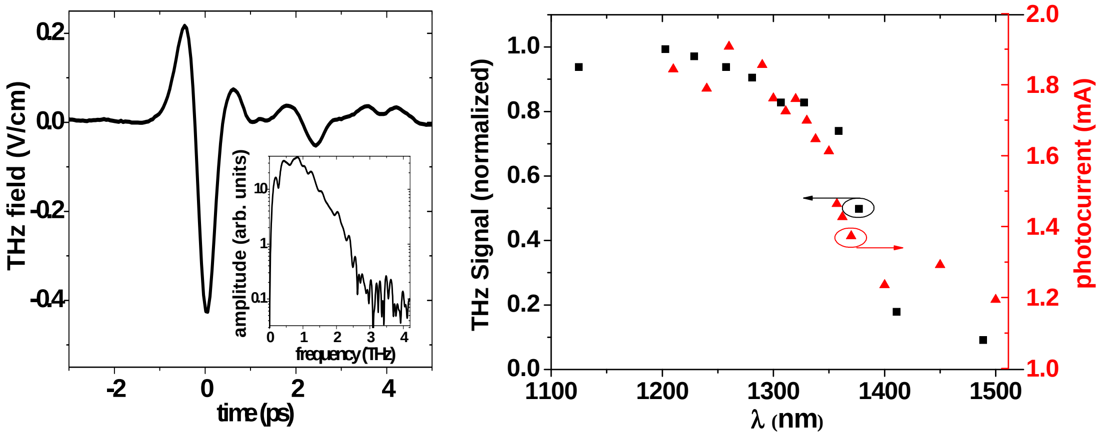

Figure 3.9: Left: Terahertz trace at 1.3 μm excitation wavelength and spectrum (inset) obtained by Fourier transformation. Right: Terahertz signal and photocurrent vs excitation wavelength (black squares and red triangles, respectively). The excitation power was kept constant at an average value of 25 mW.

signals are about five times smaller as compared to the shorter wavelength. This is consistent with the behavior of the measured photocurrents of the emitter. Based on the transmission spectrum in figure 3.7 where absorption is observed up to an excitation wavelength of 1.5 μm, we would expect the decrease in terahertz emission to occur at longer excitation wavelengths. Considering that the emitted terahertz field is proportional to the mobility times the excited carrier density, this can be attributed to a lower mobility of the electrons due to the modified band structure in a $GaInAsN$ alloy. Shan et al. [109] have found that in $Ga_{1-y}In_yAs_{1-x}N_x$ alloys the incorporation of nitrogen leads to a splitting of the conduction band into two nonparabolic subbands E$_+$(k) and E$_-$(k) (anticrossing model [110]). The nitrogen forms independently from the concentration a localized impurity level above the conduction band minimum of GaAs. The reason for the anticrossing is that this impurity level is within the conduction band and therefore resonant to the states in it. E$_+$(k) denotes the band which is above the original GaAs conduction band and E$_-$(k) is the lower band narrowing the bandgap in GaAsN. The curvature of the lower band E$_-$(k) is slightly smaller and therefore the effective electron mass higher and the mobility lower. This is an explanation of the observed wavelength dependency. Furthermore Fahy and colleagues have shown [111] that in those diluted nitride semiconductors an intrinsic upper bound on the carrier mobility exists. For a $GaAs_{1-x}N_x$ alloy with a nitrogen atomic concentration of 1% they estimated a carrier mobility of 1000 cm^2/Vs, which is six times lower than in SI GaAs. Particularly for smaller photon energies these limitations becomes important.

3.3.4 Comparison with conventional SI GaAs based emitter

Figure 3.10 a shows a comparison between a normal SI GaAs emitter and the GaInAsN/AlGaAs emitter at 800 nm excited with 500 mW optical power, 80 fs pulse duration and focused to a spot of 300 μm. For SI GaAs the signal is eight times higher than that for GaInAsN/AlGaAs. In principle the emitted THz field is proportional to the mobility multiplied by the excited carrier density. Since the number of excited carriers at 800 nm in GaInAsN/AlGaAs is at least equal to that in SI GaAs, we conclude from our data that the mobility in GaInAsN/AlGaAs is at least eight times lower than in SI GaAs (6000 cm^2 V^{-1} s^{-1}).

Figure 3.10 b shows the THz signal vs. excitation power for 800 nm, 1250 nm and 1350 nm wavelength. For the whole optical power range of the OPO up to a fluence of $1\,\mu J/cm^2$ we observe a linear dependence of the emitted THz field. The inset shows even higher optical powers obtained from direct excitation by the Ti:sapphire laser at 800 nm and up to 500 mW corresponding to a carrier density of 10^{17} cm^{-3}. This behavior is in contrast to low-temperature-grown GaInAs emitters on InP with smaller active areas operating at 1.56 μm, where saturation by carrier screening already occurs at some mW optical excitation powers [101, 102]. This is due to the scalability of our device, allowing larger excitation spot sizes[1], locally decreasing the carrier concentration between the electrodes, while the total number of excited carriers remains high.

---

[1] Typical in the order of 300 μm. (FWHM)

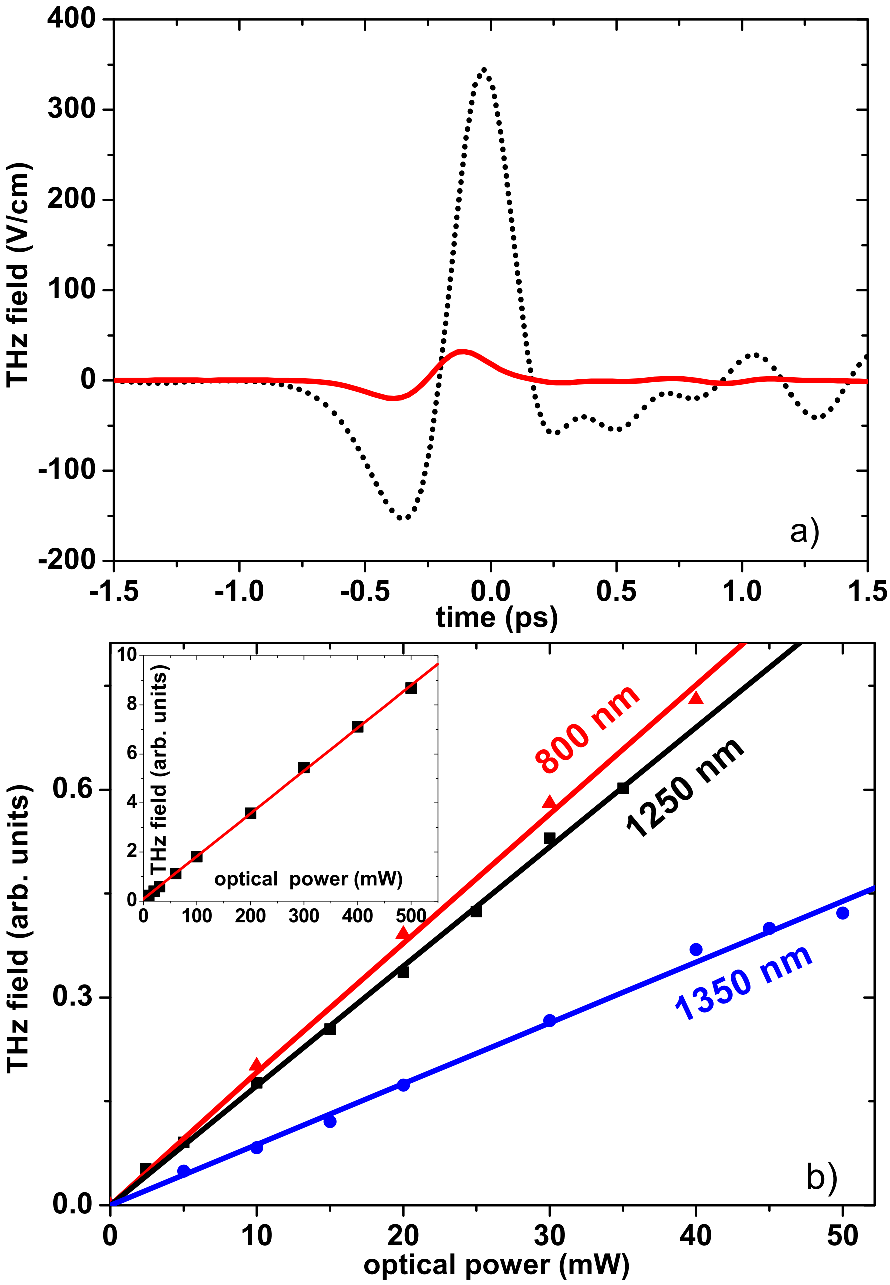

Figure 3.10: (a) Terahertz trace of a SI GaAs emitter (black dotted) in comparison to a GaInAsN/AlGaAs emitter (red solid) excited at 800 nm. (b) Terahertz field from the GaInAsN/AlGaAs emitter as a function of excitation power at 800, 1250, and 1350 nm (red triangles, black squares, and blue circles respectively). Solid lines are fits to the experimental data. The inset shows higher optical excitation powers reached at 800 nm.

3.4 THz detector properties

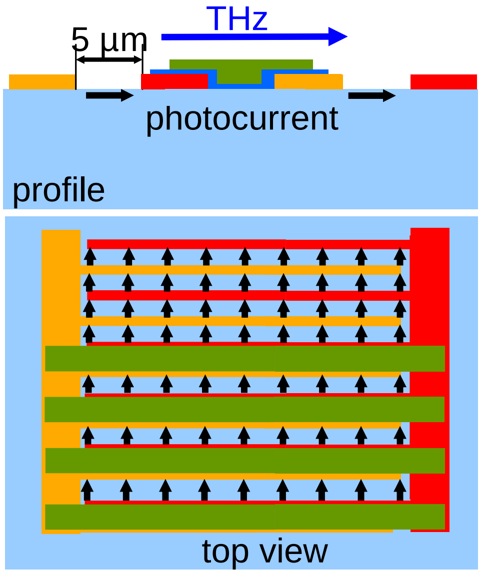

Figure 3.11: Layout of the scalable detector. The arrows indicate the photocurrent in the detector.

Unlike for emitters, there is not a wide variety of designs for detection antennas. Basically, dipole, strip line, bow tie, and logarithmic spiral antennas have been tested, with the dipole antenna being the most widely used design [44, 45]. A common feature of these detectors is a photoconductive gap of a few microns. Such antennas, and also detection based on EOS, require tight focusing of the THz beam as well as the gating beam. Furthermore, the antennas need a precise alignment of the gating beam to the photoconductive gap. The concept of the scalable device with interdigitated electrodes provides detectors that do not require tight focusing of either the THz beam or the near-infrared gating beam. These antennas detect THz radiation polarized perpendicular to the electrodes. In the absence of the second metallization (figure 3.11) photocurrent distributions from neighbouring gaps of the metallization would charge electrodes equally, which results in a zero net photocurrent. However, the complete structure (lower part of figure 3.11) allows a net current to flow.

3.4.1 Ion implanted GaAs

Samples were prepared by ion implantation of N^+ or As^+ into SI GaAs. All implantations were dual-energy implants; the energies and doses are listed in Table 3.1. The sample names are abbreviated with a suffix LD, MD, and HD, indicating low dose, medium dose, and high dose, respectively. In figure 3.12 (a) and (c), the implantation profiles calculated with the SRIM software [112] are shown for the N^+ and As^+ implantations, respectively. The aim was to achieve a fairly uniform distribution of trapping centers for the photogenerated carriers. The concentration

Sample name	E_1	d_1	E_2	d_2
	(MeV)	(cm^{-2})	(MeV)	(cm^{-2})
GaAs:N-LD	0.4	$1 \cdot 10^{12}$	0.9	$3 \cdot 10^{12}$
GaAs:N-MD	0.4	$1 \cdot 10^{13}$	0.9	$3 \cdot 10^{13}$
GaAs:N-HD	0.4	$1 \cdot 10^{14}$	0.9	$3 \cdot 10^{14}$
GaAs:As-MD	1	$8 \cdot 10^{13}$	2.4	$3.2 \cdot 10^{14}$
GaAs:As-HD	1	$2.5 \cdot 10^{15}$	2.4	$1 \cdot 10^{16}$

Table 3.1: Implantation parameters, namely, energy E and dose d for the dual-energy implantation of the samples

of generated vacancies is a measure for the trapping centers. The damage profiles (figure 3.12) indicate that the materials are modified to a depth of about 1.5 μm. Hence, all carriers generated with near-infrared radiation are created within the implanted region. Photoconductive devices were processed on the as-implanted materials and also on substrates that were annealed at 500 °C in N_2 ambient after implantation. During annealing, the samples were covered with a GaAs proximity cap. Annealing times were 10 and 30 min for the GaAs:N and the GaAs:As samples, respectively. In the following, sample names of the implanted substrates represent annealed substrates, except when the suffix "ai" for as-implanted is added. As a reference for the ion implanted samples, we fabricated devices based on LT-GaAs (layer thickness: 2 μm, growth temperature: 200 °C, annealed at 600 °C for 10 min in N_2 ambient with GaAs proximity cap) and on SI GaAs.

A useful technique for the characterization of lattice perturbations is Raman spectroscopy. Examples of such perturbations are lattice disorder, strain, symmetry breakdown, etc. Figure 3.13 shows the Stokes line of a Raman measurement from the LO phonon in GaAs (290 cm^{-1} [57]). The black solid curve belongs to SI GaAs, while the red and blue ones belong to various implantation doses of As into GaAs. On the left side in figure 3.13 the measurement was done with as-implanted samples while on the right side the samples were annealed as described above. For the as-implanted samples the Stokes line is shifted toward smaller energies. Furthermore line broadening and a shift of the base line on the low energy side is observed, indicating the damaging of the GaAs matrix by the As implantation [113–115]. After annealing the overlap of the stoke lines with the SI GaAs reference is much better, clearly demonstrating that annealing leads to substantial recovery of implantation

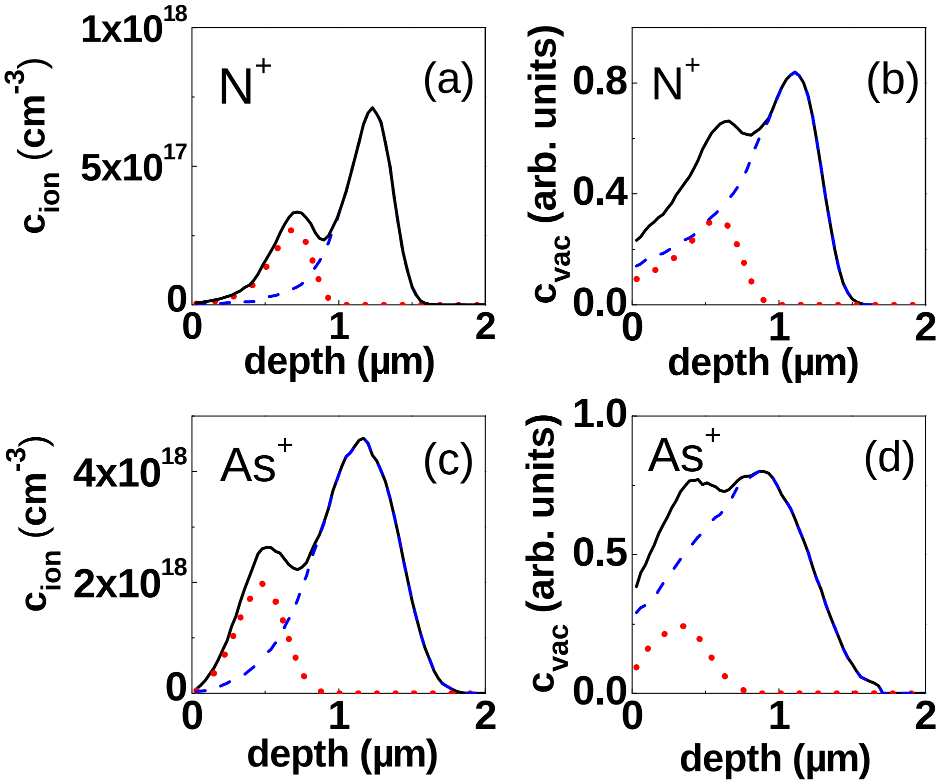

Figure 3.12: (a) Concentration of implanted ions for the GaAs:N-MD sample. (b) Concentration of vacancies for all GaAs:N samples. (c) Concentration of implanted ions for the GaAs:As-MD sample. (d) Concentration of vacancies for all GaAs:As samples. The red dotted line represents the implantation with E_1, the blue dashed line the implantation with E_2, and the black solid line the sum of the two.

damage.

3.4.2 Electrical Characterization

The dark resistance of all devices fabricated on as implanted materials, with the surprising exception of the GaAs:N-MD-ai sample, were below $10\,\Omega$, and therefore useless for either THz detectors or emitters. The structures based on GaAs:N-MD-ai yielded resistance values of $13\,\mathrm{k}\Omega$ and were suitable for THz experiments. Low dark currents are important for detectors, since the dark current is a source of noise. Annealing resulted in an increase of the device resistance by many orders of magnitude. As can be seen in (figure 3.14(a)), the dark current of the annealed GaAs:N-MD samples is five orders of magnitude lower than the dark current of

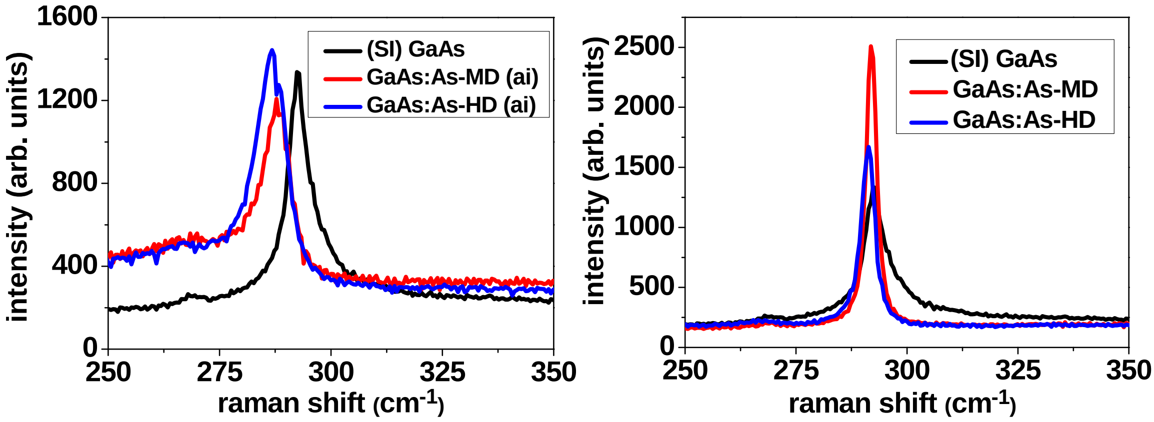

Figure 3.13: Stokes line of the Raman spectra for as implanted GaAs:As (left), and annealed GaAs:As (right) in reference to SI GaAs (black). Medium dose (MD) and high dose (HD) are colored in red and blue, respectively.

the GaAs:N-MD-ai sample. The fact that as-implanted GaAs has a low resistivity, that increases over several orders of magnitude by annealing, has been observed for various ion species [116–118]. It has been attributed to a hopping transport that vanishes when the trapping site density is decreased by annealing [116]. The dark currents of all implanted-and-annealed samples and of the LT-GaAs sample are in the sub-microampere range up to voltages of 30 V. Due to the geometry of the electrodes, high values of sheet resistance are essential. For example, the 13 kΩ of the as-implanted GaAs:N-MD-ai sample corresponds to a sheet resistance of $2.4 \times 10^8\,\Omega/\mathrm{sq}$ (resistivity $\approx 3.6 \times 10^4\,\Omega{\cdot}\mathrm{cm}$).

The photocurrents were measured for all samples illuminated with 800 nm radiation of 3, 6, and 10 mW. The responsivity of the devices was almost independent of the laser power in this range. For samples with highest photocurrents, a slightly sublinear dependence of the photocurrent on the laser power was observed. In figure 3.14(b), the responsivity of selected samples is plotted against the bias voltage. Since the absorption is expected to be similar for all substrates, the optical responsivity is a measure of the mobility and the carrier lifetime. The smallest values were found for the LT-GaAs sample followed by the GaAs:N-MD-ai sample. The responsivity decreased systematically with increasing dose for the implanted-and-annealed samples. Values of 0.31, 0.13, and 0.062 A/W were found for the GaAs:N-LD, GaAs:N-MD, and GaAs:N-HD sample, respectively (bias voltage 30 V, optical

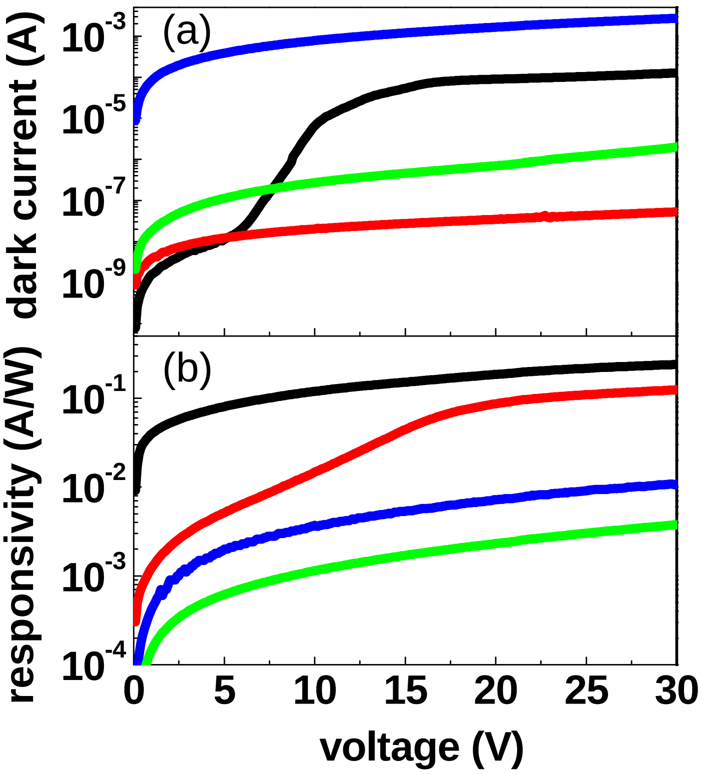

Figure 3.14: Detection characteristics (λ=800 nm, P=10 mW) for selected materials up to bias fields of 60 kV/cm (30 V). (a) Dark-current–voltage characteristics. (b) Responsivity-voltage dependence. The black line is for SI GaAs, the red for GaAs:N-MD, the blue for GaAs:N-MD-ai, and the green for LT-GaAs.

power 10 mW in all cases). This is consistent with the decreasing carrier lifetime with increasing dose [119].

The breakthrough voltage of the samples was not investigated systematically. The breakdown of SI GaAs was observed for some samples at fields of 80 and 120 kV/cm, the LT-GaAs samples could all be operated at fields of 100 kV/cm. These values are similar to values reported in the literature for conventional photoconductive antennas [44], indicating that the large area patterning of the antennas is of high quality.

3.4.3 Results and Discussion

For characterization, the detection antennas based on the different substrate materials are placed 23 mm behind a SI GaAs emitter antenna. The spot size (FWHM) and average power of the near-infrared radiation are 300 μm and 350 mW on the emitter and 400 μm and 70 mW on the detector antenna, respectively. A low-noise transimpedance amplifier is applied to amplify the photocurrents. The amplified signal is detected with a lock-in amplifier (integration time constant 100 ms). The emitter is biased with a rectangular voltage of 12.5 V with 50 % duty cycle at a frequency of 5 kHz, which serves as a reference for the lock-in detection. The spot size of the THz beam at the position of the detector is about 2 mm. In figure 3.15, the detected signals for the GaAs:N-based antennas are displayed. Comparing the signals for the different doses, the GaAs:N-LD signal contains more slow components and is more “monopolar,” while the signals for the higher doses are shorter in

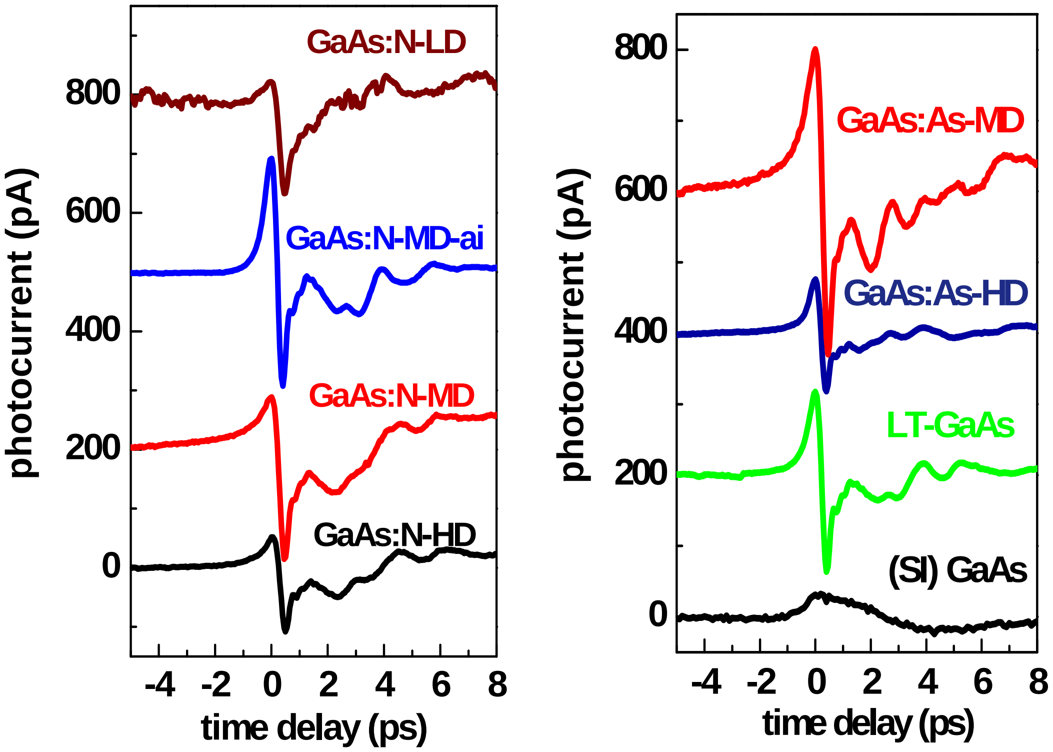

Figure 3.15: Detector photocurrents based on GaAs:N substrates (left), and photocurrent traces for the detectors based on GaAs:As, SI GaAs and LT-GaAs substrates (right).

time and have a more “bipolar” shape. This trend can also be seen comparing the signal of the GaAs:N-MD antenna, which still contains some slow components, with the signals of the GaAs:N-HD and GaAs:N-MD-ai sample. This indicates that the carrier lifetime is decreased with increasing dose, and that the annealed sample exhibits a longer lifetime as compared to the as-implanted sample (Section 2.2 figure 2.7). The long carrier lifetime of the low-dose sample also results in significantly more noise in the detected signal. The measured signals for the other detection antennas are displayed on the right side in figure 3.15.

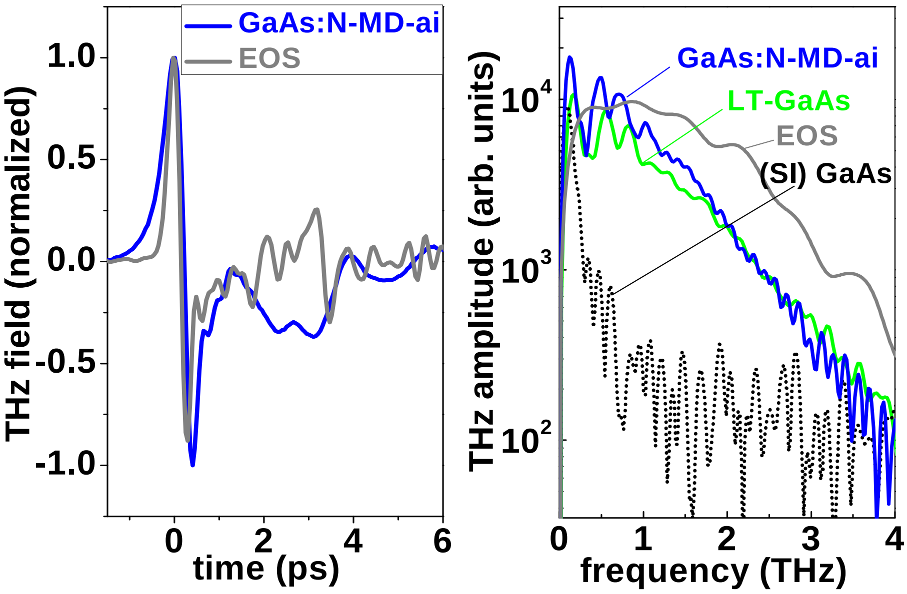

Figure 3.16: Left: Terahertz wave form detected with electro-optical sampling (grey) and with photoconductive detector based on GaAs:N-MD-ai substrate. Right: Calculated amplitude spectra for selected detectors.

Also for the GaAs:As samples, the signals indicate a reduced carrier lifetime with increasing dose. The much longer lifetime in SI GaAs, which is typically a few 100 ps [120], leads to a signal with very slow components and a high noise level.

In table 3.2, the peak-to-peak signal, noise, and SNR are summarized. The noise for the implanted samples systematically decreases with increasing dose. The best SNR is found for the LT-GaAs detector and for the GaAs:N-MD-ai detector. The good SNR of the GaAs:N-MD-ai detector indicates that the relative high dark current is not yet limiting its performance. The annealed GaAs:As detectors are

Sample name	Noise (rms)	Signal (p-p)	Sig/Noise
	(pA)	(pA)	
GaAs:N-LD	3.2	187	58
GaAs:N-MD-ai	0.2	384	1920
GaAs:N-MD	0.6	274	457
GaAs:N-HD	0.4	158	395
GaAs:As-MD	0.6	426	710
GaAs:As-HD	0.2	158	790
LT-GaAs	0.1	253	2530
SI GaAs	1.0	47	47

Table 3.2: Comparison of the peak to peak signal, noise current (RMS), and SNR for the detectors with different substrates.

second best choice with about three times lower SNRs. Fourier transforms of the signals from these optimum detectors are shown in figure 3.16. For comparison, the spectra of the SI GaAs detector and from EOS are shown. At low frequencies, spectral components for the GaAs:N-MD-ai detector are slightly stronger than for the LT-GaAs detector, while at frequencies above 1.5 THz, they are similar. The spectral range of the SI GaAs on the other hand is limited to about 0.3 THz. From the temporal shapes of the detected signals, carrier lifetimes can be deduced with an accuracy of about 20 %. By deconvoluting the signal detected with the GaAs:N-MD-ai detector with different values of τ and comparing the result with the form of $E(t)$ measured with EOS [2] (figure 3.16) under the same conditions, a value of 0.7 ps was obtained for the carrier lifetime. While performing a similar analysis for the other detectors, we find carrier lifetimes of 0.4 ps for the LT-GaAs, and times in the range from 1.2- 2 ps for the implanted and annealed samples. These values are consistent with literature values for comparably processed materials [117, 121, 122].

The dependence of the photocurrent signal on the power of the near-infrared gating beam was studied using a spot size of the gating beam of 300 μm. The maximum power of 117 mW corresponds to an excitation density of 5.7×10^{16} cm^{-3}. For the LT-GaAs detector, a linear increase was found for gating powers below 50 mW and a slightly sublinear dependence above (figure 3.17(a)).

---

[2] For the electro-optical-sampling we used two parabolic gold mirrors arranged to a telescope and an ITO coated mirror as described in section 3.3.2.

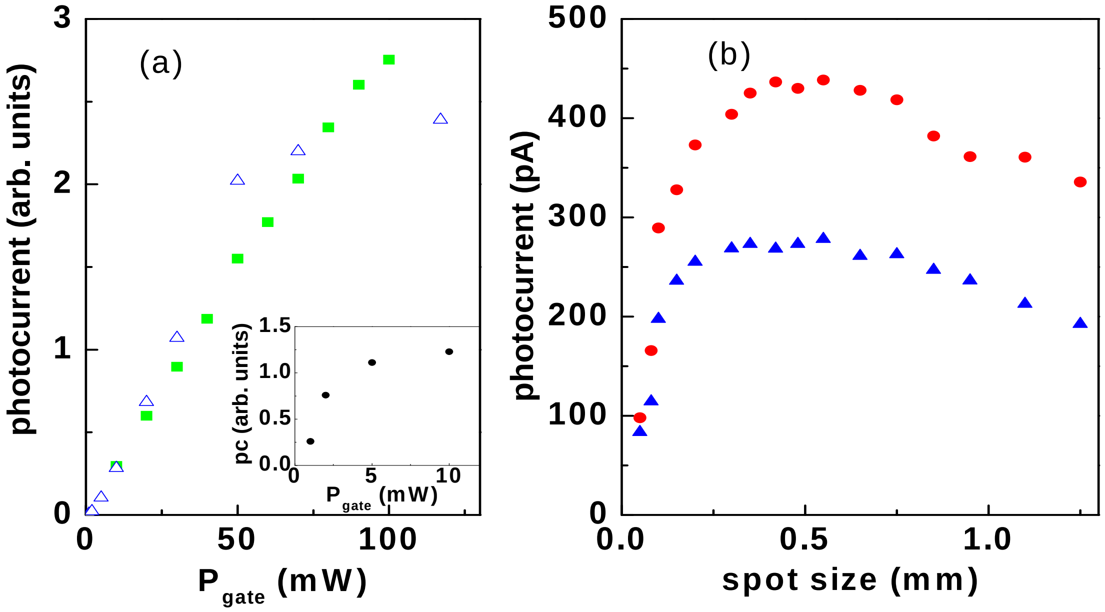

Figure 3.17: Left: Peak-to-peak photocurrent (pc) signal as a function of the gating power, for LT-GaAs (green squares), the GaAs:N-MD-ai detector (blue triangles), and the SI GaAs detector (circles in inset). Right: Peak-to-peak photocurrent signal as a function of the spot size of the gating laser, GaAs:As-MD (red circles), and GaAs:N-MD-ai detector (blue triangles).

A similar behavior was found for the other optimum detector, namely the GaAs:N-MD-ai detector. For the implanted and annealed detectors, a more pronounced sublinear dependence was observed, which also set in at lower powers (see open triangles in figure 3.17(a)). For the SI GaAs detector, strong saturation was already observed for gating powers above 2 mW (see inset of figure 3.17(a)). In the range of a few milliwatt, the detectors with longer carrier lifetimes (GaAs:N-LD and SI GaAs) provided stronger signals compared to the detectors with short carrier lifetimes. The strong saturation behavior for the detectors with long carrier lifetimes is the reason why the amplitude of their signal at 70 mW gating power (see figure 3.15) is significantly smaller compared to detectors with shorter lifetimes. We note that the best overall SNRs are found for the LT-GaAs detector and the GaAs:N-MD-ai detector for gating powers in the range of 50 - 70 mW. The saturation behavior can be attributed to screening effects in the detection antenna. The antenna capacitance was measured for different active areas and a value of 13 pF/mm^2 was obtained. For a THz field of 10 V/cm and a gating power of 2 mW, we estimate that 1.8×10^5 electrons reach the electrodes of a SI GaAs detector. Here, a mobility of $5000\,cm^2/V \cdot s$ and a carrier lifetime of 100 ps is assumed. However, the capacitance of the illuminated spot corresponds only to 4×10^4 electrons for the field of 10 V/cm; hence, a strong saturation of the signal due to screening is expected. This consideration is independent of the value for the THz field since both the number of electrons stored in the capacitance and the number of photoexcited electrons reaching the electrodes scale linearly with the driving electric field. For LT-GaAs and implanted materials with carrier lifetimes in the picosecond range and lower mobilities, the saturation is expected to play a role only at 3 to 4 orders of magnitudes at higher excitation densities.

The dependence of the detected signal on the spot size of the gating beam is illustrated in figure 3.17(b). The spot size was varied while the gating power was kept constant at 70 mW. Optimum detector signals are obtained for spot sizes in the range from 0.3 to 0.6 mm. The decrease of the signal for larger spot sizes is caused by the fact that parts of the gating beam irradiate the detector outside the active area of 1 mm × 1 mm. The decrease towards smaller spot sizes is caused by the sublinear dependence of the photocurrent on the excitation density. For the GaAs:N-MD detector, this decrease sets in at larger spot sizes, because the saturation effects set in at lower excitation densities compared to the GaAs:N-MD-ai detector.

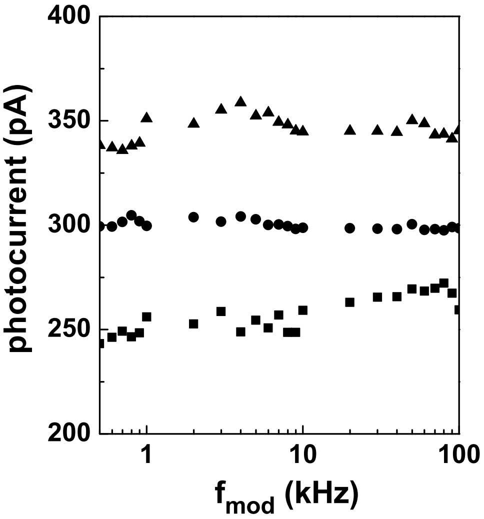

Figure 3.18: Peak-to-peak photocurrent signal for the LT-GaAs detector as a function of the modulation frequency. The spot size of the gating beam is 150 μm (triangles), 300 μm (circles), and 700 μm (squares).

A concern of the scalable, large-area concept can be the large capacitance of the structure that limits the modulation frequency. The dependence of the detected THz signal on the modulation frequency is shown in figure 3.18, for the LT-GaAs antenna in the range from 0.5 kHz to 100 kHz. In this range, the THz signal was independent of the modulation frequency. This was verified for different spot sizes of the gating beam. Since the LT-GaAs antenna is the sample with the smallest photocurrent, the largest value for the RC time constant is expected for this structure. The experiment shows that modulation in the kilohertz range is possible. This is essential to avoid the typical 1/f-laser noise which is dominant in the range of a few 100 Hz.

3.5 THz beams of radial and azimuthal polarization

Compared to THz waves of linear polarization and Gaussian beam profile, radially polarized beams have interesting fundamental properties such as smaller beam waists in the focus and strong longitudinal field components in the focus [123, 124]. Engineering of the THz field distribution is of great importance for THz waveguiding. Because of their small attenuation and low dispersion, metallic wires for plasmonic guiding of THz waves are in the focus of intense research [82, 83]. Such guided THz modes, so-called Sommerfeld modes, have a radial field distribution. For enhanced coupling J.A. Deibel and colleagues developed THz emitter for radially polarized beams and coupled them directly to the wire [83, 125]. Radial polarization of THz waves has also been realized via velocity mismatched optical rectification in a free-space propgation setup [126]. As shown in figure 3.2 (section 3.1) the concept of the interdigitated electrode structure can be transfered to various electrode geometries. Hereby the field pattern of the generated THz radiation is always orthogonal to the electrode structure. On the next pages beam profiles of radially, azimuthally, and for comparison linearly polarized beams are presented and discussed, parts of this were published in Opt. Express 17, pp. 1571-1576 (2009).

The setups for measuring the beam profiles of divergent THz beams behind the emitter and for refocussed beams are shown in the upper part of figure 3.19. The profile is measured by moving a translation stage on which the detector and a plane mirror are mounted perpendicular to the beam propagation axis (x direction in figure 3.19). The emitter antennas with their different electrode geometries were based on SI GaAs, while for detection devices fabricated on GaAs:N-MD (see previous section -table 3.1) substrates with electrodes arranged as parallel stripes were used (figure 3.1). Such an detector is sensitive to the linear polarized component perpendicular to the electrodes. The studied pattern is then like a cross section through the mode patterns in figure 3.2 c-f. In figure 3.19 (a) and (b) beam profiles for the three types of emitters are shown for the divergent beam and for the refocused beam. In all cases the detector is sensitive for linear polarization. For the emitters of linear and radial polarization the horizontal component of the field is detected, while for the emitter of azimuthal polarization the vertical component is detected. Plotted are the peak-to-peak values of the photocurrent of the THz traces. For an emitter with parallel electrode pattern the shape of the traces is essentially the same for all detector positions x. The amplitude is maximal for $x = 0$ which corresponds to the propagation axis. They can be well described by Gaussian functions. In case of the radially polarized beam the traces for each detector position x differ significantly (not shown). The THz traces show a change in sign as the detector is moved from negative to positive values of x. The electric field of the lowest order Bessel-Gauss beams for a cross-section at the height of the propagation axis has the form [127]

$$E(x) = E_0 J_1\left(\frac{x}{d_1}\right) exp^{\frac{-4ln2\cdot x^2}{d_2^2}}. \tag{3.1}$$

where E_0 is a constant value for the field, J_1 the Bessel function of the first kind of order one, d_1 a characteristic scale for the lateral extension of the Bessel function, d_2 the FWHM of the Gaussian function. The direction of E_0 is along the x-direction for the radial polarization and perpendicular to both the x-direction and the propagation direction in case of the azimuthal polarization. The measured beam profiles for the radially and azimuthally polarized beams can be described well by these lowest order Bessel-Gauss modes (figure 3.19(a) and 3.19(b)). Furthermore free-space propagation and refocusing does not distort the profiles of these THz beams. The deviation of the measured beam profiles from perfect inversion symmetry with respect to $x = 0$ is attributed to the imperfect symmetry of the near infrared excitation beam and imperfect alignment of the excitation beam on the antennas. Hence, a hybrid mode consisting of a Bessel-Gauss mode and small contribution of a Gaussian mode is excited.

For a more quantitative description of the propagation of the beams, the THz traces are Fourier transformed and beam profiles for the divergent beam are plotted

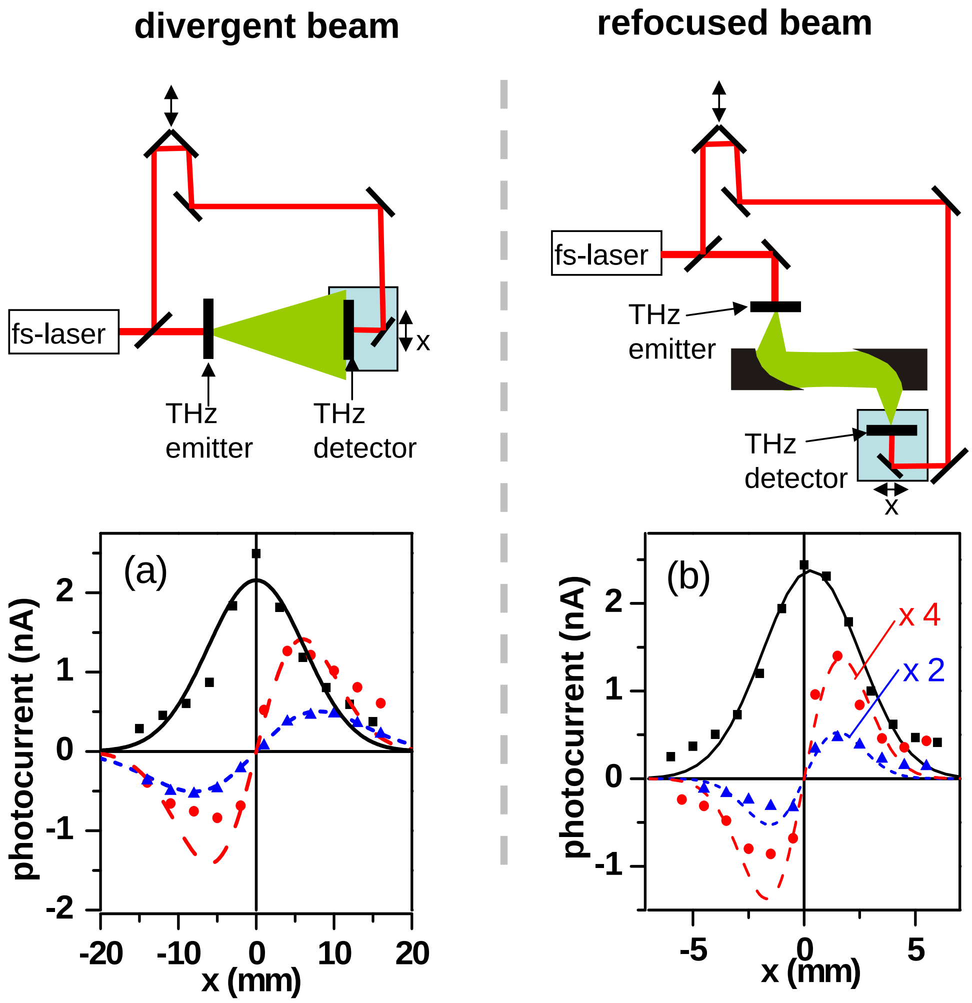

Figure 3.19: Upper part: Setups for measuring beam profiles of divergent and focused THz beams. Below: Related beam profiles of linear (black squares and solid lines), radial (red circles and dashed lines) and azimuthal (blue triangles and short dashed lines) polarization for (a) divergent and (b) refocused beams. For the radially and azimuthally polarized beams the lines represent fits based on the lowest order Bessel-Gauss function (equation 3.1). The fits for the linearly polarized beams rested on a Gaussian function. For clarity experimental and calculated data of the focused radially and azimuthally beams are scaled vertically by a factor of 4 and 2, respectively.

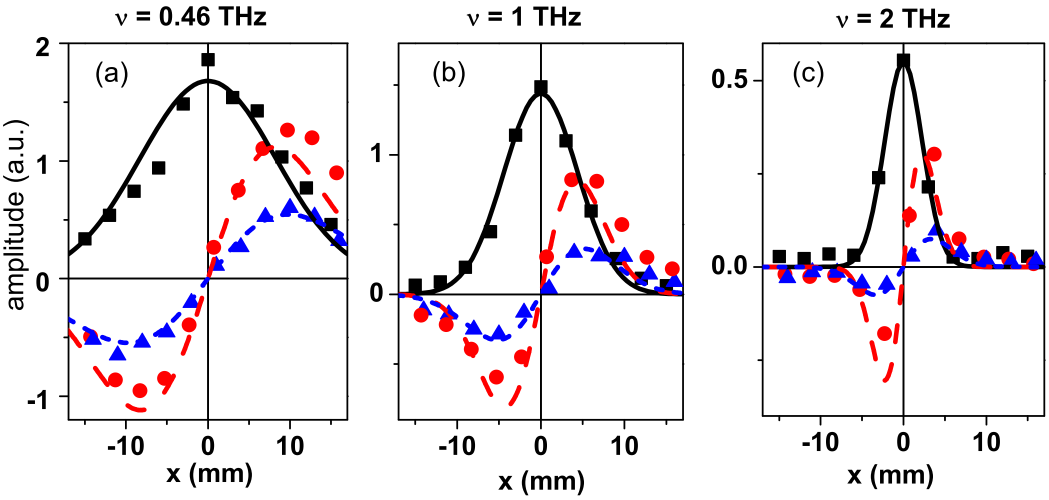

Figure 3.20: Measured (dotted) and calculated (lines) profiles for 0.5 THz (a), 1 THz (b) and 2 THz (c). Linear polarized correspond to black rectangles and lines, red circles and dashed lines to the radial polarization, blue triangles and short dashed lines to azimuthal polarization.

in figure 3.20 for three different frequencies. For all THz modes the lower frequency components are more divergent than the higher-frequency components. The data for the beam of linear polarization are fitted with Gaussian curves with FWHM of 19.6 mm, 10.4 mm and 5.4 mm for the frequencies 0.5 THz, 1 THz and 2 THz, respectively. The data for radially and azimuthally polarized radiation are fitted using Eq. 3.1. For the radially polarized beam all frequency components can be well described taking the same values for d_2 as for the fits of the linearly polarized beam and $d_1 = 1.25 \times d_2$ (dashed lines in figure 3.20). The curves for the azimuthally polarized beam are calculated for the same values of d_1 as for the radially polarized beam for all frequencies. However, the profiles of the azimuthally polarized beam are somewhat wider compared to the radially polarized beam. Good agreement is found for d_2 being 1.2 times larger than for the linearly and radially polarized beams for the frequencies 0.5 THz and 1 THz (short dashed lines in figure 3.20 a,b). For 2 THz a good fit is obtained with a 1.5 times larger value of d_2 (short dashed line in figure 3.20c). The larger divergence of the azimuthally polarized beams can be explained by the different bias field distribution. In contrast to the emitters for linearly and radially polarized radiation, the strength of the electric bias field is not constant for the emitter of azimuthally polarized radiation. Instead the strength of the bias field decreases proportionally to $1/x$. Hence, the THz generation is more efficient in the center of the emitter, resulting in a smaller value of the THz beam waist at the emitter. This in turn leads to more divergent beams and therefore larger values of d_2 for the detected profiles. For higher frequencies this effect is even more pronounced, since these frequency components are enhanced for higher bias fields [59].

Mode sensitive detection is studied in the setup for focused THz beams. The emitter is optimized for radially polarized radiation. Detectors optimized for radial and azimuthal polarization are employed. Detection with an antenna matched for the radially polarized mode resulted in seven times larger signals as compared to detection with an antenna matched for azimuthal polarization (figure 3.21). This serves as a proof-of-principle that the antennas are advantageous for detection of changes in the mode pattern. The mode selective detection is a generalization of polarization sensitive THz detection. Polarization sensitive THz detection has been demonstrated by special dipole antennas, which can selectively detect orthogonal components of linearly polarized radiation [128].

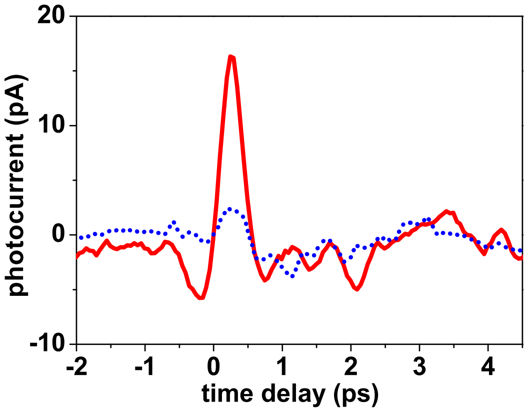

Figure 3.21: Traces from an emitter for radially polarized THz radiation measured with an detector of the same electrode pattern (red solid line), and with a detector matched for azimuthally polarized beams (blue dotted line).

3.6 Summary and Outlook

3.6.1 Emitter for excitation wavelengths above 1 μm

Overall, a GaInAsN based large area photoconductive THz source has been presented operating at excitation wavelengths up to 1.5 μm, while best performance is achieved for wavelengths below 1.35 μm. A high-resistivity substrate which is a key prerequisite for a large-area device can be realized by molecular-beam epitaxy grown GaInAsN on GaAs with an additional AlGaAs heterostructure. Based on the scalability of the device no saturation behavior over the available range of excitation powers was observed. The limited bandwidth of the emitted Terahertz radiation of 2 THz is attributed to the relatively large pulse duration of the OPO. Further optimization of the balance between high resistivity and high mobility of the substrate material should increase the performance in bandwidth and excitation wavelength towards the 1.55 μm range. In addition the presented device shows an interesting opportunity for fiber lasers operating around 1.1 μm as described in Reference [129].

3.6.2 Scalable photoconductive detector

In summary the detectors based on LT-GaAs and GaAs:N implanted with a dose in the $10^{13}\,\mathrm{cm}^{-2}$ range provide best signal to noise ratios even for unfocused THz radiation. Due to the large range of linearity in respect of the gating power and the convenient range of optimum spot sizes, these structures are easy to use and well suited for compact THz setups. The possibility to detect unfocused THz radiation with structures that also do not require precise alignment of the gating beam on a small antenna gap can be very interesting for the design of detector arrays for imaging purpose or for moving detectors. The GaAs:N-MD-(ai) samples showed that there is a further chance for improvements in responsivity by varying the annealing temperature.

3.6.3 Radially and azimuthally polarized THz radiation

It has been shown by the example of radially and azimuthally polarized beams that microstructured scalable THz antennas have a great potential to generate and detect any desired THz mode. The radially and azimuthally polarized beams can be well described as lowest order Bessel-Gauss beams. Free space propagation and focusing do not distort the beam profiles. In comparison to the divergence of linearly polarized THz beams, the divergence of radially polarized beams is similar, while the one for azimuthally polarized beams is slightly larger. With this knowledge, quasioptical systems can be easily adopted for those modes. In addition, mode sensitive detection has been demonstrated with detector antennas similarly patterned as the emitter devices. This serves as a proof-of-principle that the emitter-detector arrangement is well suited for studying changes of the mode structure. Again, those devices which are scalable in size open new possibilities to study interesting properties such as longitudinal fields in the focus of freely propagating beams of radial polarization as well as optimized coupling to guided THz modes.

4 Examples for Terahertz Time Domain Spectroscopy

In this chapter several possibilities for the application of Terahertz-Time-Domain Spectroscopy (THz-TDS) are shown. In the first section we will determine the THz refractive index of SI GaAs which is required for the treatment of the polaritonic phase matching in chapter 5. The other experiments deal with possible applications of THz-TDS in food inspection and process monitoring.

4.1 Determination of the dielectric function with THz TDS

The experimental realization is similar to the one described in the previous chapter 3 (figure 3.4 (a)). Again the fs Tsunami laser system was utilized for excitation and detection. The sample was simply placed between the two parabolic gold mirrors. For electro-optical sampling (EOS) a $160\,\mu$m $\langle 110\rangle$ thick ZnTe crystal was used. Figure 4.1 illustrates the measured THz traces, the black line represents the reference measurement without sample, while the red line indicates the THz trace transmitted through a $350\,\mu$m thick SI GaAs wafer. What can be seen clearly is the temporal delay and the attenuation of the THz cycle if transmitted through the GaAs wafer. Thus the field traces contain the complete temporal waveform, the spectra obtained by Fourier transformation include amplitude as well as phase information. In the lower part of figure 3.4 the spectra and the corresponding phase (inset) are shown. With this information we are able to calculate the transfer function and therefore the dielectric function (see section 2.3). In order to calculate the THz refractive index we used equation (2.35). The results are shown by black squares in figure 4.2. Between 0.25 and 2.25 THz the data are in good agreement

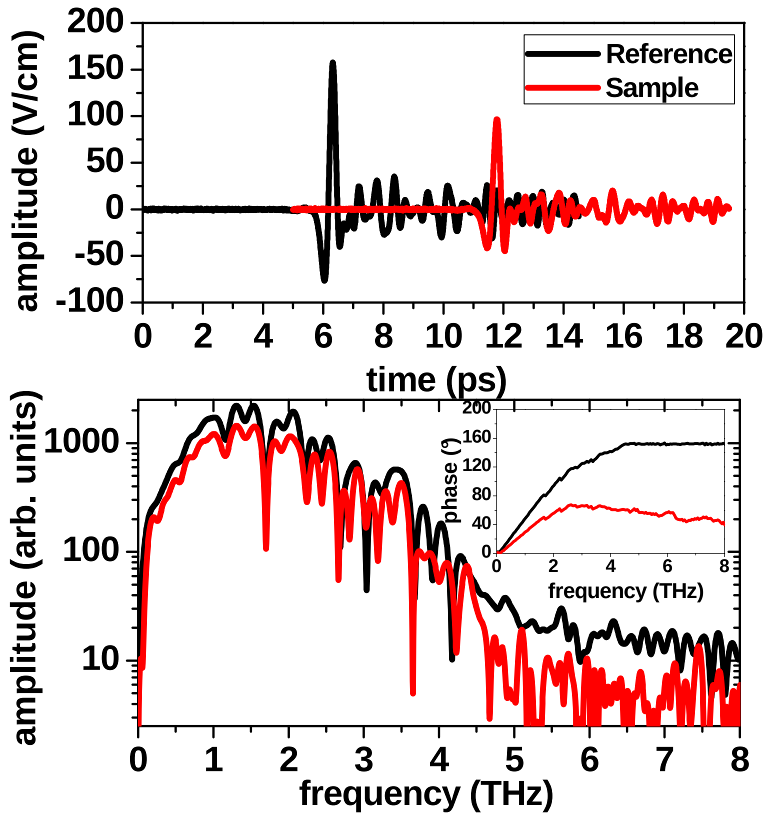

Figure 4.1: The graph above shows the measured time-domain-terahertz traces without sample (black reference) and with THz transmission through the $350\,\mu$m GaAs wafer (red). For generating the THz radiation a large area photoconductive device was applied excited with a 800 nm femtosecond Ti:Sa laser. Detection was by EOS with a $160\,\mu$m $\langle 110\rangle$ ZnTe crystal. The graph below illustrates the amplitude and phase (inset) of the spectra obtained by Fourier transformation of the time-domain data.

with a theoretical model based on a Lorentz oscillator with a resonance frequency of 8.1 THz (red solid line). For higher THz frequencies the assumptions made in the theoretical model are not valid (see appendix A.2). Additionally the dynamic range of the experimental data decreases rapidly (lower part in figure 4.1). Therefore the mismatch between theoretical (red solid line) and experimental (black squares) data is growing for higher THz frequencies. Nevertheless, the good agreement up to 2.2 THz allows a good estimation for the polaritonic phase matching points between THz and a near infrared (NIR) wave later in chapter 5.

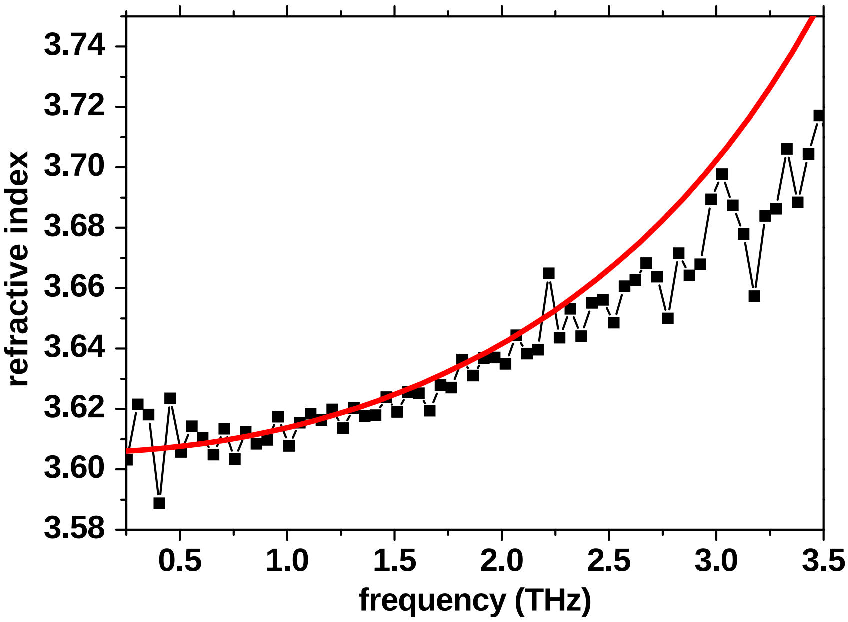

Figure 4.2: Index of refraction of SI GaAs calculated from time domain spectroscopy data from figure 4.1. The red solid line is the calculated refractive index assuming a Lorentz oscillator model (appendix A). The parameters for the calculation are ω_0=268.7 cm^{-1} (8.1 THz), ϵ_{stat}=12.8, ϵ_∞=10,8, γ=2.4 cm^{-1} [23, 57].

4.2 Examples of THz-TDS in process monitoring and food inspection

A useful feature of THz radiation is that many packaging materials like paper or plastic foil are transparent for THz beams. In figure 4.3 the modification of a THz pulse is shown when transmitted through several paper sheets. The sheets are normal office paper with a density of about 80 g/m^2. The peak of the THz field is delayed by 160 fs per sheet. Indicated by a pulse broadening the long wavelength component becomes the dominant part in the transmitted THz pulse with increasing sheet number. From the spectra in figure 4.3 it can be seen that for frequencies up to 0.2 THz the sheets are practically transparent, while for frequencies between 0.2 and 1 THz the transmission of 10 sheets is about 10% and for higher frequencies the signal drops off quickly. The dynamic range of the measrement is about six orders of magnitude. The measurement shows the potential of THz TDS systems. This can be utilized for tomography in the THz [130].

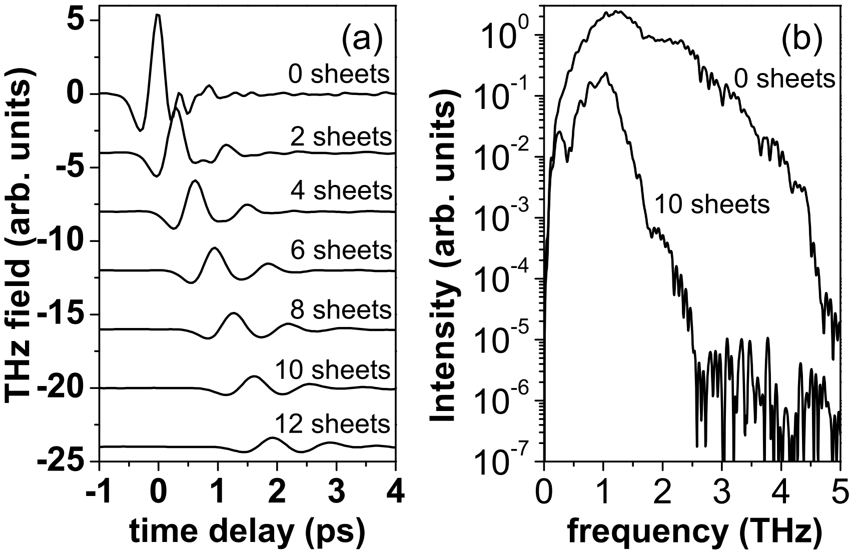

Figure 4.3: THz transmission through several sheets of paper (a) in the time domain and in the frequency domain (b).

In another experiment we investigated the THz transmission through a chocolate praline. The experimental results are illustrated in figure 4.4. For comparison the spectrum of the reference without chocolate is shown (dashed line in figure 4.4). While an empty dried chocolate praline shows some transmission for frequencies below 1.2 THz, a schnapps filled chocolate praline shows, due to the strong water and alcohol absorptions, no transmitted signal. The oscillations of 0.16 THz in the spectra of the empty praline originate from multiple reflections at the chocolate interfaces.

Apart from being used in quality control during food inspection or for packaging applications, THz systems also offer interesting oppertunities for the polymer processing industry. Although many plastic materials in the THz range are transparent, they show some characteristics in the spectra [131]. For instance in-line monitoring of additive content in polymers or the non-destructive testing of polymeric components are further fields of application. It may also be possible to use THz radiation for monitoring process gases which are circulating inside of plastic pipes [132]. In figure 4.5 the transmission of THz radiation through different kinds of plastic cards are shown. In the time domain the different attenuations and delays of the THz main pulse for the individual plastic cards can be clearly seen. The ID

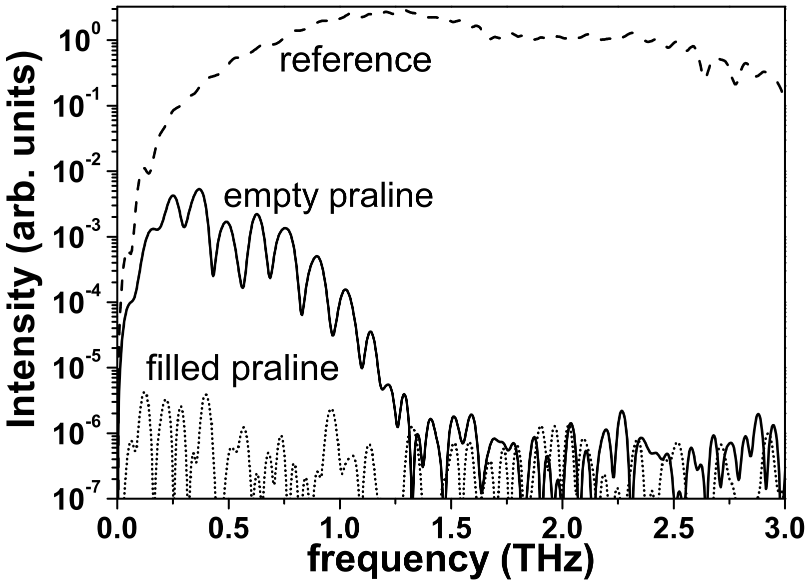

Figure 4.4: THz spectrum of THz transmission through a filled schnapps praline (dotted line) and an empty praline (solid line). The reference is the dashed line.

card and the foam show a similar transparency of about 50% up to 1.2 THz in the spectra on the right side in figure 4.5. Furthermore, for higher THz frequencies the absorption of the foam and the ID increases in the same way. In the time domain data the thickness variation of the ID and foam reveals a difference of about 1 ps in the delay times. The FZD card has comparable geometrical thickness to the ID card but has a much higher optical thickness [1]. This can be seen in the larger temporal delay of the THz main pulse. In the absorption spectra the FZD card shows a transmission of about 20% up to 1.1 THz and a rapid decline for higher frequencies. The transmission of the DVD box is nearly zero.

4.3 Summary and Outlook

The last pages demonstrate the capability and applicability of THz-TDS by studying the transmission of paper sheets, chocolate pralines and different plastics. Furthermore the THz refractive index of a SI GaAs wafer was determined.
THz TDS with high bandwidth needs short laser pulses and broadband emitters

---

[1] Optical thickness is the product of geometrical thickness and refractive index.

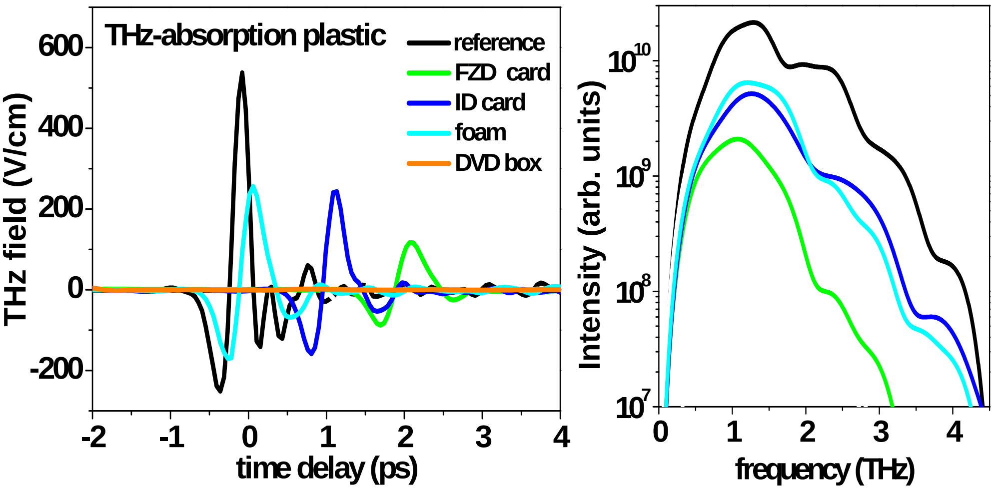

Figure 4.5: THz transmission through different plastic cards in the time domain and in the frequency domain.

and detectors. Additionally the steps for the temporal delay must be small in order to meet the Nyquist criteria. The Nyquist criteria ensures that the sampling rate is sufficient to allow perfect reconstruction of the signal from the measurement [133]. To avoid aliasing or frequency cutoff, the rule of thumb in digital signal processing is that the sampling rate $\nu_{sampling}$ has to be at least twice the frequency bandwidth of the signal $\Delta\nu$. This means for a THz signal with $\Delta\nu = 5\,\text{THz}$ the step length has to be below 100 fs. For a high spectral resolution the THz wave has to be recorded over a long time domain. All this leads to long measurement times. For imaging applications, where the sample is moved in a horizontal and vertical direction and a THz trace has to be measured at each position, the time effort increases dramatically, if the measurement is realized, as presented, with mechanical delay lines. An alternative option would be a continuously movement of the delay line by using a retro-reflector mounted on a shaker (fast scan technique). Because of the mechanical inertia this technique is limited to shaker frequencies of a few 10 Hz and a maximum delay of about 20 ps. A further development of the idea of continuous moving mechanics are a rotating mirror pair and a fixed mirror in the form of a cycloid [134–137]. With these delay lines, long time intervals can be measured at high sampling rates. The drawback is the challenging alignment of the mirrors in the laser beam path. Time delay without any mechanical movement can be realized by using chirped pulses for detection [138,139]. Hereby the time domain information is converted into a spectral information of the near infrared sampling beam. Likewise, asynchronous optical sampling (ASOPS) comes without having a mechanical component. Thereby a second fs laser is used for detection. This laser has a repetition frequency slightly offset from the excitation laser typically are 1 GHz repetition rates with an offset of 10 kHz. With this technique spectral resolution of 1 GHz and sampling rates of 10 kHz combined with an excellent signal to noise ratio have been realized [140–142].

5 THz emission by frequency mixing

In this chapter we investigate THz emission generated by optical rectification of near-infrared pulses (NIR), in the wavelength range between 1.1 μm and 1.6 μm. For this purpose several laser systems are utilized. These includes an OPO, a fibre laser and two different amplifier systems, OPA and TOPAS, with pulse energies from 1.5 nJ, 3 nJ, 0.7 μJ and 30 μJ, respectively (more details on the laser systems can be found in appendix A.1). The first object of investigation is an organic salt crystal named DAST. The second part deals with GaAs as nonlinear medium. Hereby a specific topic will be polaritonic phase matching between the NIR and THz beams in a GaAs slab.

5.1 Optical rectification with DAST

The organic ionic salt crystal DAST (4-N,N-dimethylamino-4'-N'-methyl stilbazolium tosylate) is known for its large nonlinear and EO coefficient. It was first shown to be an efficient THz emitter via optical rectification in 1992 [143]. In table 5.1 the second-order nonlinear coefficient and its Pockels coefficient are provided for the wavelength of 800 nm and 1535 nm. At a wavelength of 800 nm the second-order nonlinear coefficient of DAST is almost twelve times larger than the coefficient of GaSe, a widely employed material for broadband THz rectification [144]. The drawback of a DAST crystal as emitter or detector is an absorption dip around 1.1 THz in the THz spectrum. This is attributed to a transverse optical-phonon originating from an anion vibration in the DAST lattice. However, in the last years DAST has been established as a benchmark for THz devices working with fibre lasers around 1.55 μm. To find the optimum thickness of the DAST crystal two things have to be considered. While a thicker crystal provides a larger THz generation volume, a thinner crystal has a reduced THz absorption. Furthermore a thicker crystal only makes sense as long as phase matching is fulfilled and the coherence length for

wavelength (nm)	r_{111} (pm/V)	χ_{111} (pm/V)
800 nm	80	1200
1535 nm	50	500

Table 5.1: electro-optic coefficients r_{ijk} and nonlinear susceptibilities,χ_{kij} of DAST [145]

a certain pair of THz frequency and NIR wavelength is greater than or equal to the crystal length. Additionally, increasing thickness causes the production of high quality crystals to be more challenging. The final compromise for 1.5 μm excitation was a 0.58 mm thick DAST crystal [146], which was purchased from Rainbow Photonics. For excitation two different femtosecond laser systems were applied, first a fibre laser (FFS.SYS from Toptica) with 100 fs pulse length, 1550 nm wavelength and 78 MHz repetition rate. The second laser system was an optical parametric amplifier (OPA 9840) supplied by Coherent. Inc, which was driven by a regenerative Ti:Sa amplifier (RegA 9040). The measured pulse length of the OPA was between 100 fs and 120 fs (FWHM) with a repetition rate of 250 kHz and a wavelength tuning range from 1100 nm to 1600 nm. For imaging the generated THz radiation we used two parabolic gold mirrors arranged to a telescope. In both cases detection was achieved with electro-optical-sampling (EOS) in a $\langle 110 \rangle$ oriented ZnTe crystal. For that we needed a sampling beam around 800 nm. In the case of the fibre laser we applied second harmonic generation to produce a 775 nm beam. For the measurements with the OPA, a small part of the 800 nm beam from the RegA was split off before entering the OPA. In order to overlap the NIR sampling beam with the THz beam we utilized indium tin oxide (ITO) which is transparent at NIR wavelengths but reflective in the THz range.

In figure 5.1 a measurement of the THz field trace is illustrated using the fibre laser at a pulse energy of 1 nJ. The peak to peak value of the THz field was calculated to be 3 V/cm by using equation 2.26. The THz spot at the ZnTe crystal was determined to be 500 μm by moving the THz beam relatively to the NIR beam. This is achieved by tilting the ITO mirror [60]. Using the THz pulse duration of approximately 3 ps, as shown in figure 5.1, the THz peak power was calculated to be 2 μW. Figure 5.1 b illustrates the THz spectra obtained by fourier transformation of the THz traces detected with ZnTe crystals of two different thicknesses (100 μm and 1 mm, red and black graphs respectively). The spectrum ranges from 0 to 3.5 THz.

For higher THz frequencies the coherence length in ZnTe becomes shorter. While for 2 THz the coherence length is about 2 mm, it is below 300 μm for 2.5 THz [25]. If the coherence length is shorter than the crystal thickness, the spectrum drops much faster for increasing frequencies. Because of this phase mismatch the thinner detector crystal in figure 5.1 (b) has a better response at higher THz frequencies.

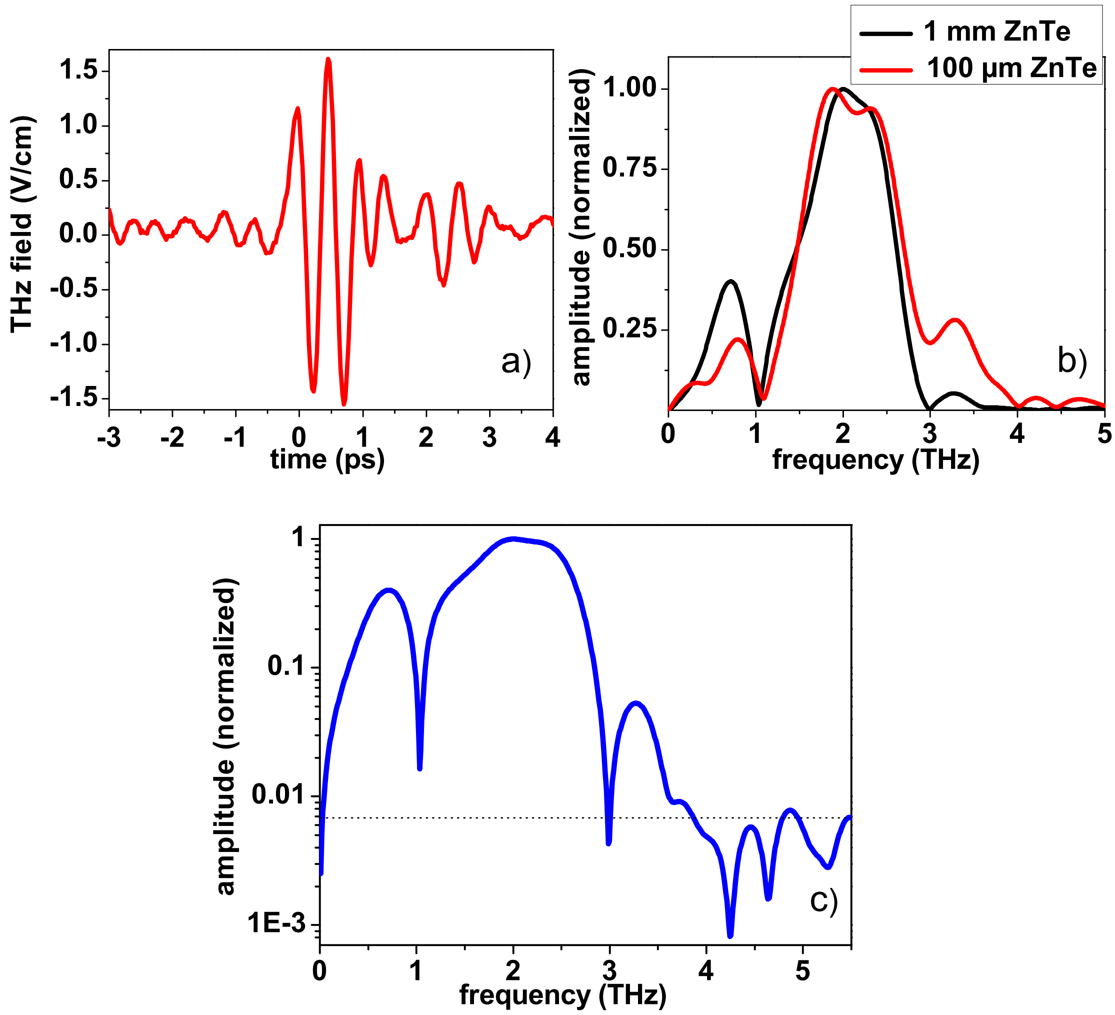

Figure 5.1: THz pulse generated by optical rectification of 1.55 μm pulses in a 0.58 mm thick DAST crystal and detected by electro-optic sampling in a ZnTe crystal using a frequency doubled probe beam (λ=775 nm). Field trace in the time domain (a), fourier transformed amplitude for two detector crystals (b). The red curve correspond to a 100 μm thin ZnTe detector crystal and the black to a thicker (1 mm) ZnTe detector crystal. Logarithmic plot of the fourier transformed amplitude detected with the 1 mm ZnTe crystal (c).

In figure 5.1 (c) the spectral amplitude is plotted on a logarithmic scale in order to highlight the characteristic absorptions in a DAST crystal. The first absorption dip is at 1.1 THz and originates from the already mentioned optical-phonon resonance. The second absorption dip is located around 3 THz. This absorption has already been observed [145, 147] and is also attributed to an optical-phonon resonance. The signal-to-noise ratio can be estimated to around $\approx 10^2$ (figure 5.1 (c) dotted line).

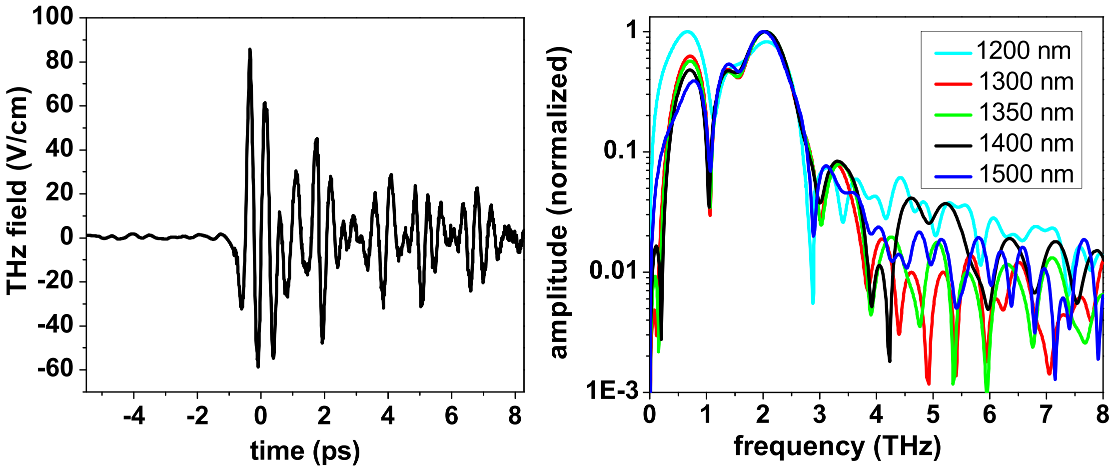

Figure 5.2: THz trace generated by optical rectification in a 0.58 mm thick DAST crystal excited at 1400 nm and detected by electro-optic sampling in a 200 μm thick ZnTe crystal using a probe beam with λ=800 nm. The excitation was with a pulse energy of 200 nJ by using the OPA. Right: Normalized THz spectra generated at different pump wavelengths.

Figure 5.2 illustrates the THz pulses generated with the OPA at a pulse energy of 200 nJ. In order to detect the THz pulses a 200 μm thick ZnTe crystal was applied. For wavelengths in the range from 1300 nm to 1500 nm no significant change of the THz field amplitude was observed, while for excitation wavelength below 1300 nm a slight decrease was seen. On the right side in figure 5.2 the spectra of the emitted THz radiation for several pump wavelengths are shown. The spectra are normalized to their maximum value. Below 1 THz the amplitude drops with increasing wavelength while between the two absorption frequencies 1.1 and 3 THz the spectral amplitude is similar for all NIR wavelengths. Schneider et al. [145] have investigated the phase matching in DAST crystals for several excitation wavelengths. They found a similar pattern, observing that the spectra were nearly independent of the excitation wavelengths between the absorption dips, while for frequencies

parameters	fibre laser (1.55 μm)	OPA (1.4 μm)
NIR pulse energy (nJ)	1	200
repetition rate	78 MHz	250 kHz
NIR pulse duration	100 fs	100 fs
peak to peak THz field strength (V/cm)	3	140
THz pulse energy (J)	$7.5 \cdot 10^{-18}$	$1.6 \cdot 10^{-14}$
average THz power (nW)	0.6	4
THz peak power (μW)	2	$5 \cdot 10^3$
photon conversion efficiency at 2 THz	$1.2 \cdot 10^{-6}$	$1.3 \cdot 10^{-6}$

Table 5.2: THz pulse properties and photon conversion efficiency for optical rectification in a $0.58\,mm$ thick DAST crystal with two different laser systems.

below 1 THz and above 3 THz the relative THz amplitude increased for decreasing excitation wavelength. Since the cutoff frequency in our measurement is around 3.5 THz we can not investigate the spectral region above 3 THz. This upper frequency limit is mainly given by the properties of the detector material. In table 5.2 various quantities of the generated THz pulses are summarized for the fibre and OPA laser system. For the higher pulse energies with the OPA we obtained higher THz fields, however, the THz field does not rise linear with the NIR power. Schneider et al. [145] attributed this to a decrease of pump pulse energy through two-photon absorption in DAST. They estimated the two-photon absorption coefficient in DAST to 0.7 cm/GW. Later we will determine this coefficient in GaAs and we will find out that this effect is much higher in GaAs then in a DAST crystal.

5.2 Optical rectification with GaAs

5.2.1 Bulk GaAs

The simplest way to generate THz radiation by optical rectification in GaAs is using a bulk $\langle 110 \rangle$ oriented GaAs crystal. Because the susceptibility depends on the crystal orientation relative to the polarization of the NIR beam (see section 2.1.4), the contribution of the THz radiation depends on the azimuthal angle between the space coordinate [1] and the crystallographic coordinate at normal optical incidence. Figure 5.3 shows this typical azimuthal dependency for rectification in a 625 μm thick $\langle 110 \rangle$ oriented GaAs wafer. These results correlate very well with data published by A. Rice et al. [148] where the polarization of the THz beam was parallel to the dipole detector axis used for detection. Although we detect by EOS and not by a photoconductive device as in ref. [148], the results prove that the applied detection geometry with a $\langle 110 \rangle$ ZnTe crystal is sensitive to the x-component of the THz field as it was shown in section 2.1.6 figure 2.6. This is the case if the polarizations of the NIR sampling beam and THz beam are parallel [149]. It has

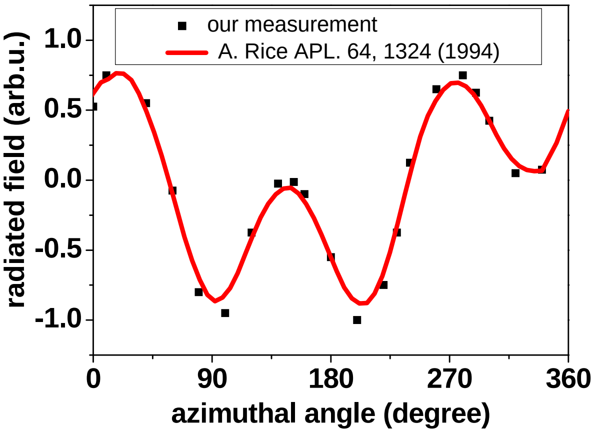

Figure 5.3: THz signal from $\langle 110 \rangle$ oriented bulk GaAs with a thickness of 625 μm in dependences from the azimuthal angle between space coordinate and crystallographic coordinate at normal optical incidence. The red line serves as references from a theoretical model in ref. [148]. The squares are from experimental data obtained by excitation with the TOPAS.

---

[1] Fixed coordinate system where the z-axis is the propagation direction of the NIR beam, the y-axis is perpendicular to the optical desk and the x-axis is the direction of the polarization of the NIR beam. The azimuthal angle describes the rotation of the crystal around z.

been shown that the whole setup has a better efficiency for parallel than for orthogonal polarizations between NIR and THz. Furthermore the curve in figure 5.3 is a verification that in our setup the second-order optical rectification in GaAs is the major nonlinear process that generates THz radiation.
Since the energy gap in GaAs corresponds to a photon wavelength of 873 nm at room temperature, GaAs is transparent above this wavelength. However, for higher optical pulse intensities nonlinear effects besides the second-order optical rectification play a more important role, such as two photon excitation. These effects reduce the transparency by increasing the absorption [150]. In figure 5.4 the absorption in $\langle 110 \rangle$ oriented semi-insulating GaAs at normal incidence is plotted for several pulse energies achieved with the OPA or TOPAS for different wavelengths. While the variation in the transparency for the different wavelengths is nearly constant, a strong dependency on the excitation energy is observed.

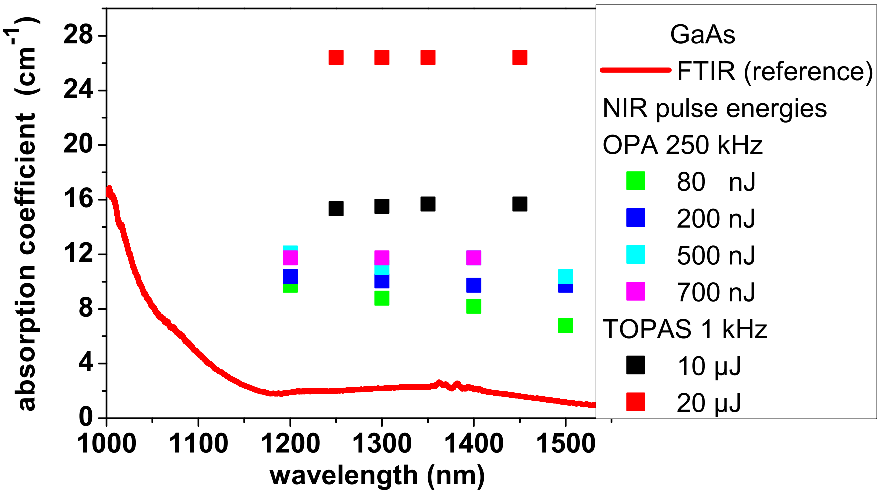

Figure 5.4: Transmission of the unfocused NIR excitation beam through $\langle 110 \rangle$ oriented 625 μm thick GaAs wafer at normal incidence for several pulse energies reached with the OPA or the TOPAS. The red graph represents a FTIR reference measurement.

For example when using a pulse energy of 20 μJ, less than thirty percent of the radiation is transmitted through the 625 μm thick GaAs wafer[2]. The two photon absorption coefficient β is given by the relation $I = I_0/(1+\beta d I_0)$. For excitation by

---

[2] Considering the reflection losses at the air-GaAs surface and the absorption relation $I/I_0 = e^{-\alpha \cdot d}$ gives about 25% transmission with α=26 cm^{-1} and $d = 625\,\mu$m.

the 20 μJ from the TOPAS the spot size of the unfocused spot was 5 mm, the two photon absorption coefficient β is then about 30 cm/GW. The values of β found in the literature span over the range of 20-30 cm/GW for wavelength above the band gap [151–153]. As expected, damage to the crystal surface occurred for higher pulse energies, which was caused by the NIR beam being focused at a spot size of $\approx 70\,\mu$m. As illustrated in figure 5.3 and 5.4, these preliminary experiments determined the optimal azimuthal angle to be 225 ° and the maximum level of excitation energy whereby crystal damaging is avoided. In figure 5.5 the obtained THz traces are plotted for excitation with the OPA and the TOPAS. The electric field amplitude is about 2 V/cm and 15 V/cm with excitation by the OPA and the TOPAS, respectively. The spectral range in both configurations is about 2.5 THz. Again sampling was conducted by applying a part of the 800 nm beam, which is driving the OPA or the TOPAS, to a 200 μm thick ZnTe crystal. By using the TOPAS for

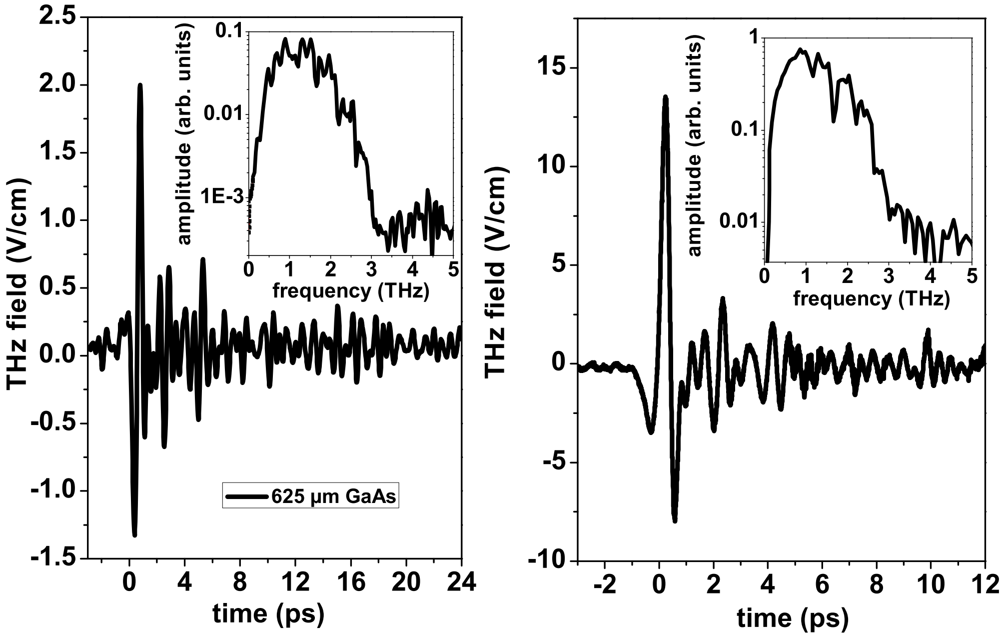

Figure 5.5: THz trace generated by optical rectification in a 625 μm thick GaAs crystal at 1350 nm and detected by electro-optic sampling in a 200 μm thick ZnTe crystal using a probe beam with $\lambda = 800$ nm. Left: Excitation was with a pulse energy of $0.6\,\mu J$ by using the OPA. Right: Excitation with a pulse energy of 20 μJ by using the TOPAS. Insets: related THz spectra obtained by fourier transformation of the time domain data.

excitation the NIR pulse energy was about thirty times higher than when using the

OPA, however the THz field amplitude rose only sevenfold. This results in a THz photon conversion efficiency of $\approx 3 \cdot 10^{-8}$ and $\approx 10^{-9}$ for the OPA and the TOPAS, respectively for a THz photon energy corresponding to 1 THz. Figure 5.6 illustrates another experiment where the emitted THz field was recorded as a function of the excitation pulse energy. This made it apparent that for pulse energies below 300 nJ the THz amplitude scales linear with the excitation pulse energies, while for pulse energies above this threshold the dependency is sub-linear and finally for pulse energies above 20 μJ it stays almost constant. This is somehow unexpected because in a straightforward consideration the THz field amplitude would scale linearly with the NIR intensity[3]. To some extent, the decreased efficiency for higher pulse energies can be attributed to two photon absorption as a competitive nonlinear effect as it was plotted in figure 5.4. Basically the high NIR pulse energies generated by the TOPAS lead to a surface damage on the GaAs emitter which in turn could finally evaporate the device surface. In order to circumvent the two photon absorption in GaAs the excitation wavelengths could be shifted above 1800 nm.

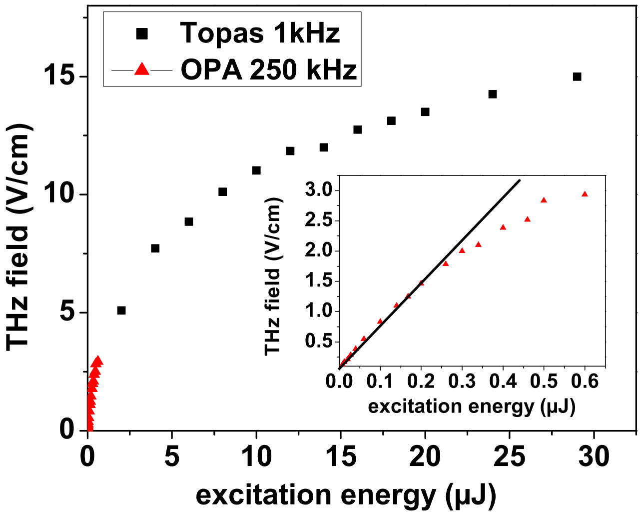

Figure 5.6: Emitted THz field for several excitation energies obtained by rectification in a $\langle 110 \rangle$ oriented GaAs crystal with the OPA (red triangles) or the TOPAS (black squares) at a wavelength of 1300 nm. Inset: Enlargement for the range which was accessible with the OPA. The solid line is a linear fit based on the data between 0 and 0.3 μJ.

In the theoretical chapter 2.1.5 it was suggested that the THz spectra might be

---

[3] The NIR excitation spot size was always kept constant to 70 μm FWHM

tuned by adjusting the excitation wavelength during polaritonic phase matching. However, this has not been observed so far. Up to now THz generation was studied in a GaAs crystal with a thickness of 625 μm. In equation (2.16) it was shown that for thicker crystals phase matching becomes more important than in thinner ones. It is therefore necessary to investigate at what thickness polaritonic phase matching becomes significant during optical rectification in GaAs. Another emerging question is the possible THz tuning range by phase matched optical rectification in GaAs. The next section will deal with these questions in more detail.

5.2.2 Phasematching in GaAs

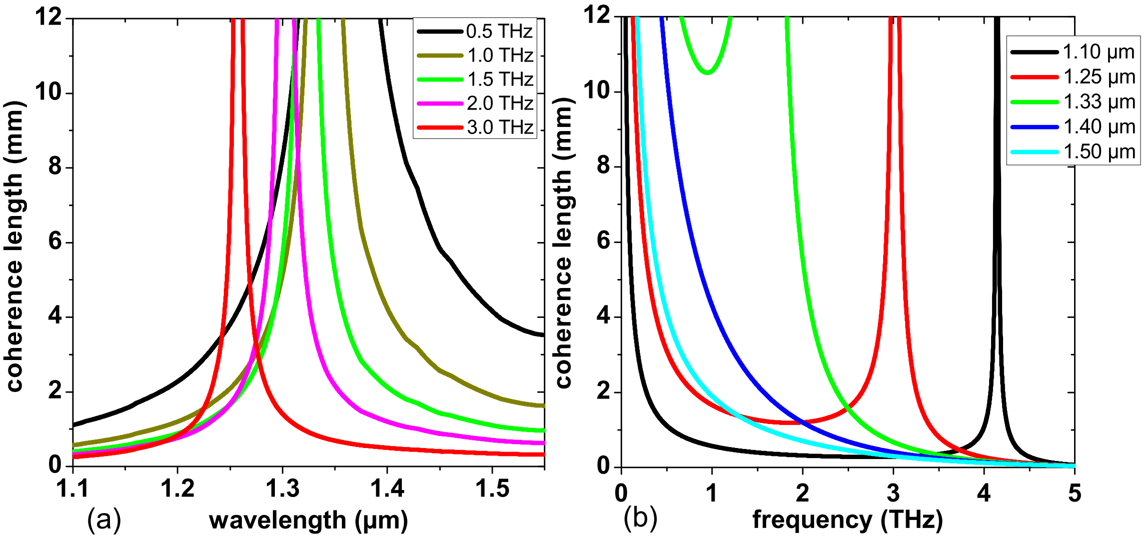

Figure 5.7: Coherence length in GaAs as a function of optical wavelength (a) and THz frequency (b) calculated using equation 5.1.

The relation (2.20) in section 2.1.5 implies that phase matching is accomplished when the phase of the THz wave travels at the velocity of the optical pulse envelope (i.e. the optical group velocity v_g). The appropriate coherence length determines the phase mismatch between the NIR wave and the THz wave over the whole distance. In other words, it provides a value for the walk-off length between the two fields. For difference frequency mixing and electro-optic sampling l_c is now

$$l_c = \frac{\pi c}{\omega_{THz} \left| n_{opt} - \lambda_{opt} \frac{dn_{opt}}{d\lambda} |_{\lambda_{opt}} - n_{THz} \right|}. \tag{5.1}$$

Using the refractive index data from the Sellmeyer Equation $n_{opt}^2 = A + B/(\lambda_{opt}^2 - C^2) - D\lambda_{opt}^2$ (with $A = 10.90600, B = 0.97501\,\mu m^2, C^2 = 0.27969\,\mu m^2, D = 0,00247\,\mu m^{-2}$ [154]), we find that at 1350 nm the effective optical refractive index[4] $N_{eff} = n_{opt} - \lambda_{opt}(dn_{opt}/d\lambda)$ equals 3.61 . Comparing this result with the measurements of the THz refractive index in chapter 4 (figure 4.2) it is apparent that at around 1.35 μm an acceptable matching between the NIR refractive index and the THz refractive index can be achieved. The reason for this matching is the reststrahlen region in GaAs as already discussed in 2.1.5. Using equation (5.1) and the refractive indices in the NIR and THz range we can calculate the coherence lengths as a function of the NIR excitation (figure 5.7(a)). Because of the pole in equation (5.1) the coherence length becomes infinite for a certain pair of NIR wavelength and THz frequency. This is the region where the phase matching is perfect. This region shifts to higher THz frequencies if the NIR wavelength is tuned to a shorter wavelength for instance: 3 THz matches to 1250 nm while 4.2 THz matches to 1100 nm (figure 5.7(b)). In figure (5.7(a)) we also observe a strong broadening for lower frequencies of the coherence length l_c. For instance for a 2 THz frequency the region where the coherence length is larger than 2 mm ranges from 1280 nm to 1375 nm while for a 1 THz frequency the phase matched NIR wavelength ranges from 1260 nm to 1450 nm. Even for a 0.5 THz frequency the phase matching for crystals up to a thickness of 1 mm is perfect over the whole laser tuning range of 1.1 to 1.6 μm. This offers one explanation to the questions raised at the end of section 5.2.1 concerning the “threshold thickness” of the GaAs at which polaritonic phase matching becomes important. It is therefore apparent that for a crystal thicknesses less than 2 mm no significant tuning of the THz output is possible by adjusting the NIR excitation wavelength. On the other hand the crystal thickness cannot become infinite because the dispersive broadening of the NIR excitation pulse reduces the efficiency of a second order nonlinear process. Bakunov et al. [155] showed that for a laser with 1.5 μm wavelength and a pulse duration of $150 - 200\,fs$ the optimum

---

[4] N_{eff} see chapter 2 section 2.1.5

thickness of a GaAs slab should be around 1 cm. Adopting these insights to our laser system with pulse durations around 100 fs the optimal slab length should be in the range of 5 to 10 mm. The next section presents such a GaAs slab for phase matched optical rectification.

5.2.3 GaAs slab

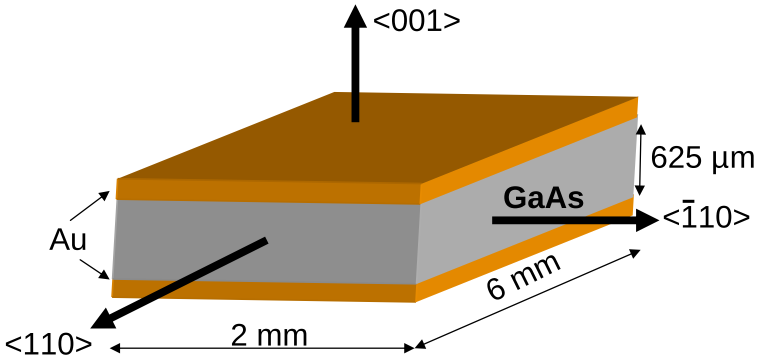

Figure 5.8: Sketch of the cleaved GaAs slab.

The slab employed in this experiment is made from a 625 μm thick $\langle 100 \rangle$ oriented, semi-insulating GaAs wafer. It is cleaved starting from the flat of the wafer with a length of 6 mm and a width of 2 mm. Since the surface of the flat in such a wafer has an orientation of $\langle 110 \rangle$, the second-order susceptibility tensor has a nonzero component, and therefore the facets can be used as coupling surfaces for the NIR excitation beam (see fig. 5.8). To prevent losses from radiation leaking at the upper and lower end of the slab, which would not be imaged to the detector, both sides were metallized using chromium-gold layers. Furthermore, this metallization enhances the overlap between the NIR beam and the generated THz beam. Before we start with the experimental investigations of THz emission from a GaAs slab we will first have to look at the propagation of a THz wave in such a structure. In figure 5.9 a simulation illustrates how the transverse electric (TE) mode with a frequency of 1 THz propagates in such a structure. The calculations were done by applying a finite element method using the commercial program Comsol. The program solves the wave equation including the corresponding boundary conditions at the interfaces.

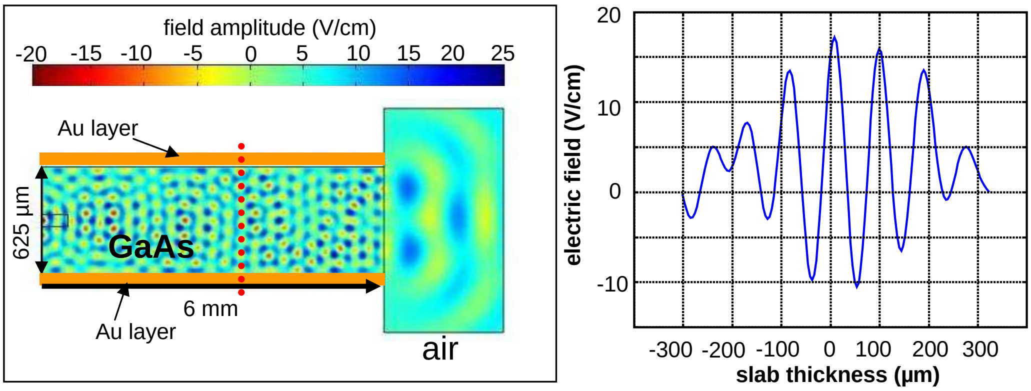

Figure 5.9: Field distribution of an in-plane TE wave with a frequency of 1 THz in the GaAs slab and its transition to air. Plotted is the electric field component perpendicular to the viewing plane (left). The right side illustrates a line plot of the field cross section at the red dotted line in the simulation at the left. The simulation was performed with finite element method using the commercial simulation program Comsol.

In the simulation the NIR beam has a spot size of 70 μm (FWHM) and penetrates the slab on the left side in figure 5.9. From there it generates the THz radiation which is then propagating through the slab before reaching the GaAs-air interface. On its way through the slab the THz wave is multiply reflected at the gold layers as well as reflected internally at the GaAs-air interface. These multiple reflections and the superposition of the resulting modes induce the structure of the illustrated field distribution. Because of the dimensions with respect to the wavelength, the slab acts like a multimode waveguide. The reason for the simulations was to get an idea about the THz guiding and about the THz outcoupling. The simulation showed that less than fifty percent of the THz field is coupled out to the air, the rest is trapped in the slab. This could be enhanced by using a substrate lens or a sort of an anti-reflection layer. The line plot of the field cross section on the right side in figure 5.9 clarifies the multimode characteristics of the slab. Furthermore it was found that at low frequency the slab is limited by a cutoff frequency, where the dispersion relation of the slab becomes imaginary and propagation is not possible. This cutoff frequency was around 300 GHz in the numerical calculation. On the high-frequency side it was found that for frequencies higher than 4 THz the superposition of the several modes in our numerical model is highly problematic, resulting in a sharply reduced outcoupling efficiency.

During the measurements with the 625 μm thick bulk GaAs wafer in the previous

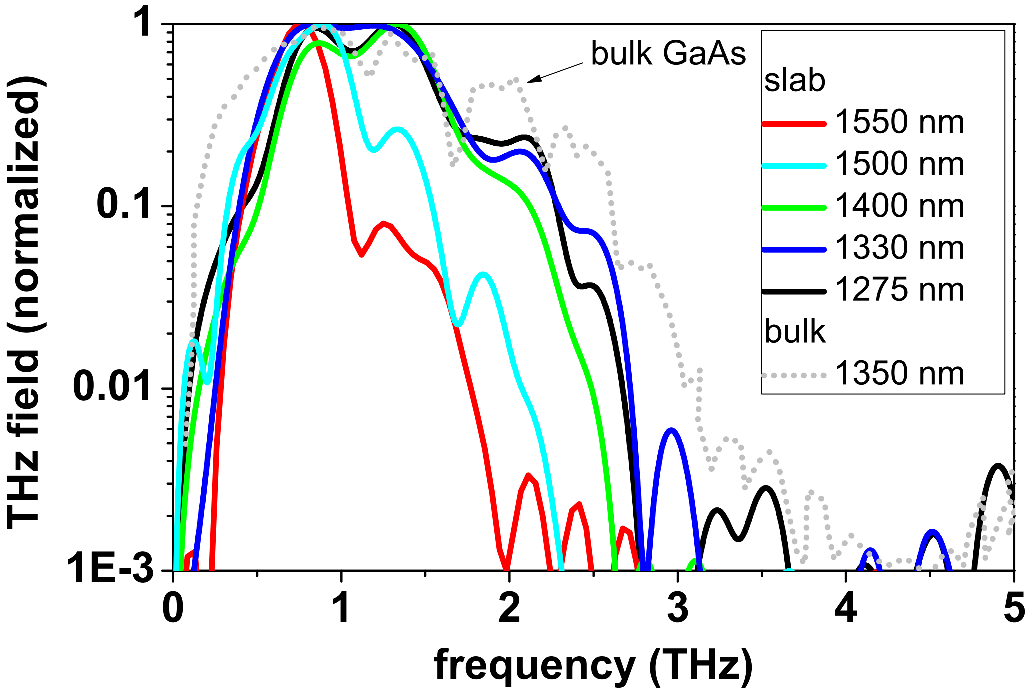

Figure 5.10: THz spectra of a slab-emitter for few exemplary excitation wavelengths, the driving laser system was the OPA with a pulse energy of 0.2 μJ. For comparison the spectrum of the bulk emitter is plotted (dotted light gray). The largest field amplitude was for 1.4 μm excitation (see figure 5.11).

section no significant changes in the emitted THz spectra were observed by tuning the excitation wavelength. In figure 5.10 the THz spectra from the GaAs slab were plotted for several exemplary excitation wavelengths. Within the slab there was some evidence of changes in bandwidth of the emitted THz radiation. As predicted by the phase matching model in figure 5.7 the shorter the excitation wavelength the higher the frequency components in the emitted spectra. From the simulations with the Comsol program, a low frequency limit for the propagation of a THz wave was predicted at a cutoff frequency of around 300 GHz. In fact, during the testing phase a cutoff was observed for frequency components below 0.4 THz. This is the reason why the spectra in figure 5.10 vary only on the higher frequency side with modified excitation wavelength. In order to understand the underlying physical mechanism for this cutoff in the low frequency limit we will have to look at the dispersion relation for TE waves in the slab. The wave equation is given to be

$$\frac{\partial^2 E}{\partial x^2} = \left(\frac{n^2\omega^2}{c_0^2} - k^2\right) E. \tag{5.2}$$

The solution for this type of differential equation is

$$E(x) = E_0 \cdot sin\frac{m\pi x}{d}, \tag{5.3}$$

where d is the slab thickness and m the solution for the m^{th} TE mode. The dispersion relation is calculated by inserting (5.3) into (5.2), which gives the dispersion relation for the wavenumber k

$$k = \sqrt{\frac{n^2\omega^2}{c_0^2} - \frac{m^2\pi^2}{d^2}}. \tag{5.4}$$

For example for our slab with a thickness d of 625 μm and m=1 the cutoff is roughly 100 GHz. Compared to the numerical calculation and the observational findings throughout the experiment this result is considerably lower. The reason for this is that in the analytical model the size of the source has been ignored. For a laser spot size of 70 μm the source is much smaller than the wavelength corresponding to frequencies of around several 100 GHz, therefore the first order modes of these frequencies can not propagate efficiently in the waveguide and the real cutoff is at higher THz frequencies than 100 GHz.

However, also on the high-frequency side in the emitted THz spectra we would expect a stronger shift to higher THz frequencies for shorter excitation wavelengths. For instance for an excitation wavelength of around 1250 nm the phase matched THz frequency is 3 THz as predicted in section 5.2.2, while the spectrum drops rapidly already above 2.5 THz in figure 5.10. There are two main reasons for this decrease of the high-frequency components. The first reason is the dependence of the coherence length on the excitation wavelength in figure 5.7. There the pole for higher THz frequencies is much sharper then for lower ones. Now we have to consider the bandwidth of the NIR laser pulse, which is typically around 100 nm for the OPA and even higher for the TOPAS (see laser spectra in appendix A.1). Convoluting now the coherence length from figure 5.7 with the NIR spectra of the laser leads to a much better overlap for the lower THz frequencies. In other words, excitation by a

spectrally broad laser pulse always fulfills the phase matching criteria for frequency components between 0.5 to 1 THz. At this stage those frequency components are the dominating part of the emitted spectra. Only for a larger crystal length or a sharper excitation spectra should it be possible to tune the higher THz frequencies by adjusting the excitation wavelength.
The second reason for this drop on the high-frequency side is a geometrical one. This is because higher THz frequencies have the drawback of a stronger multimode characteristic of the waveguide. Resulting in an enhanced superposition in the slab between the several modes coming from the multiple reflections at the interfaces in the slab. Due to random imperfections these modes are getting out of phase and smeares out the signal. Both limitations on the high as well as on the low frequency side result in a preference for frequencies between 0.5 to 2.5 THz. In addition to the spectral maximum of the emitted radiation attention needs to be paid to the field amplitude in the time domain and the bandwidth of the emitted radiation. In principle the THz field amplitude should become enhanced if the phase matching condition between the NIR excitation beam and the generated THz beam is fulfilled. On the left side in figure 5.11 the THz field is plotted in dependence of the excitation wavelength. Squares represent the experimental data, while the

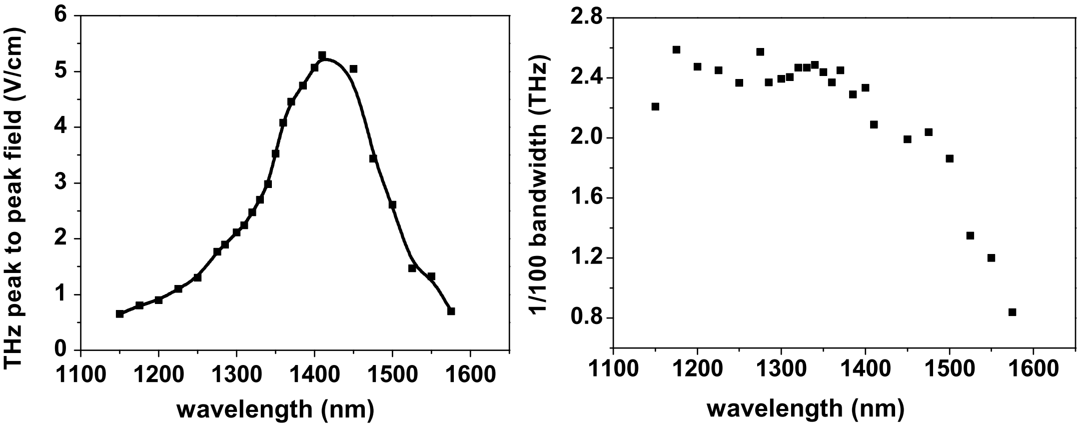

Figure 5.11: THz emission from GaAs-slab in dependence of excitation wavelength. The left figure illustrates the peak to peak value of the THz field in the time domain while on the right side the relative bandwidth of the emitted spectra is plotted. Excitation was again by the OPA laser system with a constant pulse energy of 0.2 μJ.

solid line serves as a visual guide. Again, excitation was by the OPA laser system at a constant pulse energy of 0.2 μJ. The maximum THz field emission (peak to peak) was for an excitation wavelength of around 1.4 μm. This maximum highlights that a NIR laser pulse with a bandwidth of 100 nm and a central wavelength of 1400 nm matches to most of the THz frequencies in figure 5.7. The dependence of the 20 dB bandwidth on the excitation wavelength is illustrated on the right side in figure 5.11. It is shown that the bandwidth remains constant up to 1400 nm and then decreases to less then half of the maximum value within an increase of the excitation wavelength of about 150 nm. The reason for this narrowing in the emitted spectra is that, on the high-frequency side, phase matched THz frequencies decrease with increasing wavelengths (figure 5.10). On the low frequency side the aforementioned frequency cutoff in the slab prevents a "red" shift of the spectra. This underpins that the phase mismatch in the slab between THz signal and NIR beam grows for excitation wavelengths above 1400 nm.

5.3 Discussion and Summary

In this chapter we investigated the properties of pulsed THz sources based on optical rectification with NIR pulses between 1.1 and 1.6 μm. For this purpose three different laser-systems were utilized. Firstly a high repetition fs fibre laser with a fixed emission wavelength of 1.55 μm and with pulse energies in the nJ-range was selected. The second laser system was an optical parametric amplifier with a tuneable emission wavelength of between 1.1 and 1.6 μm and with pulse energies of around 200 nJ. TOPAS, another optical parametric amplifier also with a tuneable wavelength of 1.1 to 1.6 μm but with a much higher pulse energy range of around 10 μJ, completed the selection of laser systems. The first crystal was the organic salt crystal DAST. The DAST crystal showed the highest THz field amplitude of 140 V/cm (peak to peak) by excitation with the OPA at 200 nJ with a bandwidth of 3.5 THz. The photon conversion efficiency was about 10^{-6} with a THz photon energy corresponding to 2 THz. The drawback of the DAST emitter are its absorption dips in the emitted spectra at 1.1 and 3 THz due to phonon resonances. The second investigated nonlinear material for optical rectification was the GaAs. GaAs is deemed to be an efficient emitter because of its high nonlinearities and especially due to its dielectric function allowing polaritonic phase matching between the THz and NIR beam.

It was found that the best phase matching point in GaAs between THz and NIR was for an excitation wavelength of 1400 nm.

GaAs	OPA with 0.6μJ pulse energy	TOPAS with 20μJ pulse energy
THz field (V/cm)	3	20
20 dB bandwidth (THz)	2.4	2.4
NIR absorption (cm^{-1})	10	26
THz peak power (μW)	14	70
THz photon conversion efficiency at 1 THz	$3 \cdot 10^{-8}$	10^{-9}

Table 5.3: Main properties of THz radiation generated in GaAs with a 250 kHz pulse repetition rate laser system (OPA) and a 1 kHz pulse repetition rate laser system (TOPAS). The excitation wavelength was 1350 nm.

However, when comparing the performance of the DAST crystal and the GaAs at telecommunication wavelengths, the DAST crystal generated a much higher magnitude of THz fields than the GaAs at comparable crystal thicknesses (see table 5.3 and 5.2). Even at higher excitation energies GaAs did not come close to the emission performance of the DAST emitter. This was due to an increased absorption at higher NIR pulse energies in the GaAs crystal leading to a saturated THz emission and a lower efficiency (table 5.3). The bandwidth of the emitted radiation in both mediums was comparable. The predicted opportunity of tuning the emitted THz spectra in a GaAs slab was observed, but it was not as strong as expected. The reasons for that are the limitations in a simplified picture of the THz guiding in a thicker crystal on the low frequency side as well as on the high-frequency side. The limitations on the low frequency side are mainly the discussed frequency cutoff in the slab for frequencies under 300 GHz. On the high-frequency side the phase matching between a broadband NIR pulse and the phase matched THz frequencies becomes more difficult. This is because the sharper divergence in the coherence length for higher THz frequencies favors an overlap of a 100 nm broad NIR pulse for frequencies between 0.5 up to 1.5 THz. These frequencies are always phase matched and dominate the emitted spectra. Furthermore it was found that the superposition of different modes in the slab is much stronger at higher THz frequencies, resulting in stronger group-velocity dispersion in the waveguide.

Nevertheless the efficiency in converting NIR photons to THz photons remains at a low level of 10^{-9} to 10^{-8}. A further enhancement for the THz emission with a GaAs slab could be obtained by increasing the thickness of the crystal to about 1 cm. The tunability within a GaAs slab could be optimized by using NIR excitation pulses with narrower spectral width. In the investigations it has been shown that finding waveguide geometries which are suitable for broadband THz pulses still remains a challenging task. In one of the theoretical works by A. Marandi et al. [156], he suggests another type of a DFG based THz source by integrating appropriate optical and THz waveguides. In their approach the THz wave is guided in a metallic slit waveguide and the optical mode is guided in an dielectric slab which is integrated in the metallic slit waveguide. Such kind of waveguides could be subject to further investigations on this topic.

A Appendix

A.1 Laser systems

In this work several laser systems were utilized. Table A.1 gives an overview of the main properties of these lasers. In figure A.1 some examples of spectra are shown.

Laser-system	Manufacturer	f_{rep}	λ (nm)	E_{pulse}	τ_{FWHM}(fs)
oscillator (Ti:Sa)	Femtolaser	78 MHz	800	6 nJ	12
oscillator (Ti:Sa)	Spectra Physics	78 MHz	750-840	10 nJ	70
oscillator (fibre)	TOPTICA	78 MHz	1550	3 nJ	100
amplifier	Femtolaser	1 kHz	800	0.8 mJ	30
amplifier	COHERENT	250 kHz	800	6 μJ	40
OPO	APE Berlin	78 MHz	1100-1600	1.5 nJ	200
OPA	COHERENT	250 kHz	1100-1600	0.7 μJ	100
TOPAS	LIGHTCON	1 kHz	1100-1500	30 μJ	50

Table A.1: Main properties of the used pulsed laser systems.

The main differences between the laser systems are their specific pulse energies and operating wavelength range. The Ti:Sa systems, with a center wavelength of around 800 nm, are employed for direct photoconductive excitation of THz radiation in SI GaAs. In order to discuss the fundamentals of all laser systems, we will have a detailed look at the kilohertz Femtolaser amplifier system, which is seeded by the 78 MHz oscillator named 'Scientific sPro'. The resulting amplified beam is then applied for driving the Traveling-wave Optical Parametric Amplifier of Superfluorescence (TOPAS) from Lightcon.

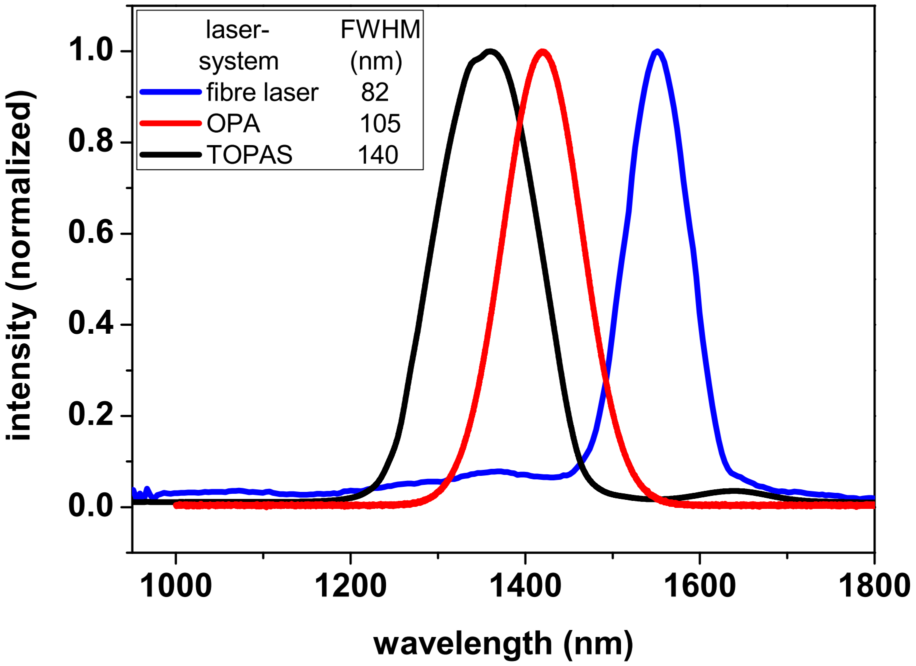

Figure A.1: Typical laser spectra for the fibre laser, the OPA and the TOPAS with corresponding bandwidths.

A.1.1 fs-Titanium-Sapphire-Oscillator

Because of the extremely broad gain spectrum, from 650 up to 1000 nm, and its high third-order nonlinear coefficient, Titanium doped sapphire ($Ti^{3+}Al_2O_3$) has become the most important laser medium for femtosecond laser technology. The operation principle of an ultrashort femtosecond oscillator is based on two main principles. These are the Kerr lens mode locking and the compensation of the group velocity dispersion. This can be realized for instance by dielectric negatively chirped mirrors. For pumping the Ti:Sa crystal a diode-pumped frequency doubled solid state laser is utilized (5 W, Nd:YVO$_4$ Verdi V5 from Coherent). This pump laser has an emission wavelength of 532 nm, which lies ideally within the absorption band of the Ti:Sa ranging from 400 up to 600 nm [157].

For a femtosecond pulse it is necessary that a broad spectrum of Fourier components overlaps with a fixed phase relation to each other in the laser cavity (mode locking). In a Ti:Sa crystal this can be realized by the already mentioned Kerr lensing. Thereby the effective refractive index n_{eff} becomes intensity dependent because of the high $\chi^{(3)}$-polarization in a Ti:Sa crystal, $n_{eff} = n + \alpha I$. This means that a transverse intensity profile induces a transverse refractive index profile like a focusing lens. This results in a stronger focusing of short pulses with higher intensities than in cw mode with low intensity. If the cavity of the laser has a design (e.g. a soft aperture [1]) which favors the more strongly focused modes, then the losses of the cw-modes are so high because of a mismatch of the cavity. The laser cavity is then more stable for pulsed operation than for cw operation. A small disturbance is then sufficient to start the mode locking operation. This can be achieved for instance by a small vibration or movement of one of the cavity mirrors.

Because of the group velocity dispersion different Fourier components have different round trip times in the cavity. This would lead to a broadening of the pulse and a disappearance of the Kerr effect. To prevent this most of the installed mirrors introduce a negative dispersion in order to compensate this positive chirp accumulated inside the laser cavity by air and the Ti:Sa crystal. The oscillator delivers an output power of 480 mW at 78 MHz, corresponding to a pulse energy of 6 nJ. The spectrum is centered at 800 nm with a FWHM of 110 nm and a pulse duration of 12 fs (FWHM).

A.1.2 kHz Amplifier System

For driving the TOPAS efficiently much higher pulse energies are needed, than an oscillator system with a high repetition rate can provide. This can be realized for instance with the commercial system FEMTOPOWER COMPACT PRO from Femtolasers GmbH, Vienna, Austria (figure A.2). The repetition rate of this system is 1 kHz. The description here gives just an overview of the main parts and the physical basics in such a laser system, a detailed description can also be found in Ref. [158]. This system is a multipass amplifier based on the chirped pulse amplification method. Initially pulses from a Titanium-Sapphire-Oscillator (Scientific sPro, Femtolasers) are stretched in time by adding a linear chirp in a stretcher, lengthening the pulses from about 12 fs to more then 10 ps. This is necessary to prevent peak intensities during the amplification process which are beyond the

---

[1] A soft aperture is no real aperture but it is realized by focusing the pump beam into the Ti:Sa crystal. The aperture diameter then corresponds to the spot size of the pump beam.

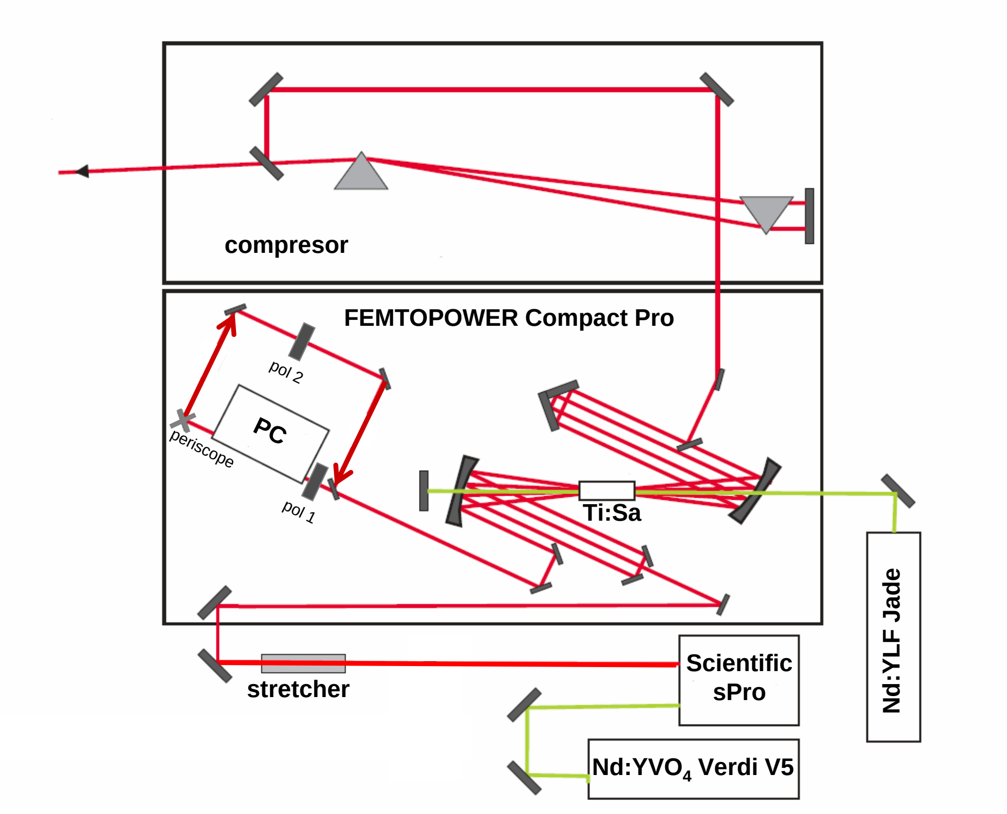

Figure A.2: Simplified layout of the Femtolaser amplifier system. It consists of the 78 MHz oscillator system (Scientific sPro) with the pulse stretcher, the amplifier stages with pockels cell (PC), Ti:Sa crystal and Jade pumplaser. On top of the picture the last module is illustrated, the prism compressor.

damage threshold of optics and crystals utilized in the amplifier. Additionally, this stretching increases the efficiency by enhancing the power transfer from the pump laser to the amplified pulses. In the next step the stretched pulses are coupled into the multipass amplifier which is pumped by an Q-switched diode-pumped frequency doubled solid state laser (Nd:YLF Jade Thales) with a repetition rate of 1 kHz and a pulse energy of 20 mJ. After four passes through the amplifying Ti:Sa crystal, one pulse out of the pulse train of preamplified pulses is picked out by a Pockels cell, which is in turn triggered by the 1 kHz repetition rate of the pump laser. This pulse passes an additional five amplification rounds through the crystal and is then outcoupled to the prism compressor. In the compressor the pulse is finally compressed to approximately 30 fs. The so created NIR pulses have a spectral width of about

40 nm and a maximum pulse energy of 0.8 mJ with a 1 kHz repetition rate.

A.1.3 Traveling-Wave Optical Parametric Amplifier of Superfluorescence (TOPAS)

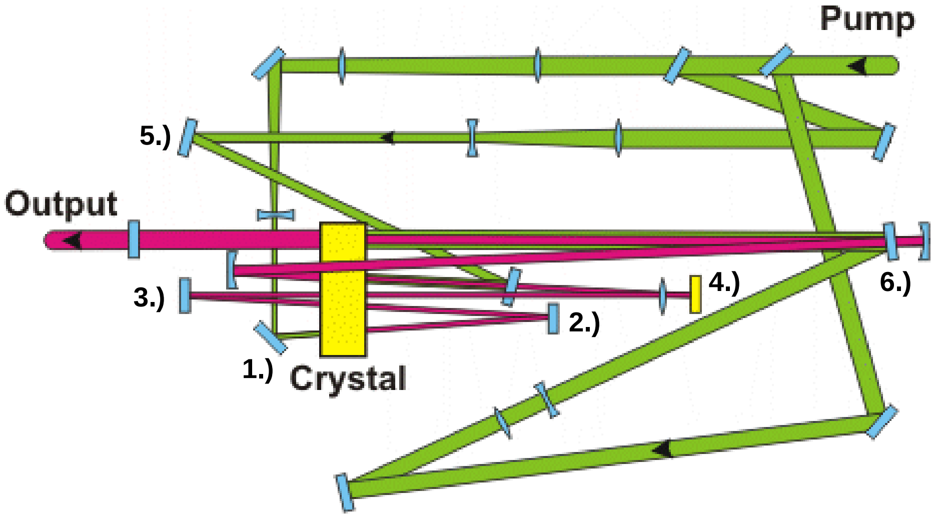

Figure A.3: Schematic layout of the TOPAS (Light Conversion Limited). The green line represents the 800 nm pump beam provided by the kHz amplifier system. The pump is divided into 3 parts by two beam splitters (BS) at the beginning of the TOPAS. The first BS reflects about 90 % which is later employed for the final power amplification. The light reflected by the second BS is applied for preamplification. The transmitted light is used for generating the superfluorescence (SFL) in the BBO-crystal (purple line). Because of the wavelength dependent diffraction at the grating (4), the SFL is spatially widened. The wavelength part of the SFL that is amplified, can now be tuned by overlapping it with the reflected parts from the two BS. This is realized by proper focusing the amplification beams and tuning the SFL by tilting (4).

The TOPAS system is basically an Optical Parametric Amplifier (OPA). The particular characteristic that distinguishes the TOPAS system from the OPA is that at first a small part of the pump generates parametric superfluorescence (1. and 2 in figure A.3) which is then amplified by the three stages of preamplifying (3,4,5), and one stage of power amplifying (6) by using a geometrical arrangement with a single nonlinear crystal (BBO). Because of an additional diffraction the superfluorescence light is spatially widened. Since the pump light in the amplifying stages is focused to a smaller beam, only a narrower spectrum of the diffracted beam will be amplified. This is how the wavelength and the bandwidth of Signal and Idler beam are tuned. The power amplifier uses <90% of the pump energy and is adjusted for high conversion efficiency along with good beam quality and short duration of the converted pulses. To achieve energy stability of generated pulses all the amplification stages are driven into saturation. At each stage the pump intensities are adjusted for the particular pump pulse width and power used.

A.1.4 Optical Parametric Oscillator

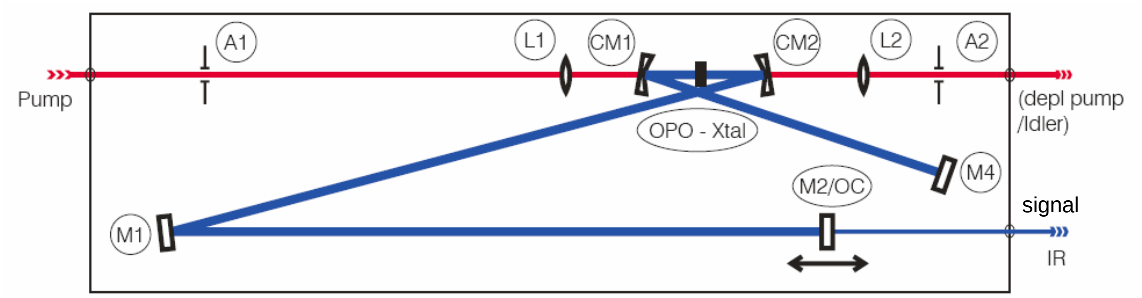

Figure A.4: OPO layout from Ref. [159]. The red line represents the pump beam provided by a femtosecond Ti:Sa system operating at a wavelength of 820 nm. The blue line indicates the light generated in the cavity by the parametrical process. The output-coupler for the signal beam is the end mirror M2. By moving this mirror and thereby changing the cavity length the wavelength of the signal beam can be tuned.

The OPO cavity is a 5-mirror standing-wave system resonant to the Signal. In figure A.4 the cavity configuration is shown. The nonlinear crystal is a periodically poled potassium titanyl phosphate (KTP). The main difference to the OPA and TOPAS is that the OPO has a real cavity and the wavelengths of signal and idler are tuned by the cavity length. The OPO is pumped by a mode locked Ti:Sa (Tsunami Spectra Physics) with a wavelength of 820 nm. Typical pulse duration of the signal pulse is 250 fs at a 78 MHz repetition rate and a tuneability of 1.1 to 1.5 μm.

A.2 Lorentz Oscillator Model

In chapter 3 figure 4.2 we use the Lorentz Oscillator model for a theoretical description of the THz refractive index in GaAs. Here a short description of the main idea of this model is given. A detailed derivation can be found either in [160] or [161]. In the reststrahlen region the radiation field interacts with the fundamental lattice vibrations. For a simple description of this interaction between a photon and a phonon we can use a harmonic oscillator model, where the coupling between the lattice atoms is described by analogy to Hooke's law. Furthermore, considering damping and the optical electrical field as driving force leads us to the well known differential equation

$$\ddot{x} + \gamma\dot{x} + \omega_0^2 x = \frac{e}{m} E_0 e^{-i(\omega t - kz)}, \tag{A.1}$$

where the physical meaning of $x(t)$ is the electron displacement. Using the common ansatz x(t)=x$_0 e^{-i(\omega t - kz)}$ [160] and solving for the dielectric function gives

$$\epsilon(\omega) = \epsilon_\infty + \frac{\omega_0^2(\epsilon_{static} - \epsilon_\infty)}{\omega_0^2 - \omega^2 - i\omega\gamma}. \tag{A.2}$$

The Lyddane-Sachs-Teller relation connects the dielectric constants ϵ_{static} for $\omega \to 0$ and ϵ_∞ for $\omega \to \infty$ with the long-wavelength phonon frequencies ($\frac{\epsilon_{static}}{\epsilon_\infty} = (\frac{\omega_{LO}}{\omega_{TO}})^2$). By using $\omega_0 \to \omega_{TO}$ in A.2, the dielectric function and the refractive index in the THz regime are then given by

$$n_{THz}^2 = \epsilon(\omega) = \epsilon_\infty + \frac{\omega_{TO}^2(\epsilon_{static} - \epsilon_\infty)}{\omega_{TO}^2 - \omega^2 - i\omega\gamma}, \tag{A.3}$$

where ω_{TO} is the resonance frequency, also known as the transverse optical phonon frequency ($\omega_{TO} = 268.7\,cm^{-1}$), $\gamma = 2.4\,cm^{-1}$ is the phonon damping constant, and $\epsilon_{static} - \epsilon_\infty = 12.8 - 10.8 = 2.0$ is the difference between the static and high frequency dielectric constant [23, 57] in GaAs.

A.3 Publications not explicitly discussed in this thesis

Refereed conference proceedings

- S. Winnerl, B. Zimmermann, F. Peter, H. Schneider, M. Helm, “Terahertz emitters and detectors for radially and azimuthally polarized beams”, Proceedings of SPIE 7366 (2009).
- S. Winnerl, B. Zimmermann, R. Hubrich, F. Peter, H. Schneider, M. Helm, ”Free-space propagation of radially and azimuthally polarized terahertz Bessel-Gauss beams”, Proceeding to CLEO-Europe (2009).
- S. Winnerl, B. Zimmermann, F. Peter, H. Schneider, M. Helm, “Terahertz vector beams”; Conference Digest of the 33rd International Conference on Infrared, Millimeter, and Terahertz Waves (2008).
- S. Winnerl, S. Nitsche, F. Peter, O. Drachenko, H. Schneider, M. Helm, K. Köhler, “Easy-to-use scalable antennas for coherent detection of THz radiation”, Springer Proceedings in Physics 119, pp. 167-169 (2007).
- S. Winnerl, F. Peter, S. Nitsche, A. Dreyhaupt, O. Drachenko, H. Schneider, M. Helm, K. Köhler, “Coherent detection of terahertz radiation with scalable antennas”, Conference Digest of the Joint 32nd International Conference on Infrared and Millimeter Waves and the 15th International Conference on Terahertz Electronics 1-4244-1439-3, pp. 740-741 (2007).
- S. Winnerl, A. Dreyhaupt, F. Peter, D. Stehr, M. Helm, T. Dekorsy, “High-intensity THz radiation from a large-aperture photoconductive emitter”, Springer Proceedings in Physics 110 , pp. 73-76 (2006).

Contributions at conferences

- F. Peter, S. Winnerl, H. Schneider, M. Helm, K. Köhler, “Terahertz wave emission from InGaAsN large area emitter”, International Workshop on Optical Terahertz Science and Technology, 07.-11.03.2009, Santa Barbara, USA.

- F. Peter, S. Winnerl, H. Schneider, M. Helm, K. Köhler, “Large-area terahertz emitters based on GaInAsN” SPIE Europe Microtechnologies for the New Millenium, 04.-06.05.2009, Dresden, Deutschland.

- S. Winnerl, B. Zimmermann, F. Peter, H. Schneider, M. Helm, “Terahertz emitters and detectors for radially and azimuthally polarized beams”, SPIE Europe Microtechnologies for the New Millenium, 04.-06.05.2009, Dresden, Deutschland.

- F. Peter, S. Winnerl, H. Schneider, M. Helm, K. Köhler, “Terahertz wave emission from InGaAsN large area emitter”, Frühjahrstagung Deutsche Physikalische Gesellschaft, 22.-27.03.2009, Dresden, Deutschland.

- S. Winnerl, B. Zimmermann, R. Hubrich, F. Peter, H. Schneider, M. Helm, ”Free-space propagation of radially and azimuthally polarized terahertz Bessel-Gauss beams”, CLEO-Europe, 14-19.06.2009, München, Deutschland.

- S. Winnerl, B. Zimmermann, R. Hubrich, F. Peter, H. Schneider, M. Helm, ”Photoconductive emitters and detectors for radially and azimuthally polarized terahertz beams”, GDR-E-2009 THz Workshop, 16.-17.11.2009, Montpellier, France.

- F. Peter, S. Winnerl, H. Schneider, M. Helm, K. Köhler, “Terahertz wave emission from an InGaAsN large area emitter”, GDR-E-2008 THz Workshop, 25.-26.09.2008, Paris, France.

- S. Winnerl, B. Zimmermann, F. Peter, H. Schneider, M. Helm, “Terahertz vector beams”, 33rd International Conference on Infrared, Millimeter, and Terahertz Waves, 14.- 19.09.2008, Pasadena, USA.

- F. Peter, S. Winnerl, S. Nitsche, A. Dreyhaupt, H. Schneider, M. Helm, K. Köhler, “THz detection with scalable photoconductive antennas”, Frühjahrstagung Deutsche und Europäische Physikalische Gesellschaft, 24.-29.02.2008, Berlin, Deutschland.

- S. Winnerl, F. Peter, S. Nitsche, A. Dreyhaupt, O. Drachenko, H. Schneider, M. Helm, K. Köhler, “Coherent detection of terahertz radiation with scalable antennas", The Joint 32nd International Conference on Infrared and Millimeter Waves and the 15th International Conference on Terahertz Electronics, 02.-09.09.2007, Cardiff, UK.

- S. Winnerl, S. Nitsche, F. Peter, O. Drachenko, H. Schneider, M. Helm, K. Köhler, "Easy-to-use scalable antennas for coherent detection of THz radiation", The Thirteenth International Conference on Narrow Gap Semiconductors, University of Surrey, 08.-12.07.2007, Guildford, UK.
- S. Winnerl, F. Peter, S. Nitsche, A. Dreyhaupt, O. Drachenko, H. Schneider, M. Helm, "Coherent detection of terahertz radiation with non-resonant antennas", French- Russian THz Seminar, Russian Foundation for Basic Research and Centre National de la Recherche Scientifique, 05.-06.06.2007, Toulouse, France.
- F. Peter, S. Nitsche, S. Winnerl, A. Dreyhaupt, H. Schneider, M. Helm, "Terahertz radiation from a large-area photoconductive device", Frühjahrstagung Deutsche Physikalische Gesellschaft, 26.-30.03.2007, Regensburg, Deutschland.
- F. Peter, S. Winnerl, A. Dreyhaupt, H. Schneider, M. Helm, "Profile of a photoconductive THz Emitter excited by an amplified laser system", Frühjahrstagung Deutsche und Europäische Physikalische Gesellschaft, 27.-31.03.2006, Dresden, Deutschland.
- S. Winnerl, A. Dreyhaupt, F. Peter, D. Stehr, M. Helm, T. Dekorsy, "High-intensity THz radiation from a large-aperture photoconductive emitter", 14th International Conference on Nonequilibrium Carrier Dynamics in Semiconductors (HCIS-14), 24.-29.07.2005, Chicago, USA.

Bibliography

[1] D.H. Auston, “Picosecond optoelectronic switching and gating in silicon”, Appl. Phys. Lett. 26, pp. 101–103 (1975).

[2] D.H. Auston, K.P. Cheung, and P.R. Smith, “Picosecond photoconducting Hertzian dipoles”, Appl. Phys. Lett. 45, pp. 284–286 (1984).

[3] M. van Exter, C. Fattinger, and D. Grischkowsky, “Terahertz time-domain spectrocopy of water vapor”, Opt. Lett. 14, pp. 1128–1130 (1989).

[4] D. Grischkowsky, S. Keiding, M. van Exter, and Ch. Fattinger, “Far-infrared time-domain spectroscopy with terahertz beams of dielectrics and semiconductors”, J. Opt. Soc. Am. B 7, pp. 2006–2015 (1990).

[5] D. E. Spence, P.N. Kean, and W. Sibbet, “60-fsec pulse generation from a self-mode-locked Ti:sapphire laser”, Opt. Lett. 16, pp. 42–44 (1991).

[6] S. Gupta, M.Y. Frankel, J.A. Valdmanis, J.F. Whitaker, G.A. Mourou, F.W. Smith, and A.R. Calawa, “Subpicosecond carrier lifetime in GaAs grown by molecular beam epitaxy at low temperatures”, Appl. Phys. Lett. 59, pp. 3276–3278 (1991).

[7] D.H. Auston, “Subpicosecond electro-optic shock waves”, Appl. Phys. Lett. 43, pp. 713–715 (1983).

[8] D.H. Auston, K.P. Cheung, J.A. Valdmanis, and D.A. Kleinman, “Cherenkov radiation from femtosecond optical pulses in electro-optic media”, Phys. Rev. Lett. 53, pp. 1555-1558 (1984).

[9] Q. Wu, X.C. Zhang, “Free-space electro-optic sampling of terahertz beams”, Appl. Phys. Lett. 67, pp. 3523–3525 (1995).

[10] M. Tonouchi, “Cutting-edge terahertz technology”, Nat. Photonics 1, pp. 97-105 (2007).

[11] A. Leitenstorfer, S. Hunsche, J. Shah, M.C. Nuss, and W.H. Knox, “Femtosecond charge transport in polar semiconductors”, Phys. Rev. Lett. 82, pp. 5140-5143 (1999).

[12] A. Othonos,“Probing ultrafast carrier and phonon dynamics in semiconductors”, J. Appl. Phys. 83, pp. 1789-1830 (1998).

[13] L. Ho, M. Pepper, and P. Taday, “Terahertz spectroscopy signatures and fingerprints”, Nature Photonics 2, pp. 541-543 (2008).

[14] A.G. Stepanov, J. Hebling, and J. Kuhl, “Efficient generation of subpicosecond terahertz radiation by phase-matched optical rectification using ultrashort laser pulses with tilted pulse fronts”, Appl. Phys. Lett. 83, pp. 3000–3002 (2003).

[15] A. Sell, A. Leitenstorfer, and R. Huber, “Phase-locked generation and field-resolved detection of widely tunable terahertz pulses with amplitudes exceeding 100 MV/cm”, Opt. Lett. 33, pp. 2767-2769 (2008).

[16] K. Wille, “Physik der Teilchenbeschleuniger und Synchrotronstrahlungsquellen”, B.G. Teubner, Stuttgart (1992).

[17] E.A. Zibik, T. Grange, B.A. Carpenter, N.E. Porter, R. Ferreira, G. Bastard, D. Stehr, S. Winnerl, M. Helm, H.Y. Liu, M.S. Skolnick, and L.R. Wilson,”Long lifetimes of quantum-dot intersublevel transitions in the terahertz range”, Nature Materials 8, pp. 803-807 (2009).

[18] M. Wagner, H. Schneider, S. Winnerl, M. Helm, T. Roch, A.M. Andrews, S. Schartner, and G. Strasser, “Resonant enhancement of second order sideband generation for intra-excitonic transitions in GaAs/AlGaAs multiple quantum wells”, Appl. Phys. Lett. 94, 241105 (2009).

[19] C. Walther, M. Fischer, G. Scalari, R. Terazzi, N. Hoyler, and J. Faist, “Quantum cascade lasers operating from 1.2 to 1.6 THz”, Appl. Phys. Lett. 91, 131122 (2007).

[20] B.S. Williams, S. Kumar, Q. Hu, and J.L. Reno, “High-power terahertz quantum-cascade lasers”, Electron. Lett. 42, pp. 89-91 (2006).

[21] A.W.M. Lee, Q. Qin, S. Kumar, B.S. Williams, Q. Hu, and J.L. Reno, ”Real-time terahertz imaging over a standoff distance (>25 meters)”, Appl. Phys. Lett. 89, 141125 (2006).

[22] V.A. Gorobets, B.F. Kuntsevich, V.O. Petukhov, “Terahertz gas laser”, IEEE IRMMW THz 2006 Plenary Paper, TueC4-8 (2007).

[23] M. Nagai, K. Tanaka, H. Ohtake, T. Bessho, T. Sugiura, T. Hirosumi, and M. Yoshida, “Generation and detection of terahertz radiation by electro-optical process in GaAs using 1.56 μm fiber laser pulses”, Appl. Phys. Lett. 85, pp. 3974-3976 (2004).

[24] Y. Ko, S. Sengupta, S. Tomasulo, P. Dutta, and I. Wilke, "Emission of terahertz-frequency electromagnetic radiation from bulk $Ga_xIn_{1-x}As$ crystals", Phys. Rev. B 78, 035201 (2008).

[25] A. Nahata, A.S. Weling, and T.F. Heinz, "A wideband coherent terahertz spectroscopy system using optical rectification and electro-optic sampling", Appl. Phys. Lett. 69, pp. 2321–2323 (1996).

[26] Q. Wu, X.C. Zhang, "Design and characterization of traveling-wave electrooptic terahertz sensors", IEEE Journal of Quantum Electronics 2, pp. 693-700 (1996).

[27] A. Bonvalet, M. Joffre, J.L. Martin, and A. Migus, "Generation of ultrabroadband femtosecond pulses in the mid-infrared by optical rectification of 15 fs light pulses at 100 MHz repetition rate", Appl. Phys. Lett. 67, pp. 2907–2909 (1995).

[28] T.J. Carrig, G. Rodriguez, T.C. Clement, A.J. Taylor, and K.R. Stewart, "Scaling of terahertz radiation via optical rectification in electro-optic crystals", Appl. Phys. Lett. 66, pp. 121–123 (1995).

[29] K.H. Yang, P.L. Richards, and Y.R. Shen, "Generation of far-infrared radiation by picosecond light pulses in $LiNbO_3$", Appl. Phys. Lett. 19, pp. 320–323 (1971).

[30] Y.-S. Lee, T. Meade, V. Perlin, H. Winful, T.B. Norris, and A. Galvanauskas, "Generation of narrow-band terahertz radiation via optical rectification of femtosecond pulses in periodically poled lithium niobat", Appl. Phys. Lett. 76, pp. 2505-2507 (2000).

[31] T. Löffler, T. Hahn, M. Thomson, F. Jacob, and H.G. Roskos, "Large-area electro-optic ZnTe terahertz emitters", Opt. Express 13, pp. 5353-5362 (2005).

[32] R. Huber, A. Brodschelm, F. Tauser, and A. Leitenstorfer, "Generation and field-resolved detection of femtosecond electromagnetic pulses tunable up to 41 THz", Appl. Phys. Lett. 76, pp. 3191–3193 (2000).

[33] K. Reimann, "Table-top sources of ultrashort THz pulses", Rep. Prog. Phys. 70, pp. 1597–1632 (2007).

[34] K.L. Yeh, M.C. Hoffmann, J. Hebling, and K.A. Nelson, "Generation of 10 μJ ultrashort terahertz pulses by optical rectification", Appl. Phys. Lett. 90, 171121 (2007).

[35] N. Karpowicz, J. Dai, X. Lu, Y. Chen, M. Yamaguchi, H. Zhao, X.C. Zhang, M. Price-Gallagher, C. Fletcher, O. Mamer, A. Lesimple, and K. Johnson,

"Coherent heterodyne time-domain spectrometry covering the entire terahertz gap", Appl. Phys. Lett. 92, 011131 (2008).

[36] M.B. Ketchen, D. Grischkowsky, T.C. Chen, C.C. Chi, I.N. Duling III, N.J. Halas, J.M. Halbout, J.A. Kash, and G.P. Li, "Generation of subpicosecond electrical pulses on coplanar transmission lines", Appl. Phys. Lett. 48, pp. 751–753 (1986).

[37] C. Weiss, R. Wallenstein, and R. Beigang, "Magnetic-field-enhanced generation of terahertz radiation in semiconductor surfaces", Appl. Phys. Lett. 77, pp. 4160–4162 (2000).

[38] M.B. Johnston, D.M. Whittaker, A. Corchia, A.G. Davies, and E.H. Linfield, "Theory of magnetic-field enhancement of surface-field terahertz emission", J. Appl. Phys. 91, pp. 2104–2106 (2002).

[39] D. Grischkowsky, "Nonlinear generation of subpsec pulses of THz electromagnetic radiation by optoelectronics - applications to time-domain spectroscopy," invited paper in "Frontiers in Nonlinear Optics", Edited by H. Walther, N. Koroteev and M.O. Scully, Inst. of Phys. Pub. Bristol and Philadelphia, pp. 196-227 (1993).

[40] L. Duvillaret, F. Garet, J.-F. Roux, and J.-L. Coutaz, "Analytical modeling and optimization of terahertz time-domain spectrocopy experiments using photoswitches as antennas", IEEE Journal on Selected Topics in Quantum Electronics 7, pp. 615 (2001).

[41] G.C. Loata, M.D. Thomson, T. Löffler, and H.G. Roskos, "Radiation field screening in photoconductive antennae studied via pulsed terahertz emission spectroscopy", Appl. Phys. Lett. 91, 232506 (2007).

[42] G. Segschneider, F. Jacob, T. Löffler, H.G. Roskos, S. Tautz, P.Kiesel, and G. Döhler, "Free-carrier dynamics in low-temperature-grown GaAs at high excitation densities investigated by time-domain terahertz spectroscopy", Phys. Rev. B 65, 125205 (2002).

[43] H. Harde, D. Grischkowsky, "Coherent transients excited by subpicosecond pulses of terahertz radiation", J. Opt. Soc. Am. B 8, pp. 1642-1651 (1991).

[44] M. Tani, S. Matsuura, K. Sakai, and S.-I. Nakashima, "Emission characteristics of photoconductive antennas based on low-temperature-grown GaAs and semi-insulating GaAs", Appl. Opt. 36, pp. 7853–7859 (1997).

[45] T.-A. Liu, G.-R. Lin, Y.-C. Lee, S.-C. Wang, M. Tani, H.-H. Wu, and C.-L. Pan, "Dark current and trailing-edge suppression in ultrafast photoconductive

switches and terahertz spiral antennas fabricated on multienergy arsenic-ion-implanted GaAs", J. Appl. Phys. 98, 013711 (2005).

[46] J.E. Pedersen, V.G. Lyssenko, J.M. Hvam, P. Uhd Jepsen, S.R. Keiding, C.B. Soerensen, and P.E. Lindelof, "Ultrafast local field dynamics in photoconductive THz antennas", Appl. Phys. Lett. 62, pp. 1265-1267 (1993).

[47] D.R. Dykaar, B.I. Greene, J.F. Federici, A.F.J. Levi, L.N. Pfeiffer, and R.F. Kopf, "Log-periodic antennas for pulsed terahertz radiation", Appl. Phys. Lett. 59, pp. 262–264 (1991).

[48] K.A. McIntosh, E.R. Brown, K.B. Nichols, O.B. McMahon, W.F. DiNatale, and T.M. Lyszczarz "Terahertz measurements of resonant planar antennas coupled to low-temperature-grown GaAs photomixers", Appl. Phys. Lett. 69, pp. 3632–3634 (1996).

[49] G.C. Loata, T. Löffler, and H.G. Roskos, "Evidence for long-living charge carriers in electrically biased low-temperature-grown GaAs photoconductive switches", Appl. Phys. Lett. 90, 052101 (2007).

[50] Y.R. Shen, "The Principles of Nonlinear Optics", Wiley, New Jersey (2003).

[51] R.W. Boyd, "Nonlinear optics", Academic Press (1992).

[52] R. A. Kaindl, D.C. Smith, M. Joschko, M.P. Hasselbeck, M. Woerner, and T. Elsaesser, "Femtosecond infrared pulses tunable from 9 to 18 μm at an 88-MHz repetition rate", Opt. Lett. 23, pp. 861-863 (1998).

[53] K.L. Vodopyanov, M.M. Fejer, X. Yu, J.S. Harris, Y.-S. Lee, W.C. Hurlbut, V.G. Kozlov, D. Bliss, and C. Lynch, "Terahertz-wave generation in quasi-phase-matched GaAs", Appl. Phys. Lett. 89, 141119 (2006).

[54] K.L. Vodopyanov, "Optical THz-wave generation with periodically-inverted GaAs", Laser and Photonics Review 2, pp. 11-25 (2008).

[55] S.S. Dhillon, C. Sirtori, J. Alton, S. Barbieri, A. De Rossi, H.E. Beere, and D.A. Ritchie "Terahertz transfer onto a telecom optical carrier", Nature Photonics 1, pp. 411-415 (2007).

[56] V. Berger, and C. Sirtori, "Nonlinear phase matching in THz semiconductor waveguides", Semiconductor Science and Technology 19, pp. 964-970 (2004).

[57] J.S. Blakemore, "Semiconducting and other major properties of gallium arsenide", J. Appl. Phys. 53, pp. 81-123 (1982).

[58] S. Hargreaves, K. Radhanpura, and R.A. Lewis, “Generation of terahertz radiation by bulk and surface optical rectification from crystal planes of arbitrary orientation”, Phys. Rev. B 80, pp. 195323 (2009).

[59] A. Dreyhaupt, S. Winnerl, T. Dekorsy, and M. Helm, “High-intensity terahertz radiation from a microstructured large-area photoconductor”, Appl. Phys. Lett. 86, 121114 (2005).

[60] A. Dreyhaupt, S. Winnerl, M. Helm, and T. Dekorsy, “Optimum excitation conditions for the generation of high-electric-field terahertz radiation from an oscillator-driven photoconductive device”, Opt. Lett. 31, pp. 1546–1548 (2006).

[61] S. Winnerl, F. Peter, A. Dreyhaupt, B. Zimmermann, M. Wagner, H. Schneider, M. Helm, and K. Köhler, “Generation and detection of THz radiation with scalable antennas based on GaAs substrates with different carrier lifetimes”, IEEE Journal of Selected Topics in Quantum Electronics 14, pp. 449-457 (2008).

[62] S. Gupta, J.F. Whitaker, and G.A. Mourou, “Ultrafast carrier dynamics in III-V semiconductors grown by molecular-beam epitaxy at very low substrate temperatures”, IEEE Journal of Quantum Electronics 28, pp. 2464-2472 (1992).

[63] H.-H. Wang, P. Grenier, J.F. Whitaker, H. Fujioka, J. Jasinski, and Z. Liliental-Weber, “Ultrafast response of As-implanted GaAs photoconductors”, IEEE Journal on Selected Topics in Quantum Electronics 2, pp. 630 -635 (1996).

[64] G. L. Witt, “LTMBE GaAs: present status and perspectives”, Materials Science and Engineering B 22, pp. 9 -15 (1993).

[65] C. Winnewisser, P. Uhd Jepsen, M. Schall, V. Schyja, and H. Helm, “Electro-optic detection of THz radiation in $LiTaO_3$, $LiNbO_3$ and ZnTe”, Appl. Phys. Lett. 70, pp. 3069–3071 (1997).

[66] A. Nahata, D.H. Auston, C. Wu, and T. F. Heinz, “Coherent detection of freely propagating terahertz radiation by electro-optic sampling”, Appl. Phys. Lett. 68, pp. 150–152 (1996).

[67] A. Leitenstorfer, S. Hunsche, J. Shah, M.C. Nuss, and W.H. Knox, “Detectors and sources for ultrabroadband electro-optic sampling: experiment and theory”, Appl. Phys. Lett. 74, pp. 1516-1518 (1999).

[68] T.D. Dorney, R.G. Baraniuk, and D.M. Mittleman, “Material parameter estimation with terahertz time-domain spectroscopy”, J. Opt. Soc. Am. A 18, pp. 1562-1571 (2001).

[69] D. Mittleman (ed.),"Sensing with terahertz radiation", Springer, Berlin (2003).

[70] Yun-Shik Lee,"Principles of Terahertz Science and Technology", Springer, Berlin (2009).

[71] P.F. Goldsmith, "Quasioptical Systems", IEEE Press, Chapman and Hall (1998).

[72] F. Peter, "Untersuchung der räumlichen Strahlcharakteristik von fotoleitenden Terahertz-Strahlungsquellen", Diplomarbeit FZD und TU Dresden (2006).

[73] H.A. Bethe, "Theory of diffraction by small holes", Phys. Rev. 66, pp. 163–182 (1944).

[74] J. Faure, J. van Tilborg, R.A. Kaindl, and W.P. Leemans, "Modelling laser-based table-top THz sources: Optical rectification, propagation and electro-optic sampling", Review Optical and Quantum Electronics 36, pp. 681–697 (2004).

[75] G. Gallot, S. P. Jamison, R. W. McGowan, and D. Grischkowsky, "Terahertz waveguides", J. Opt. Soc. Am. B 17, pp. 851–863 (2000).

[76] S. P. Jamison, R. W. McGowan, and D. Grischkowsky, "Single-mode waveguide propagation and reshaping of sub-ps terahertz pulses in sapphire fibers", Appl. Phys. Lett.76, pp. 1987–1989 (2000).

[77] R. Mendis and D. Grischkowsky, "Plastic ribbon THz waveguide", J. Appl. Phys. 88, pp. 4449–4451 (2001).

[78] R. Mendis and D. Grischkowsky, "Undistorted guided-wave propagation of sub-picosecond terahertz pulses", Opt. Lett. 26, pp. 846–848 (2001).

[79] R. Mendis and D.M. Mittleman, "An investigation of the lowest-order transverse-electric (TE_1) mode of the parallel-plate waveguide for THz pulse propagation", J. Opt. Soc. Am. B 26, pp. A6-A13 (2009).

[80] H. Han, H. Park, M. Cho, and J. Kim, "Terahertz pulse propagation in a plastic photonic crystal fiber", Appl. Phys. Lett. 80, pp. 2634–2636 (2002).

[81] T.I. Jeon and D. Grischkowsky, "Direct optoelectronic generation and detection of sub-ps electrical pulses on sub-mm coaxial transmission lines", Appl. Phys. Lett. 85, pp. 6092–6094 (2004).

[82] K. Wang and D.M. Mittleman, "Metal wires for terahertz wave guiding", Nature 432, pp. 376-379 (2004).

[83] T.I. Jeon, J. Zhang, D. Grischkowsky, "THz Sommerfeld wave propagation on a single metal wire", Appl. Phys. Lett. 86, 161904 (2005).

[84] K. Wang and D. M. Mittleman, "Guided propagation of terahertz pulses on metal wires", J. Opt. Soc. Am. B 22, pp. 2001–2008 (2005).

[85] M. Wachter, M. Nagel, and H. Kurz, "Metallic slit waveguide for dispersion-free low-loss terahertz signal transmission", Appl. Phys. Lett. 90, 061111 (2007).

[86] Comsol based on a Finite-Elemente-Methode (FEM) for solving various kinds of differential equations, see http://www.comsol.com (2009).

[87] J.T. Darrow, Xi-Cheng Zhang, D.H. Auston, J.D. Morse, "Saturation properties of large-aperture photoconductive antennas", IEEE Journal of Quantum Electronics 28, pp. 1607-1616 (1992).

[88] G. Zhao, R.N. Schouten, N. van der Valk, W.T. Wenckebach, and P.C.M. Planken, "Design and performance of a THz emission and detection setup based on a semi-insulating GaAs emitter", Rev. Sci. Instrum. 73, pp. 1715-1719 (2002).

[89] W. Shi, J. Xu, and X.-C. Zhang, "Terahertz generation from Si_3N_4 covered photoconductive dipole antenna", Chinese Opt. Lett. 1, pp. 308-310 (2003).

[90] S. Winnerl, B. Zimmermann, F. Peter, H. Schneider, and M. Helm, "Terahertz Bessel-Gauss beams of radial and azimuthal polarization from microstructured photoconductive antennas", Opt. Express 17, pp. 1571-1576 (2009).

[91] H. Son, T. B. Norris, and J. F. Whitaker, "Terahertz electromagnetic pulses as probes for transient velocity overshoot in GaAs and Si", J. Opt. Soc. Am. B 11, pp. 2519–2527 (1994).

[92] A. Schwanhäusser, M. Betz, M. Eckardt, S. Trumm, L. Robledo, S. Malzer, A. Leitenstorfer, and G. H. Döhler, "Ultrafast transport of electrons in GaAs: Direct observation of quasiballistic motion and side valley transfer", Phys. Rev. B 70, 085211 (2004).

[93] A. Leitenstorfer, S. Hunsche, J. Shah, M. C. Nuss, and W. H. Knox, "Femtosecond high-field transport in compound semiconductors", Phys. Rev. B 61, pp. 16642–16652 (2000).

[94] C. Ludwig, and J. Kuhl, "Studies of the temporal and spectral shape of terahertz pulses generated from photoconducting switches", Appl. Phys. Lett. 69, pp. 1194–1196 (1996).

[95] A. Dreyhaupt, "Terahertz-Strahlung auf der Basis beschleunigter Ladungsträger in GaAs", Dissertation FZD und TU Dresden (2007).

[96] D. You, R.R. Jones, P.H. Bucksbaum, and D.R. Dykaar, "Generation of high-power sub-single-cycle 500-fs electromagnetic pulses", Opt. Lett. 18, pp. 290–292 (1993).

[97] G. Rodriguez, and A.J. Taylor, "Screening of the bias field in terahertz generation from photoconductors", Opt. Lett. 21, pp. 1046–1048 (1996).

[98] P. K. Benicewicz, J.P. Roberts, and A.J. Taylor, "Scaling of terahertz radiation from large-aperture biased photoconductors", J. Opt. Soc. Am. B 11, pp. 2533–2546 (1994).

[99] H. Künzel, J. Böttcher, R. Gibis, and G. Urmann, "Material properties of $Ga_{0.47}In_{0.53}As$ grown on InP by low-temperature molecular beam epitaxy", Appl. Phys. Lett. 61, pp. 1347-1349 (1992).

[100] M. Suzuki, and M. Tonouchi, "Fe-implanted InGaAs photoconductive terahertz detectors triggered by 1.56 μm femtosecond optical pulses", Appl. Phys. Lett. 86, 163504 (2005).

[101] A. Takazato, M. Kamakura, T. Matsui, J. Kitagawa, and Y. Kadoya, "Detection of terahertz waves using low-temperature-grown InGaAs with 1.56 μm pulse excitation", Appl. Phys. Lett. 90, 101119 (2007).

[102] A. Takazato, M. Kamakura, T. Matsui, J. Kitagawa, and Y. Kadoya, "Terahertz wave emission and detection using photoconductive antennas made on low-temperature-grown InGaAs with 1.56 μm pulse excitation", Appl. Phys. Lett. 91, 011102 (2007).

[103] K. Köhler, J.Wagner, P. Ganser, D. Serries, T. Geppert, M. Maier, L. Kirste, "The realization of long-wavelength ($\lambda \leq 2.3\,\mu m$) $Ga_{1-x}In_xAs_{1-y}N_y$ quantum wells on InP by molecular-beam epitaxy", J. Phys. Condens. Matter 16, pp. 2995-3008 (2004).

[104] I. Vurgaftman, J.R. Meyer, and L.R. Ram-Mohan "Band parameters for III-V compound semiconductors and their alloys", J. Appl. Phys. 89, pp. 5815-5875 (2001).

[105] Y.X. Wang, Z. Chen, Z. Zhao, L. Zhang, K. Kang, and Y. Zhang, "Restoration of terahertz signals distorted by atmospheric water vapor absorption", J. Appl. Phys. 105, pp. 103105(1-7) (2009).

[106] B.K. Ridley, "Quantum Processes in Semiconductors", Oxford University Press, Oxford, pp. 218-231 (1999).

[107] T.S. Moss, "Optical absorption edge in GaAs and its dependence on electric field", J. Appl. Phys. 32, pp. 2136-2139 (1961).

[108] A. Takazato, M. Kamakura, T. Matsui, J. Kitagawa, and Y. Kadoya, "Detection of terahertz waves using low-temperature-grown InGaAs with 1.56 μm pulse excitation", Appl. Phys. Lett. 90, 101119 (2007).

[109] W. Shan, W. Walukiewicz, J. W. Ager III, E. E. Haller, J. F. Geisz, D. J. Friedman, J. M. Olson, and S. R. Kurtz, "Effect of nitrogen on the band structure of GaInNAs alloys", J. Appl. Phys. 86, pp. 2349-2351 (1999).

[110] W. Shan, W. Walukiewicz, J.W. Ager, E.E. Haller, J.F. Geisz, D.J. Friedman, J.M. Olson, S.R. Kurtz, "Band anticrossing in GaInNAs alloys", Phys. Rev. Lett. 82, pp. 1221-1224 (1999).

[111] S. Fahy and E. P. O'Reilly, "Intrinsic limits on electron mobility in dilute nitride semiconductors", Appl. Phys. Lett. 83, pp. 3731-3733 (2003).

[112] J. F. Ziegler, J. P. Biersack, and U. Littmark, "The stopping range of ions in solids", New York: Pergamon, 1, (1985) Online Available: http://www.srim.org.

[113] P.S. Peercy,"Raman scattering of ion-implanted GaAs", Appl. Phys. Lett. 18, pp. 574–576 (1971).

[114] P.S. Pizani, A. Mlayah, J. Groenen, R.Carles, and A. Claverie, "High strain effects evidenced by Raman scattering in arsenic clusters in As-implanted GaAs", Appl. Phys. Lett. 66, pp. 1927–1929 (1995).

[115] A. Krotkus, S. Marcinkevicius, J. Jasinski, M. Kaminska, H.H. Tan, and C. Jagadish, "Picosecond carrier lifetime in GaAs implanted with high doses of As ions: An alternative material to low-temperature GaAs for optoelectronic applications", Appl. Phys. Lett. 66, pp. 3304–3306 (1995).

[116] T.-A. Liu, M. Tani, and C.-L. Pan, "THz radiation emission properties of multienergy arsenic-ion-implanted GaAs and semi-insulating GaAs based photoconductive antennas," J. Appl. Phys. 93, pp. 2996–3001 (2003).

[117] M. Mikulics, M. Marso, I. Camara Mayorga, R. Guesten, S. Stancek, P. Kovac, S. Wu, X. Li, M. Khafizov, R. Sobolewski, R. E. A. Michael, R. Schieder, M. Wolter, D. Buca, A. Foerster, P. Kordos, and H. Lueth, "Photomixers fabricated on nitrogen-ion-implanted GaAs," Appl. Phys. Lett. 87, 041106 (2005).

[118] Y. Kato, T. Shimada, Y. Shiraki, and K. F. Komatsubara, "Electrical conductivity of disordered layers in GaAs crystal produced by ion implantation", J. Appl. Phys. 45, pp. 1044–1049 (1974).

[119] M. Lambsdorff, J. Kuhl, J. Rosenzweig, A. Axmann, and J. Schneider, “Subpicosecond carrier lifetimes in radiation-damaged GaAs”, Appl. Phys. Lett. 58, pp. 1881–1883 (1991).

[120] J. S. Weiner, and P. Y. Yu, “Free carrier lifetime in semi-insulating GaAs from time-resolved band-to-band photoluminescence,” J. Appl. Phys. 55, pp. 3889–3891 (1984).

[121] A. Krotkus, and J.-L. Coutaz, “Non-stoichiometric semiconductor materials for terahertz optoelectronics applications” Semicond. Sci. Technol. 20, pp. 142–150 (2005).

[122] J. Lloyd-Hughes, E. Castro-Camus, M. D. Fraser, C. Jagadish, and M.B. Johnston, “Carrier dynamics in ion-implanted GaAs studied by simulation and observation of terahertz emission”, Phys. Rev. B 70, 235330 (2004).

[123] S. Quabis, R.Dorn, m. Eberler, O. Glöckl, G.Leuchs, “Focusing light to a tighter spot”, Opt. Comm. 179, pp. 1-7 (2000).

[124] H.P. Urbach, and S.F. Pereira, “Field in focus with a maximum longitudinal electric component”, Phys. Rev. Lett. 100, 123904 (2008).

[125] J.A. Deibel, K. Wang, M.D. Escarra, D.M. Mittleman, “Enhanced coupling of terahertz radiation to cylindrical wire waveguides”, Opt. Express 14, pp. 279-290 (2006).

[126] G. Chang, C.J. Divin, C.H. Liu, S.L. Williamson, A. Galvanauskas, T.B. Norris, “Generation of radially polarized terahertz pulses via velocity-mismatched optical rectification”, Opt. Lett. 32, pp. 433-435 (2007).

[127] D.G. Hall, “Vector-beam solutions of Maxwell’s wave equation”, Opt. Lett. 21, pp. 9-11 (1996).

[128] E. Castro-Camus, J. Lloyd-Hyghes, M. B. Johnston, M. D. Fraser, H. H. Tan, C. Jagdish, “Polarization-sensitive terahertz detection by multicontact photoconductive receivers”, Appl. Phys. Lett. 86, 254102 (2005).

[129] G. Matthäus, T. Schreiber, J. Limpert, S. Nolte, G. Torosyan, R. Beigang, S. Riehemann, G. Notni and A. Tünnermann, “Surface-emitted THz generation using a compact ultrashort pulse fiber amplifier at 1060 nm”, Opt. Comm. 261, pp. 114-117 (2006).

[130] S. Wang, X.C. Zhang, “Pulsed terahertz tomography”, J. Phys. D: Appl. Phys. 37, pp. R1-R36 (2004).

[131] S. Wietzke, C. Jansen, F. Rutz, D.M. Mittleman, and M. Koch, “Determination of additive content in polymeric compounds with terahertz time-domain spectroscopy”, Polymer Testing 26, pp. 614-618 (2007).

[132] T. Yasuda, Y. Kawada, H. Toyoda, and H. Takahashi, “Terahertz movies of internal transmission images”, Opt. Express 15, pp. 15583-15588 (2007).

[133] H. Nyquist, “Certain topics in telegraph transmission theory”, Trans. Amer. Inst. Elect. Eng. 47, pp. 617-644 (1928), reprint: Proc. IEEE 90, pp. 280-305 (2002).

[134] J. Xu, Z. Lu, and X.C. Zhang, ”Compact involute optical delay line”, Electronics Lett. 40, pp. 1218-1219 (2004).

[135] J. Xu, and X.C. Zhang, “Circular involute stage”, Opt. Lett. 29, pp. 2082-2084 (2004).

[136] H. Kitahara, M. Tani, and M. Hangyo, “High-repetition-rate optical delay line using a micromirror array and galvanometer mirror for a terahertz system”, Rev. Sci. Instrum. 80, 076104 (2009).

[137] H. Kitahara, M. Tani, and M. Hangyo, Erratum: “High-repetition-rate optical delay line using a micromirror array and galvanometer mirror for a terahertz system”, Rev. Sci. Instrum. 80, 119901 (2009).

[138] Z. Jiang, and X.C. Zhang, “Electro-optic measurement of THz field pulses with a chirped optical beam”, Appl. Phys. Lett. 72, pp. 1945-1947 (1998).

[139] J. Shan, A.S. Weling, E. Knoesel, L. Bartels, M. Bonn, G.A. Reider, and T.F. Heinz, “Single-shot measurement of terahertz electromagnetic pulses by use of electro-optic sampling”, Opt. Lett. 25, pp. 426-428 (2000).

[140] A. Bartels, A. Thoma, C. Janke, T. Dekorsy, A. Dreyhaupt, S. Winnerl, and M. Helm, “High resolution THz spectrometer with kHz scan rates”, Opt. Express 14, pp. 430-437 (2006).

[141] A. Bartels, R. Cerna, C. Kistner, A. Thoma, F. Hudert, C. Janke, and T. Dekorsy, “Ultrafast time-domain spectroscopy based on high-speed asynchronous optical sampling”, Rev. Sci. Instrum. 78, pp. 035107 (2007).

[142] G. Klatt, R. Gebs, C. Janke, T. Dekorsy, and A. Bartels, ”Rapid-scanning terahertz precision spectrometer with more than $6 THz$ spectral coverage”, Opt. Express 17, pp. 22847-22854 (2009).

[143] X.-C. Zhang, X.F. Ma, Y. Jin, T.-M. Lu, E.P. Boden, P.D. Phelps, K.R. Stewart, and C.P. Yakymyshyn, "Terahertz optical rectification from a nonlinear organic crystal", Appl. Phys. Lett. 61, pp. 3080-3082 (1992).

[144] V.G. Dmitriev, G. G. Gurzadyan, D.N. Nikogosyan, "Handbook of nonlinear optical crystals", Springer, 3 (1999)

[145] A. Schneider, M. Neis, M. Stillhart, B. Ruiz, R.U.A. Khan, and P. Günter, "Generation of terahertz pulses through optical rectification in organic DAST crystals: theory and experiment", J. Opt. Soc. Am. B 23, pp. 1822-1835 (2006).

[146] A. Schneider, M. Stillhart, and P. Günter, "High efficiency generation and detection of terahertz pulses using laser pulses at telecommunication wavelengths", Opt. Express 14, pp. 5376-5384 (2006).

[147] T. Taniuchi, S. Okada, and H. Nakanishi, "Widely tunable terahertz-wave generation in an organic crystal and its spectroscopic application", J. Appl. Phys. 95, pp. 5984-5988 (2004).

[148] A. Rice, Y. Jin, X.F. Ma, X.C. Zhang, D.Bliss, J.Larkin, and M. Alexander, "Terahertz optical rectification from <110> zinc-blende crystals", Appl. Phys. Lett. 64, pp. 1324-1326 (1994).

[149] P.C.M. Planken, H.K. Nienhuys, H.J. Bakker, T. Wenckebach, "Measurement and calculation of the orientation dependence of terahertz pulse detection in ZnTe", J. Opt. Soc. Am. B 18, pp. 313-317 (2001).

[150] A. Penzkofer, A. Bugayev, "Two-photon absorption and emission dynamics of bulk GaAs", Optical and Quantum Electronics 21, pp. 283-306 (1989).

[151] M.D. Dvorak, W.A. Schroeder, D.R. Andersen, A.L. Smirl, and B.S. Wherrett, "Measurement of the anisotropy of two-photon absorption coefficients in zincblende semiconductors", IEEE J. Quantum Electron. 30, pp. 256-268 (1994).

[152] J.H. Bechtel, and W.L. Smith, "Two-photon absorption in semiconductors with picosecond laser pulses", Phys. Rev. B 13, pp. 3515-3522 (1976).

[153] G.C. Valley, T.F. Boggess, J. Dubard, and A.L. Smirl, "Picosecond pump-probe technique to measure deep-level, free-carrier, and two photon cross sections in GaAs", J. Appl. Phys. 66, pp. 2407-2413 (1989).

[154] J.T. Boyd, "Theory of parametric oscillation phase matched in GaAs thin-film waveguides", IEEE J. Quantum Electronics 8, pp. 788-796 (1972).

[155] M.I. Bakunov, S.B. Bodrov, A.V. Maslov, and M. Hangyo, "Theory of terahertz generation in a slab of electro-optic material using an ultrashort laser pulse focused to a line", Phys. Rev. B 76, pp. 085346(1-18) (2007).

[156] A. Marandi, T.E. Darcie, P.P.M. So, "Design of a continuous-wave tunable terahertz source using waveguide-phase-matched GaAs", Opt. Express 16, pp. 10427-10433 (2008).

[157] R.L. Aggarwal, A. Sanchez, M.M. Stuppi, R.E. Fahey, A.J. Strauss, W.R. Rapoport, and C.P. Khattak,"Residual infrared absorption in as-grown and annealed crystals of $Ti : Al_2O_3$",IEEE Journal of Quantum Electronics 24, pp. 1003-1008 (1988).

[158] Femtolasers, Floragasse 7, A-1070 Vienna, "Users manual for femtosecond multipass amplifier FEMTOPOWER COMPACT PRO"

[159] APE, Plauener Str. 163, 13053 Berlin, "Datasheet for pump tuned ultrafast optical parametric oscillator"

[160] P.W. Milonni, and J.H. Eberly "Lasers", Wiley, pp. 68 (1988).

[161] S. Adachi, "Physical Properties of III-V Semiconductor Compounds", Wiley, pp. 64 and pp. 137 (1992).

Danksagung

An dieser Stelle möchte ich mich bei allen bedanken, die zum Gelingen dieser Arbeit beigetragen haben. Mein besonderer Dank gilt Herrn Prof. Manfred Helm, der es ermöglicht hat, an diesem interessanten und spannenden Thema der Halbleiterphysik zu arbeiten. In gleicher Weise danke ich Dr. Harald Schneider für die Bereitstellung der dafür benötigten Mittel und die reichhaltigen Diskussionen und Anregungen. Dr. Stephan Winnerl danke ich für die umfassende Begleitung von der Ideenentwicklung bis zur praktischen Realisierung. Sein Optimismus und besonnene Art war eine große Hilfe für mich. Prof. Thomas Dekorsy danke ich dafür ein Gutachten über meine Dissertation zu erstellen. Meinem Bürokollegen "Dr." (in spe) Martin Wagner danke ich für zahlreiche fruchtvolle Diskussionen.

Allen Kollegen der Abteilung danke ich für das angenehme Arbeitsklima und die Art und Weise wie Probleme gemeinsam diskutiert wurden. Besonders zu nennen sind: Andre Dreyhaupt, Sven Nitsche, Oliver Kallauch, Ralf Hubrich, Burkhard Zimmermann, Uta Lucchesi, Oleksiy Drachenko, Dominik Stehr, Charlotte Pfau, Steffen Sinning, Christiana Villas-Boas Grimm, Sabine Zybell und Rainer Jacob.

Herrn Dr. Klaus Köhler vom Fraunhofer Institut für Angewandte Festkörperphysik Freiburg danke ich für das Wachstum ein paar exzellenter Proben. Dem gesamtem Team der Halbleiterprozessierung um Dr. Bernd Schmidt danke ich für die Unterstützung bei der Prozessierung im Reinraum.

Mein besonderer Dank gilt auch meiner Schwester und meinen Eltern für die stete Unterstützung. Zuletzt möchte ich auch meiner kleinen Tochter Valerie und meiner zukünftigen Frau Julia für Ihre Unterstützung und Motivation danken.

Versicherung

Hiermit versichere ich, dass ich die vorliegende Arbeit ohne unzulässige Hilfe Dritter und ohne Benutzung anderer als der angegebenen Hilfsmittel angefertigt habe; die aus fremden Quellen direkt oder indirekt übernommenen Gedanken sind als solche kenntlich gemacht. Die Arbeit wurde bisher weder im Inland noch im Ausland in gleicher oder ähnlicher Form einer anderen Prüfungsbehörde vorgelegt.
Die Arbeit entstand mit wissenschaftlicher Betreuung durch Prof. Dr. Manfred Helm am Institut für Ionenstrahlphysik und Materialforschung des Forschungszentrums Dresden Rossendorf. Manfred Helm ist Professor im Institut für Angewandte Physik der Fakultät Mathematik und Naturwissenschaften der TU Dresden.
Ich habe vorher kein anderes Promotionsverfahren eröffnet. Ich erkenne die Promotionsordnung der Fakultät Mathematik und Naturwissenschaften der Technischen Universität Dresden in der aktuell gültigen Fassung vom 27.05.2009 an.

Falk Peter Dresden, den 2010